Air Force Grant: AFOSR-85-0181
FINAL TECHNICAL REPORT
July 01, 1985 to February 28, 1989

AD-A222 245

APPENDICIES

INFRARED OBSERVATIONS OF THE SOLAR SYSTEM

INFRARED OBSERVATIONS OF THE SOLAR SYSTEM
IN SUPPORT OF LARGE APERTURE INFRARED
TELESCOPE [LARITS] : CALIBRATION

by

Department of Mechanical Engineering
3209 Merrill Engineering Building
Salt Lake City, UT 84112

Principal Investigator: Richard W. Shorthill, Ph.D.
Consultants: Paul E. Johnson, PH. D., Thomas F. Greene, Ph.D.
Students: Frank Lander and Karl J. Vogler

Submitted to: Air Force Office of Scientific Research
AFOSR/PKO, Bldg. #410
Bolling Field Air Force Base
Washington, DC 20332

Attention: Dr. Henry R. Radoski

DTIC
ELECTE
MAY 3 1 1990
S D
B

April 1, 1990

90 05 29 061

REPORT DOCUMENTATION PAGE

1. AGENCY USE ONLY (Leave blank)	2. REPORT DATE 2 May 1990	3. REPORT TYPE AND DATES COVERED Final Report/1 Jul 85-31 Jan 89

4. TITLE AND SUBTITLE
Infrared Observations of the Solar System

5. FUNDING NUMBERS
61102E/2311/A1

6. AUTHOR(S)
Dr Richard Shorthill

7. PERFORMING ORGANIZATION NAME(S) AND ADDRESS(ES)

University of Utah
Dept of Mechanical Engineering
3209 Merrill Engineering Building
Salt Lake City, UT 84122

8. PERFORMING ORGANIZATION REPORT NUMBER

AFOSR-TR 90 0645

9. SPONSORING/MONITORING AGENCY NAME(S) AND ADDRESS(ES)

AFOSR/NP, Bldg 410
Bolling AFB DC 20332-6448

10. SPONSORING/MONITORING AGENCY REPORT NUMBER

AFOSR-85-0181

11. SUPPLEMENTARY NOTES

12a. DISTRIBUTION/AVAILABILITY STATEMENT

Approved for public release; distribution is unlimited.

12b. DISTRIBUTION CODE

13. ABSTRACT (Maximum 200 words)

The purpose of this project was to improve the infrared calibration base for infrared detectors. Groundbased infrared measurements of solid-surfaced planetary bodies, such as asteroids, are being used for the calibration of spacecraft detectors. A limitation has been the relatively poor theoretical understanding of thermal emission from these objects. The goal was to: (1) develop a database of ources and, (2) improve or modify the thermal models for these sources to provide a calibration data base for spacecraft infrared detector systems. The technique consisted of five phases: (1) design and construct infrared detector system to be used with and without collecting optics, (2) acquire whole-disk infrared lunar data relative to a laboratory blackbody and tie them to Mars (Venus or Mercury) and Vega, (3) compare with thermophysical models of the moon and modify, (4) acquire infrared asteroid photometry. (5) compare the lunar disk photometry with the asteroid calibrators using photometry and thermophysical models. The Si bolometer is calibrated without optics, attached to the portable telescope drive and Lunar disk measurements made. Next the bolometer is attached to the 90 inch telescope. Lunar scans are made and the remaining objects (planets, stars, asteroids) are measured. ●

14. SUBJECT TERMS Astrophysics, Infrared, Calibration			15. NUMBER OF PAGES 185
			16. PRICE CODE

17. SECURITY CLASSIFICATION OF REPORT UNCLASSIFIED	18. SECURITY CLASSIFICATION OF THIS PAGE UNCLASSIFIED	19. SECURITY CLASSIFICATION OF ABSTRACT UNCLASSIFIED	20. LIMITATION OF ABSTRACT UL SAR

5.0 APPENDICES

Several items are included in the Appendices: (5.1) the report submitted by Frank Lander for his Masters degree and (5.2) the operating manual for the Infrared Laboratories Inc., for Silicon Bolometer # 1059, (5.3) Research Conducted at the Lunar and Planetary Institute by Karl Vogler, (5.4) A paper submitted to *Icarus*, Modeling the Non-Gray-Body Thermal Emission from the Full Moon, (5.5) Surface Roughness and Infrared Emission from Solid-Surfaced Planetary Bodies, a Ph.D. thesis proposal by Karl Vogler, (5.6) Description of the ADC-1 data acquisition and control peripheral and (5.7) Description of the RTD Resistance Temperature Device, and (5.8) some miscellaneous articles.

5.1 **Report: Chopper and Automated Telescope (46 pages).**

5.2 **The Silicon Bolometer Operating Manual (53 pages).**

5.3 **Research Conducted at the Lunar and Planetary Institute.**

5.4 **Modeling the Non-Gray-Body Thermal Emission from the Full Moon.**

5.5 **Surface Roughness and Infrared Emission from Solid-Surfaced Planetary Bodies.**

5.6 **The ADC-1 data acquisition and control peripheral (1page).**

5.7 **The RTD Resistance Temperature Device.(3 pages).**

5.8 **Articles**

5.1 Report: Chopper and Automated Telescope (46 pages).

TABLE OF CONTENTS

Abstract

An infrared (I.R.) optics package designed for a I.R. detector calibration survey will be used in conjunction with the 90 inch telescope at the University of Wyoming, or as a portable, stand alone unit. An important part of this instrument package is a mechanical light beam chopper which rotates with a fixed phase relation with respect to a wobbling secondary mirror in the telescope. A control circuit synchronizes the chopper to an external signal when used at the Wyoming site, or generates an internal reference frequency when used as a portable system. The portable system consists of a small equatorial telescope mount to support the same I.R. instrumentation package, which is used without additional optics. An automated positioning and tracking system encorporates a personal computer to control the movement of the telescope mount via stepper motors attached to the drive axis. The computer is also used to record all data on floppy disc for both fixed and portable systems.

Introduction

The purpose of this project is to design a portion of the instrumentation required for an upcoming infrared survey of astronomical objects. This research is being conducted by Dr. Richard W. Shorthill at the University of Utah in collaboration with Dr. Paul Johnson (University of Wyoming) and Dr. Thomas Green (Boeing Aerospace Company). The object of their research, entitled " Infrared Observations of the Solar System : Calibration ", is to obtain an improved calibration base for spacecraft infrared detectors, and to understand the thermographic properties of asteroids. The uniqueness of this research is that it will tie together thermal models, infrared photometry of potential asteroid calibrators, the moon (an asteroid prototype) , and standard stars taken with the same instrumentation.

The moon, asteroids, planets, satellites and stellar sources are used for infrared calibration of ground based as well as spacecraft detectors. Drs. Shorthill, Johnson and Green are persuing a program for improving the infrared calibration for both groundbased and spacecraft detectors. It is therefore the goal of their research to: (1) develop a database of these infrared sources and (2) improve or modify the related thermal models for these various sources.

An instrumentation platform incorporating a silicon or GeGa bolometer, dewar, blackbody reference, CCD guide scope and additional optics has been designed for these studies. The unit will function as the detector for a large telescope (the 90 inch

telescope at the University of Wyoming) , or as part of a portable, self contained system.

The portable system consists of an equatorial telescope mount, the I.R. instrument package, and a personal computer to control positioning and tracking functions. The computer (an IBM PCXT or equivalent) also records data from the bolometer, CCD, temperature and pressure probes for both fixed and portable operation.

The infrared detector system is designed to be used both with and without collecting optics. The research concept is shown diagrammaticly on the following page. The bolometer is calibrated in the laboratory without optics and attached to the portable telescope drive where whole lunar disc measurements are made. The bolometer is then attached to the Wyoming telescope for measurements of the remaining objects.

INSTRUMENTATION PROJECT

Two components of the I.R. system were designed by the author as an instrumentation project. The design and construction of a light beam chopper and control electronics comprises the first phase of the project. The second phase involves the design of an automated telescope and the selection of the components for this system.

The chopper is an important component of the infrared optics package. A silvered chopping disc alternately directs light from the object of interest into either the I.R.

2

detector or a photomultiplier. Radiation from a reference blackbody source and the background sky are also admitted into the into the bolometer in sequence. The chopper electronics synchronizes the chopper blade with a wobbling secondary mirror, when used with the 90 inch telescope, in order to sweep the infrared source and the local background radiation. For portable operation, a fixed chopping frequency can be selected.

The automated telescope mount consists of a commercial equatorial telescope retrofitted with stepper motors to control the movement of the two axis of motion. An "intelligent" stepper motor control card occupies a slot within the the IBM PC to permits software control of the telescope mount. This control card allows the computer to handle data manipulation, even as the drive motors are running. An A/D card converts analog inputs from the bolometer as well as temperature and pressure sensors into digital form for storage on a floppy disc.

The design of the telescope drive, as well as the matching and selection of components, completes the second phase of the project.

INFRARED OBSERVATION OF THE SOLAR SYSTEM

RICHARD W. SHORTHILL, P.I.   UNIVERSITY OF UTAH
PAUL E. JOHONSON, CONSULTANT   DEPT. MECHANICAL AND INDUSTRAIL ENGINEERING
FRANK LANDERS, STUDENT   SALT LAKE CITY, UTAH 84112
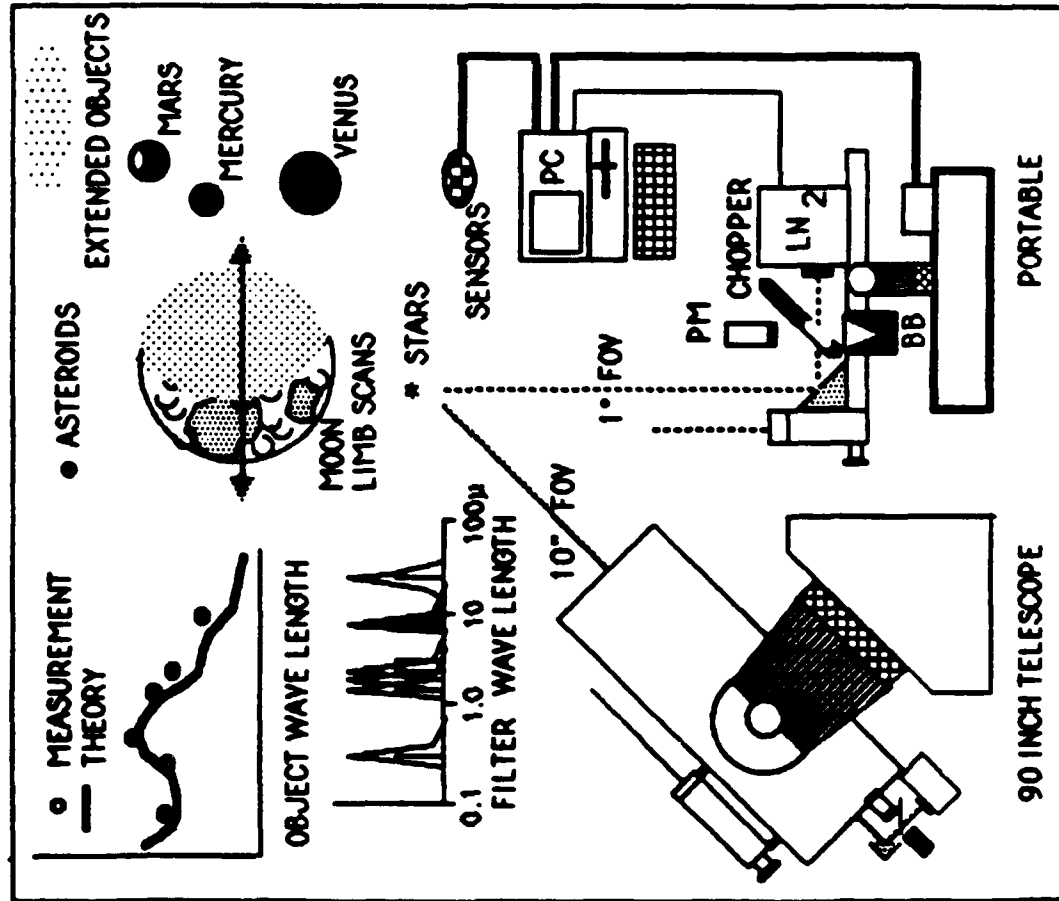
RESEARCH AREAS

O INFRARED DETECTOR CALIBRATION
O INFRARED WAVE LENGTHS 5-30 µ
O ASTEROIDS
O LUNAR LIMB SCANS
O OTHER OBJECTS
O THERMAL MODELS

ANTICIPATED ACCOMPLISHMENTS

O IMPROVED CALIBRATION
O SPECTRAL DISTRIBUTION OF OBJECTS
O SYSTEM OF CALIBRATION OBJECTS
O IMPROVED THERMAL MODELS
O EFFECT OF PARAMETERS (e.g.)
 • DEWAR-TEMP., PRES., ETC.
 • ATMOSPHERE-TEMP., PRES., ETC.

POTENTIAL AIR FORCE APPLICATIONS

O IMPROVED OBJECT IDENTIFICATION
 • NATURAL
 • MAN MADE
O IMPROVED CALIBRATION METHODS
 • GROUNDBASED
 • SPACECRAFT
O IMPROVED THERMAL MODELS

EXTENDED OBJECTS
MARS
MERCURY
VENUS

• ASTEROIDS

MOON LIMB SCANS

* STARS

SENSORS

PC

PM
CHOPPER
LN 2
BB
1° FOV

PORTABLE

○ MEASUREMENT
— THEORY

OBJECT WAVE LENGTH

0.1   1.0   10   100µ
FILTER WAVE LENGTH

10⁻ FOV

90 INCH TELESCOPE

EQUIPMENT AND CONCEPTS

4
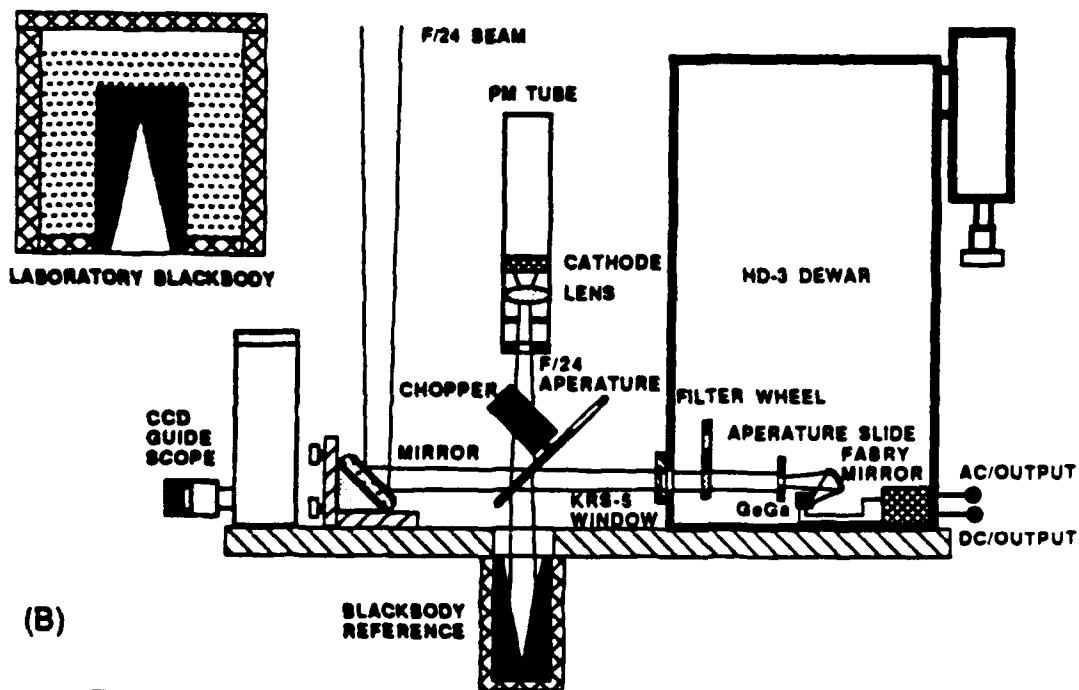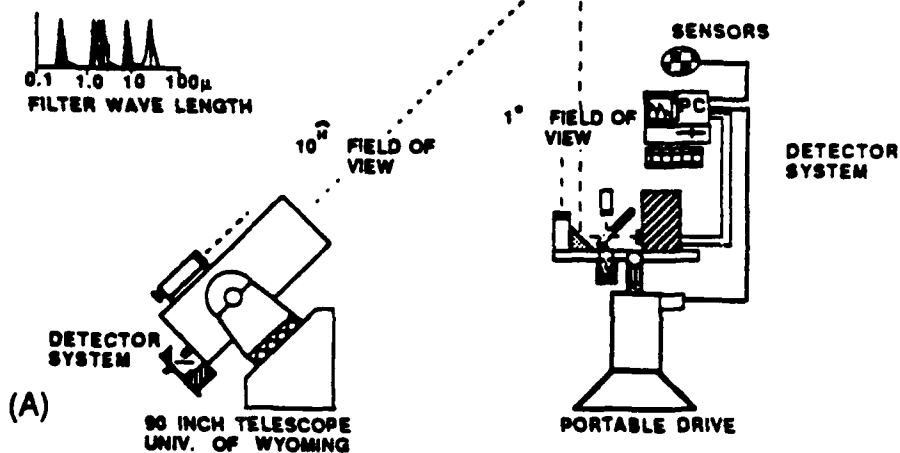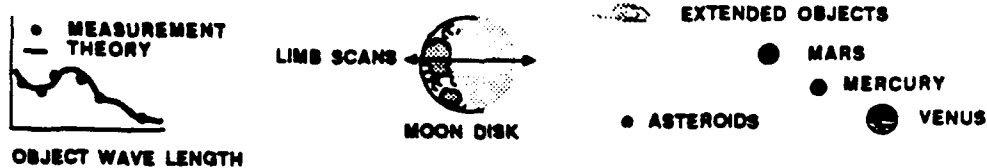
Experimental approach is shown in (A) above. The GeGa bolometer
system is shown at the bottom in (B).

F/24 BEAM

PM TUBE

CATHODE

LENS

F/24
APERATURE

CHOPPER

ALIGNMENT
MIRROR

KRS-5
WINDOW

HD-3 DEWAR

7.00 IN

12.50 IN

FILTER WHEEL

APERATURE SLIDE

FABRY
MIRROR

Ge

BLACKBODY

≈ 17.00 IN

6
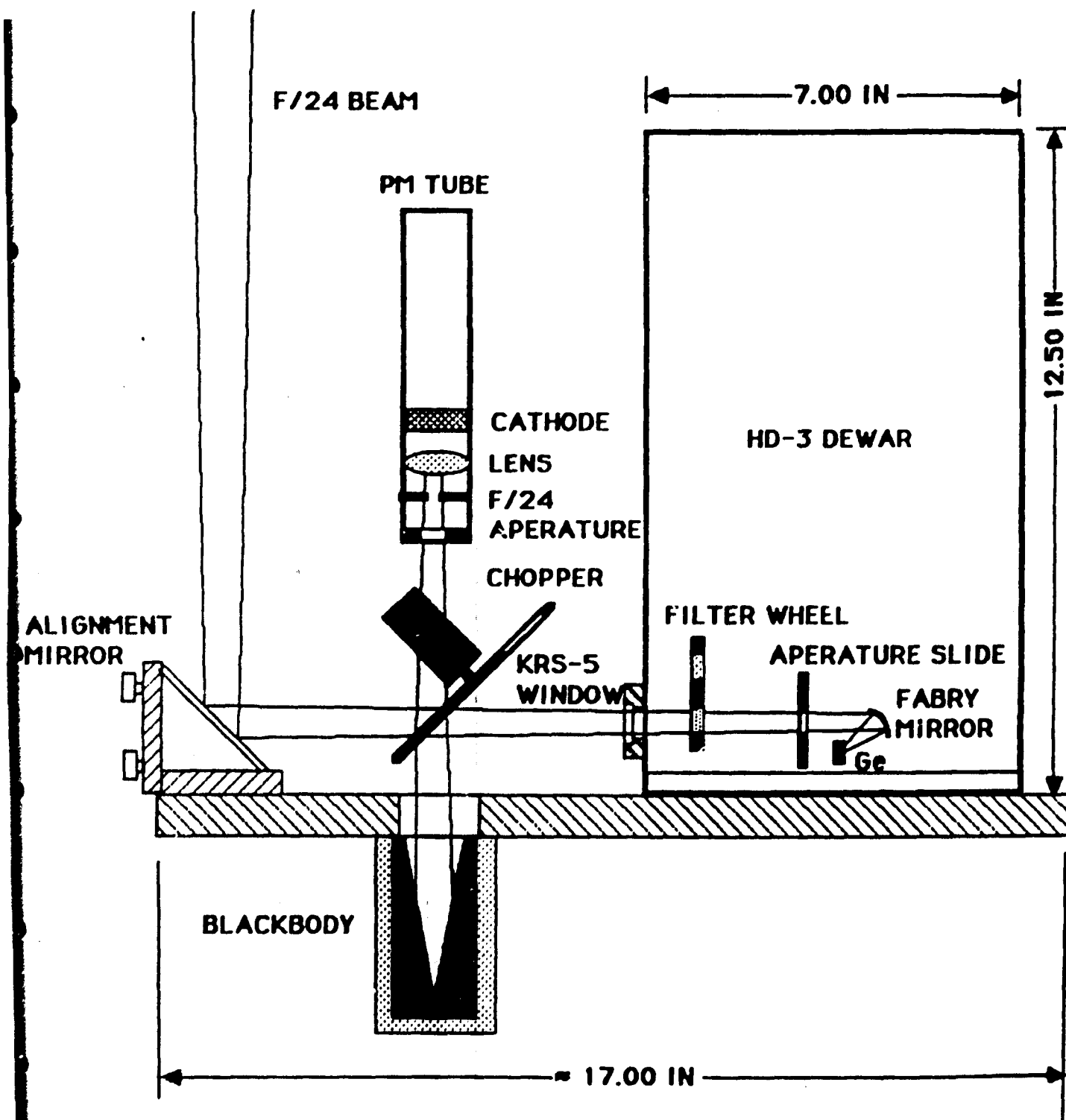
OPERATOR'S MANUAL

FOR THE

LIGHT BEAM CHOPPER AND CONTROL

Phase - Locked / Variable Speed Light Beam Chopper

Description

This unit is designed for low frequency mechanical chopping of light. The chopper covers a frequency range from 8Hz. to 25Hz. using a two blade chopping disc. Higher frequencies are available with the use of multiple slot wheels.

The phase-locking of the chopper to an input square wave is achieved with minimal phase jitter. The phase relationship between reference and chopper is continuously variable between approximately zero and ninety degrees, and an additional ninety degrees can be added to cover a full range of adjustment. The adjustable phase relationship and out-of-lock conditions are indicated by an LED. An internal reference oscillator permits free run operation over the lower frequency range, while a digital frequency readout displays the actual running frequency of the chopper. The frequency is displayed in Hertz, with a resolution of 0.1Hz.

The chopper head consists of a d.c. drive motor with gear reduction, the chopper blade and signal conditioning electronics for the optical blade position sensor. An infrared LED / phototransistor pair triggers a TTL level signal corresponding to the position of the chopper blade.

Features

* 8 - 25 Hz operation...... modifiable for higher frequencies

* Phase - Locking to external TTL signal

* Digital readout of chopping frequency to 99.9 Hz.

* Internal frequeny reference for free run operation

* Phase, lock-in indicator

* Adjustable Phase

Specifications

CONTROL UNIT

Input Voltage : +,- 15 V

Input Current : 150mA

Frequency Range :   8-25 Hz   (2 blade chopper)

16-50 Hz   (4 blade chopper)

24-75Hz   (6 blade chopper)

Phase Jitter :   less than 2% nominal

Internal Frequency Stability :   .005% per degree C

Dimensions :   5.75" , 4" , 2.5"

Chopper Blade : 102 mm dia. 2 blade

Chopper Motor : d.c. with gear reduction

Theory of Operation

The chopper control uses the principle of a phase-locked loop (PLL) circuit to synchronize the chopper to either an external or internal reference frequency. Its operation differs from that of the self contained I.C. variety of PLL in that it is the frequency of the chopper that is locked into an external signal, rather than the frequency of a voltage controlled oscillator (VCO). In fact , the chopper-position detector combination behaves as a VCO in this circuit.

Coherent Detector

The coherent detector consists of a logical Exclusive OR gate (XOR) with a low pass filter at the output. Two signals enter the XOR ; the reference signal (either external or internally generated) and the chopper position reference signal. The position signal originates from the LED / photodiode pair mounted on the chopper head. A Schmitt trigger adjusts this signal to TTL levels and permits the addition of a quarter revolution phase shift by the series connection of two inverting triggers.

The XOR function is actually comprised of four NAND gates. A logic diagram of the XOR appears below.

(c)
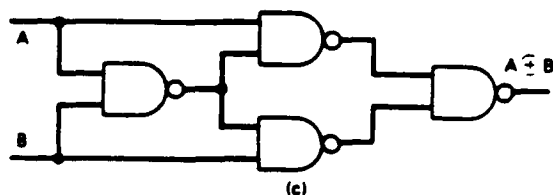
$A \oplus B = C$

A	B	C
0	0	0
0	1	1
1	0	1
1	1	0

For a two - input XOR gate, the output is high if either of the inputs is high, but not if both inputs are high. Therefore, the integrated (d.c. averaged) output is zero when both signals are coherent and is a maximum when the signals are 90 degrees out of phase. This "error" signal at the output of the low pass filter is proportional to the phase difference between the two signals.

The error signal is buffered by a unity gain,non-inverting amplifier to prevent loading of the low pass lead-lag filter. An LED at the amplifier output indicates the magnitude of the error signal when the chopper is locked in. For the unlocked condition,the indicator lamp flickers at a rate which is proportional to the difference between chopper and reference frequency . This makes it easier to adjust the chopper rate to within the lock-in range.

A second operational amplifier sets the running speed of the chopper. A 10k speed adjust potentiometer varies the the d.c. output level of the amplifier. The summing configuration adds the error signal to the speed set voltage, thus increasing the speed of the chopper when the chopper lags the reference signal. The sensitivity adjustment determines the gain of the error signal, i.e. the error voltage vs. phase angle ratio.

The final stage of the circuit is a power amplifier. A power transistor follower at the output of the op amp provides the high current gain that is required to drive the chopper motor.

Internal Frequency Reference

A square wave generator provides the frequency reference when an eternal signal is not available. The requirements for the signal are that it be zero to five volts and that it be symmetric (50% duty cycle). A 555 timer generates a signal that is quite stable and is easily adjusted using an external potentiometer, however the output is not symmetric. An edge triggered D-type flip-flop wired as a divide by two circuit converts the 555 output into a symmetric square wave. A square wave is required by the coherent detector.

Digital Frequency Readout

The frequency readout circuit utilizes a single chip tachometer (frequency to voltage) circuit to convert the chopper output signal into a d.c. voltage level which is proportional to frequency. This device performs well at higher frequencies, but a significant ripple voltage (which is inversely proportional to the frequency) appears at the lower range of the chopper (8-20 Hz). Attempts to remedy this problem by adjusting the values of the components that comprise the tachometer circuit result in a cleaner output voltage but introduce an unacceptably long response time. The solution is to add a low pass filter to the output of the tachometer circuit. The ripple is reduced to levels that are below the resolution of the readout, while maintaining a fast response time. The output gain is calibrated by a trim pot so that 10mV corresponds to 1 Hz..

A monolithic digital voltmeter circuit (DVM) displays the tachometer output voltage on a three digit, 7-segment LED display. The least significant digit , corresponding to one millivolt, represents one tenth of one hertz. The integrated circuit uses a pulse

11

modulation analog-to-digital conversion technique that requires no external precision components. The conversion rate is controlled by an internal oscillator , the frequency of which can be set by an external RC network. The ADD3501 has been designed to drive 7-segment multiplexed LED displays directly with the aid of external digit buffers and segment resistors. A two volt I.C. precision voltage reference circuit provides the reference level for the DVM.

Operation

External Reference

The use of the chopper control is straightforward. For normal, externally referenced operation, complete the following steps;

(1) Connect the power supply to the banana plugs on the right side of the control unit. The chopper requires +12 to +15V, a ground connection, and -12 to -15V. The power supply must be rated for at least 200mA.

(2) Connect the frequency reference to the ref. input BNC connector on the right hand side of the control box. The reference signal must be a symmetric square wave, 0-5V.

(3) Connect the control to the chopper head by attaching the coax and double wire leads to the proper connections on the left hand side of the control box. Make sure that the double wire leads are connected to the proper terminals.

(4)   Flip the reference switch to " external ".

The unit should now be ready to operate when the power supply is turned on. The LED indicator lamp will flicker as long as the chopper frequency differs from the ref. frequency. To lock the chopper onto the reference signal, turn the speed adjust knob in the direction that decreases the flickering rate of the LED. As the lock-on frequency is approached, the flickering rate decreases until the chopper is within the capture range. When lock-in is achieved, the flickering should abruptly cease. A steady light indicates lock-in . The brightness of the LED is proportional to the phase difference between the chopper and the ref. signal (dim: small angle, bright: approaching 90 degrees). Fine adjustments of the phase angle are made by turning the speed adjust knob in small increments. To add an additional 90 degrees, flip the phase switch in either direction.

Internal Reference

Follow the instructions for externally referenced operation except :

(1) Flip the reference switch to " internal ".

(2)   Select the desired operating frequency using the " Int. Freq. " adjustment knob.

The final lock-in adjustments are made as before. Note that the frequency readout displays the reference frequency (internal or external). Frequencies between 100-199.9Hz are displayed without the most significant digit .

13

Internal Adjustments

All controls used in normal operation are located on the outside of the chopper control cabinet. However,occationally it may be desireable to adjust an internal trim pot or to make other modifications.

Adjusting the sensitivity trim pot will alter the behavior of the chopper to a small degree. The adjustment affects the manner in which the chopper " grabs " the ref. signal and how rapidly it responds to a change in frequency. The adjustment is not critical, but there may arise a problem with overshooting if the error signal is too large. This adjustment changes the magnitude of the error signal, which is analagous to the restoring force of a simple harmonic oscillator. Oscillation about the reference phase is called " phase jitter ". The damping of the system is due in large part to the mechanical properties of the motor.

The 555 timer may be adjusted to provide a higher maximum reference frequency by adjusting the ratio of the two resistors, or by replacing the timing capacitor (probably the easier solution).
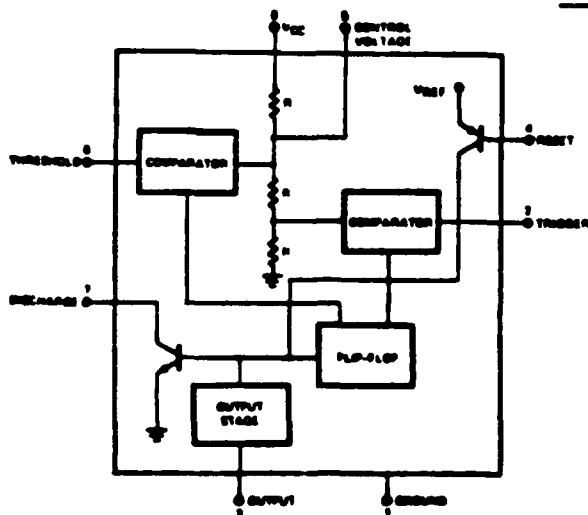
ASTABLE OPERATION

If the circuit is connected as shown in Figure 2a (pins 2 and 6 connected) it will trigger itself and free run as a multivibrator. The external capacitor charges through R_A and R_B and discharges through R_B only. Thus the duty cycle may be precisely set by the ratio of these two resistors.
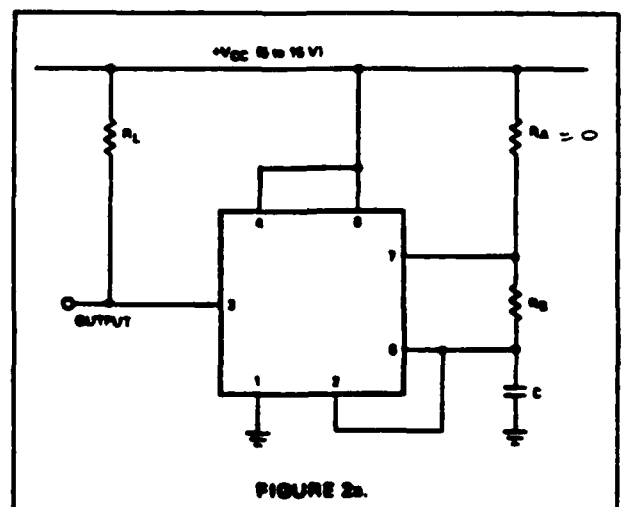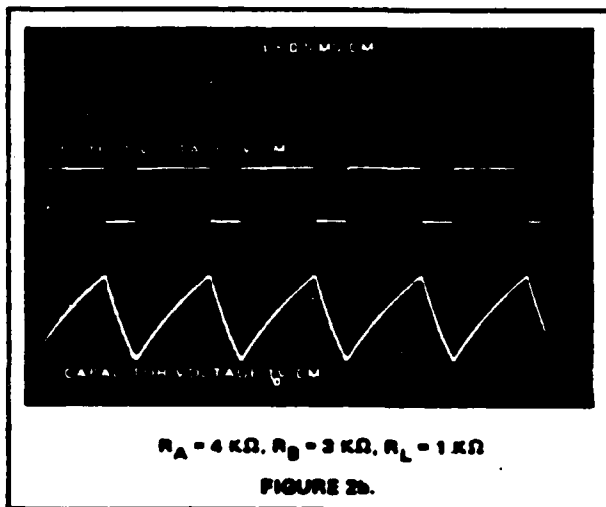
555 – TIMER

14

FIGURE 2a.

APPLICATIONS INFORMATION (Cont'd)

In this mode of operation, the capacitor charges and discharges between $1/3\ V_{CC}$ and $2/3\ V_{CC}$. As in the triggered mode, the charge and discharge times, and therefore the frequency are independent of the supply voltage.

Figure 2b shows actual waveforms generated in this mode of operation.

$$R_A = 4\ K\Omega,\ R_B = 3\ K\Omega,\ R_L = 1\ K\Omega$$

FIGURE 2b.

The duty cycle is given by:

$$D = \frac{R_B}{R_A + 2R_B}$$

The charge time (output high) is given by:

$$t_1 = 0.685\ (R_A + R_B)\ C$$

and the discharge time (output low) by:
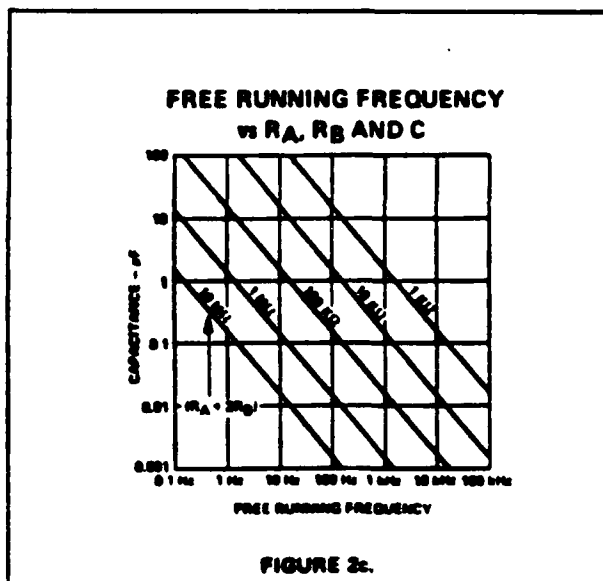
$$t_2 = 0.685\ (R_B)\ C$$

Thus the total period is given by:

$$T = t_1 + t_2 = 0.685\ (R_A + 2R_B)\ C$$

The frequency of oscillation is then:

$$f = \frac{1}{T} = \frac{1.46}{(R_A + 2R_B)\ C}$$

and may be easily found by Figure 2c.

FREE RUNNING FREQUENCY
vs R_A, R_B AND C

FIGURE 2c.

The tachometer circuit should not require any adjustments, but specifications are provided below. The gain adjustment pot on pin 4 of the 2907 has been calibrated for 10mV per Hertz.
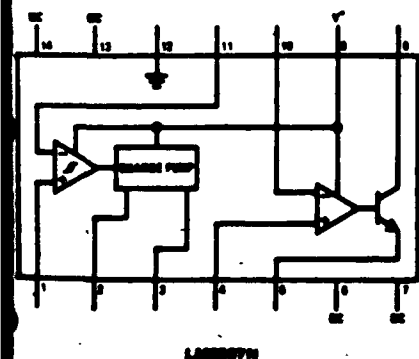
LM2907N

Basic f to V Converter

The operation of the LM2907, LM2917 series is best understood by observing the basic converter shown in Figure 3. In this configuration, a frequency signal is applied to the input of the charge pump at pin 1. The voltage appearing at pin 2 will swing between two values which are approximately $1/4\ (V_{CC}) - V_{BE}$ and $3/4\ (V_{CC}) - V_{BE}$. The voltage at pin 3 will have a value equal to $V_{CC} \cdot f_{IN} \cdot C1 \cdot R1 \cdot K$, where K is the gain constant (normally 1.0).

The emitter output (pin 4) is connected to the inverting input of the op amp so that pin 4 will follow pin 3 and provide a low impedance output voltage proportional to input frequency. The linearity of this voltage is typically better than 0.3% of full scale.

FIGURE 3. Basic f to V Converter
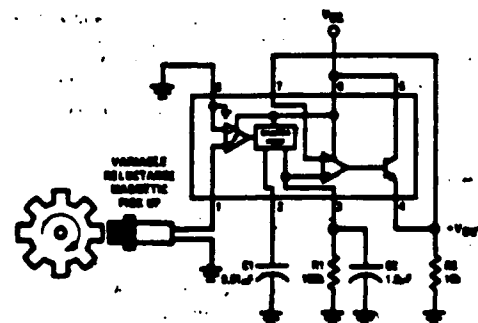
Choosing R1, C1 and C2

There are some limitations on the choice of R1, C1 and C2 (Figure 3) which should be considered for optimum performance. C1 also provides internal compensation for the charge pump and should be kept larger than 100 pF. Smaller values can cause an error current on R1, especially at low temperatures. Three considerations must be met when choosing R1.

15

First, the output current at pin 3 is internally fixed and therefore V3 max. divided by R1, must be less than or equal to this value.

$$R1 \geq \frac{V3 \text{ max}}{I_{3MIN}}$$

where V3 max is the full scale output voltage required. I_{3MIN} is determined from the data sheet (150μA)

Second, if R1 is too large, it can become a significant fraction of the output impedance at pin 3 which degrades linearity. Finally, ripple voltage must be considered, and the size of C2 is affected by R1. An expression that describes the ripple content on pin 3 for a single R1, C2 combination is:

$$V_{RIPPLE} = \frac{V_{CC}}{2} \cdot \frac{C1}{C2} \left(1 - \frac{V_{CC} \cdot f_{IN} \cdot C1}{I_2}\right) p\text{-}p$$

It appears R1 can be chosen independent of ripple, however response time, or the time it takes V_{OUT} to stabilize at a new frequency increases as the size of C2 increases, so a compromise between ripple, response time, and linearity must be chosen carefully. R1 should be selected according to the following relationship:

C1 is selected according to:

$$C1 = \frac{V3 \text{ Full Scale}}{R1 \cdot V_{CC} \cdot f_{FULL SCALE}}$$

Next decide on the maximum ripple which can be accepted and plug into the following equation to determine C2:

$$C2 = \frac{V_{CC}}{2} \cdot \frac{C1}{V_{RIPPLE}} \left(1 - \frac{V3}{2}\right)$$

The DVM circuit includes several trim pots which should not be altered. The DVM and its voltage reference have been calibrated so that the least significant digit reads in millivolts.

ADD3601 3½-Digit DVM Block Diagram
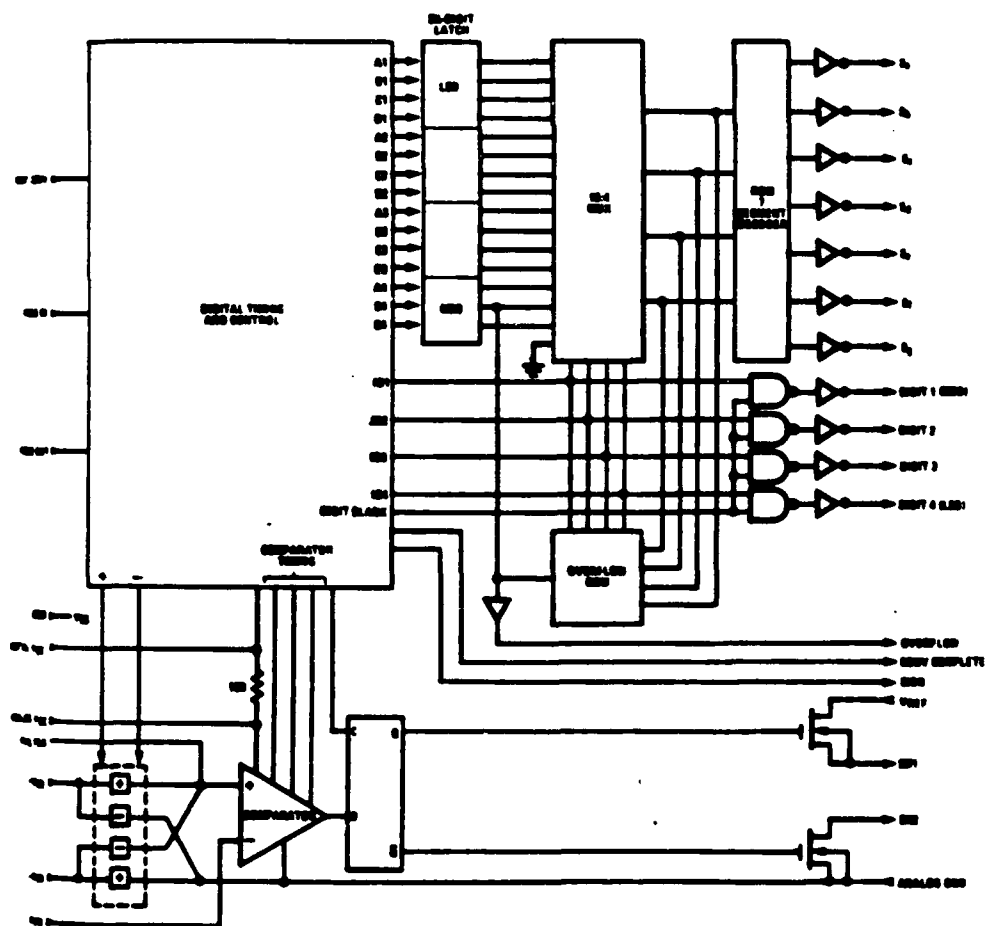
PLL / FREQUENCY REF. CIRCUIT

FREQUENCY READOUT

F. LANDERS
6-86

18

F. LANDERS
6-86

180Ω (8 each)

a
f
b
g

Driver
R+
c
d
e

4d

3d

2d

7-SEGMENT LED

PIN CONNECTIONS
FRONT VIEW

g f a b

e d c dp

+8

1k

OUT

15k

330

optical interrupter

+5

OPTICAL PICKUP CIRCUIT
- CHOPPER HEAD

+5v
phase shift resrn D1
phase switch
9 6 6

(top)

LED D5 D5 D4 a b c d

RIBBON CABLE
CONNECTOR

TAPPED FOR
4-40 SCREW
(3 EACH)

90°

120°

1.313

0.407

0.230

0.32

0.125

0.750

0.125

0.375

0.625

TAPPED FOR
SET SCREW 2-56
(2 EACH)

SHAFT HOLE
0.116 DIA

CHOPPER BLADE HUB (1 EACH)

102

A
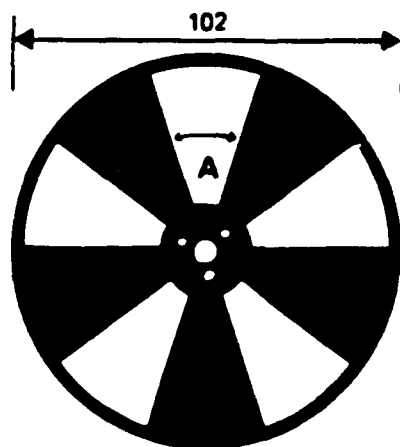
Dimensions in mm

Aperture 'A'

2 slot disc = 50mm
5 slot disc = 20mm
10 slot disc = 10mm
30 slot disc = 3mm

20

TAP 10-32 (1 EA)
DRILL THROUGH

1.025 DIA

0.500

3.000

2.200

0.500

1.600

1.000

0.120
0.400

0.250

0.750

TAP1/4-20 (4 EA)
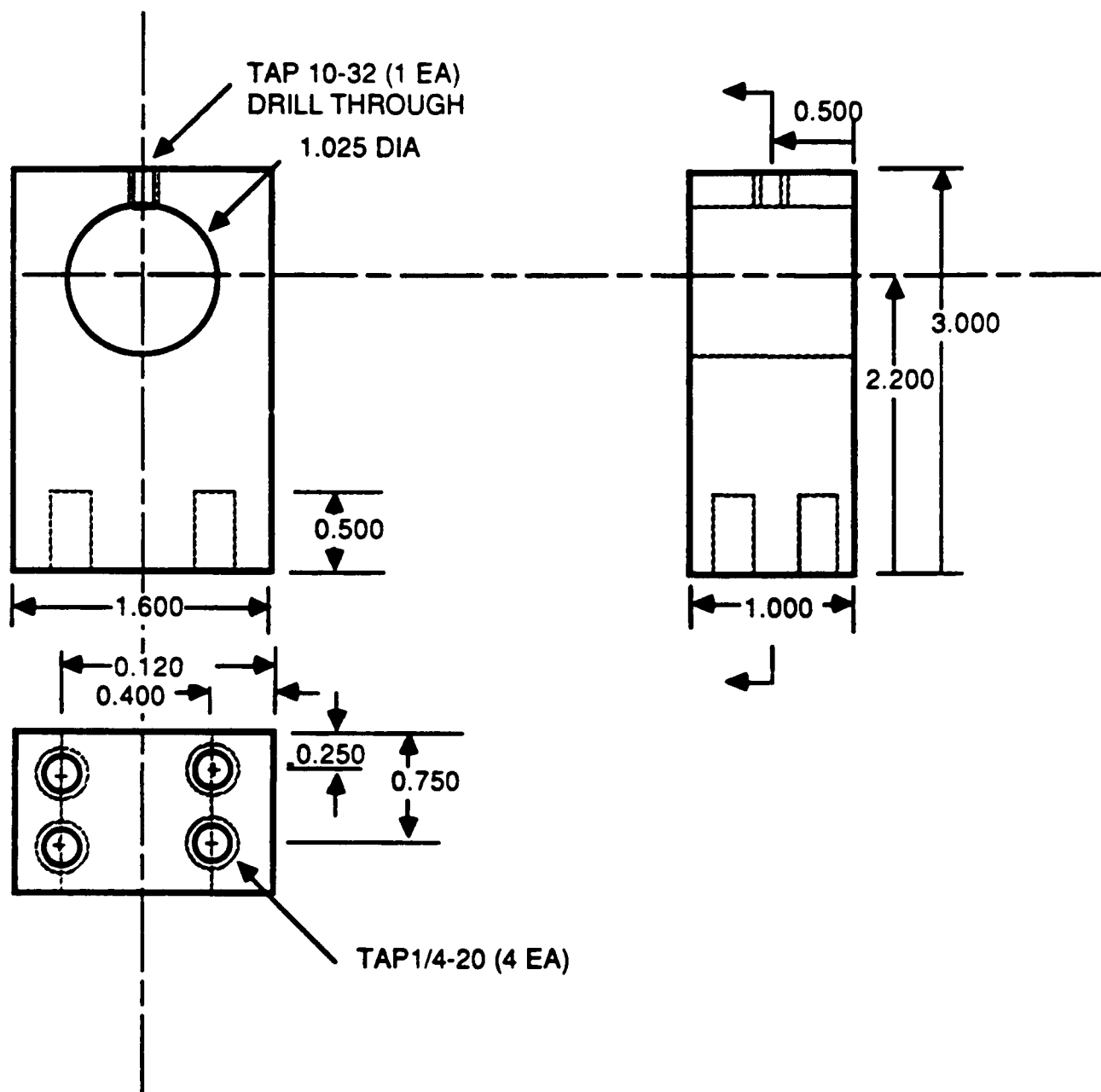
CHOPPER MOTOR SUPPORT POST (1 EACH)
MATERIAL: Al
SPRAY FLAT BLACK

21

AA'

COUNTER DRILL
FOR 1/4-20 ALLEN
HEAD SCREW (4 EA)

2.00

1.00

TAP 4-40 (2 EA)

1.00

CLR 1/4 (4 EA)

A

A'

1.900

TAP 4-40

1.400

CLR 0.40

0.950

0.575

TAP 4-40

1.100

1.500

1.900

3.00

0.50

BASE (1 EACH)-TO FIT
CHOPPER MOTOR SUPPORT POST
MATERIAL: AI
SPRAY FLAT BLACK

AFOSR   IR-CONTRACT
UU #5-28012-6490 (FABRICATION)
F. LANDERS (GRADUATE STUDENT)
R.W.SHORTHILL (PRINCIPAL INVESTIGATOR)
16 APRIL 1986

22

AUTOMATED TELESCOPE DRIVE

Background

The open-loop stepper drive system was selected over several other possibilities. An alternative approach is the closed-loop control of D.C. or brushless motors. Such a system utilizes a position sensor for feedback and uses the feedback to close the control loop around the motor. Closed loop systems require a controller that observes the motor position, closes the loop, and maintains loop stability. Closed loop systems are typically difficult to "tune" to a particular system and require expensive shaft encoders.

A second approach to stepper motor control would have used a chip level stepper controller as part of a custom printed circuit board for the IBM PC. It was decided that the savings in cost would be minimal and that the time required for the design of a PC board was prohibitive.

Description

The components for the automated telescope drive were selected to meet the requirements of performance, compatability, time limitations and cost considerations. A description of the individual components and their specifications can be found in the following pages. The control software has not been developed at this time.

Computer

The heart of the telescope control is a personal computer. An IBM PCXT has been

23

chosen for the initial testing, but may be substituted for an IBM " work alike" personal computer at a later date.

Controller Card

An " intelligent " stepper motor interface card will occupy a slot within the PC. The Rogers Labs " PCMotion " controller performs many of the lower level control functions such as setting a ramp profile and mainaining a specific step rate. The computer is free to accept data or adjust the tracking rate while the telescope drive motors are running. A program operating in the foreground directs the stepper controller using single line BASIC commands. The controller board also has 32 discrete input / output ports. These can be used with limiting switches, or as shaft encoder inputs should they be needed.

Stepper Driver

The driver circuit for the stepper motors consists of an externally mounted board connected to the computer via ribbon cables. A clock and translator circuitry convert direction and mode signals from the controller into the proper stepping sequence for each coil of the two stepper motors. Two separate driving circuits allow each motor to run independently. A 24V, 2 amp unregulated power supply is required to drive the motors.

'PCMotion' Peripheral Adapter Specifications
Rogers Labs PCMotion I 432 I/O Stepper Control Plug-In Board

Features :

* Controls (2) stepper motors with mode and direction

* Software controls ramping, velocity,direction and distance using single line call statements from BASIC. Run time routines written in assembly language . Interupt driven operation minimizes CPU time.

* Requires (1) full slot in IBM PC/XT or work alike (64k memory minimum)

Specs :

System

(3) 34 pin connector I/O ports :

(1)   motion control port

(2)   ports, (16) channel discrete TTL I/O configurable as input or output

(1) full slot required, uses +5v, 500mA from internal power supply

Software

* Assembly language device handlers

* Single line call statements from BASIC

* Discrete I/O read and write calls, 2 digit BCD

* (2) motor calls for simultaneous ramp operation

* HELP and demo programs included on 5.25" disc

PRICE : $ 495.00

Rogers Labs R2D23 Dual Axis Stepper Motor Driver

The R2D23 board was designed to work with the PCMotion control card for driving two four phase stepper motors (up to 1 Amp per phase). It contains the translator circuitry and power drivers, as well as terminal strips for connecting to the motors and power supply. Wiring is also provided for two optical shaft encoder inputs should they be required.

Features:

* Optically isolated inputs

* HEXFET output driver transistors diode protected from inductive spikes

* Two input channels for optical encoder feedback

* Industrial barrier strip terminals for wiring

Input:

Connects to PCMotion controller via standard 34 line ribbon cable.

Power Supply :

External power supply required : 1 Amp, 24v unregulated Logic power (5v) supplied by ribbon connector.

Dimensions :

2 3/4 " by 6 7/8" , designed for mounting on 'snaptrack' channel.

PRICE : $ 177.00

' Hurst' Model AS-300 D.C. Stepping Motors
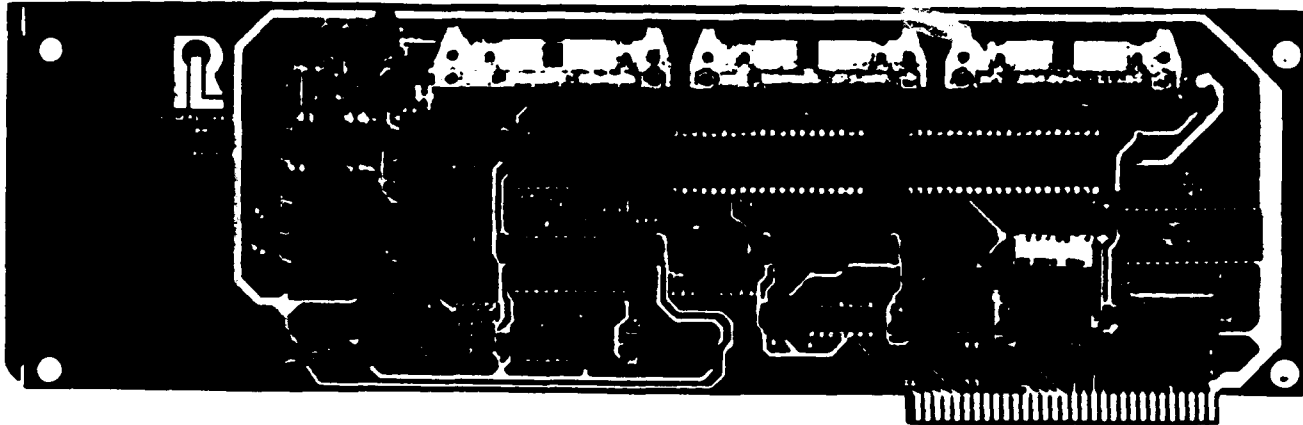
4-Phase Type, With Gear Reduction, 0.025 degree Step Angle

Holding torque .... 150 oz-in
Nominal voltage 12
Resistance per winding .... 100 ohms
Speed (rpm) @ 200 p/s ... 0.83

PRICE : $ 45.00 ea

I 432 I/O
**4 AXIS STEPPER DRIVER
WITH 32 I/O BOARD**

PCMotion™ PERIPHERAL ADAPTER
FOR THE IBM PC® FAMILY OF COMPUTERS

- **Precision Motion Control and Digital I/O**
- **Four Axis Stepper Motor Driver with Mode and Direction**
- **Two Encoder Input Channels with Direction and Index**
- **32 Discrete I/O Channels: Either Input or Output**
- **Standard System Software Emphasizes Ease of Use**

The PCMotion board, when plugged into any available slot in your IBM PC computer, gives you industrial and robotic control capabilities which have been field tested and proven over a period of years. Used with Rogers Labs or other industry standard peripheral devices, it can monitor and control machinery, processes, and equipment with an ease and economy not previously available.

System software, which is furnished on 5¼ diskette is compatible with PCDOS versions up through 2.10. Routines are included for: system configuration, application software, initialization, motor control and discrete input and output. All run-time routines are written in assembly language, and make liberal use of interrupts, which produces high speed background hardware operation with the user application program operating in the foreground. All system commands are one line call statements in your BASIC (or other HOL) application program and combine flexibility with ease of use.

External hardware interfacing is accomplished through three ribbon cable connectors, each representing an interface port. All external hardware features optical isolation, and signal leads are separated by grounded conductors in order to minimize transmission of electrical process noise into the computer and to eliminate cross-talk between adjacent signal channels.

The stepper motor control port can output four gated pulse trains from two independent pulse generators; providing independent control of four axes of positioning at two independent speeds. Four latched outputs provide direction control for four motors, or mode and direction control when two motors are being driven. The two high speed encoder inputs each has associated discrete inputs for encoder index signals and externally derived encoder rection. All signals for this port are grouped in connector P1.

The discrete I/O ports are routed through connectors P2 and P3. Each carries sixteen signals which are programmed as input or output in groups of eight. Two of the signal lines can be jumper connected to act as real time interrupt inputs for instant shutdown or for freezing all outputs.

Board power is jumper selectable from either the computer power supply or an external regulated supply. Switch selectable addressing and relocatable code permit operation with any memory size.

28

ROGERS LABS

2727-E SO. CRODDY WAY
SANTA ANA, CA 92704
TEL. (714) 751-0442

I 432 I/O
4 AXIS STEPPER DRIVER
WITH 32 I/O BOARD
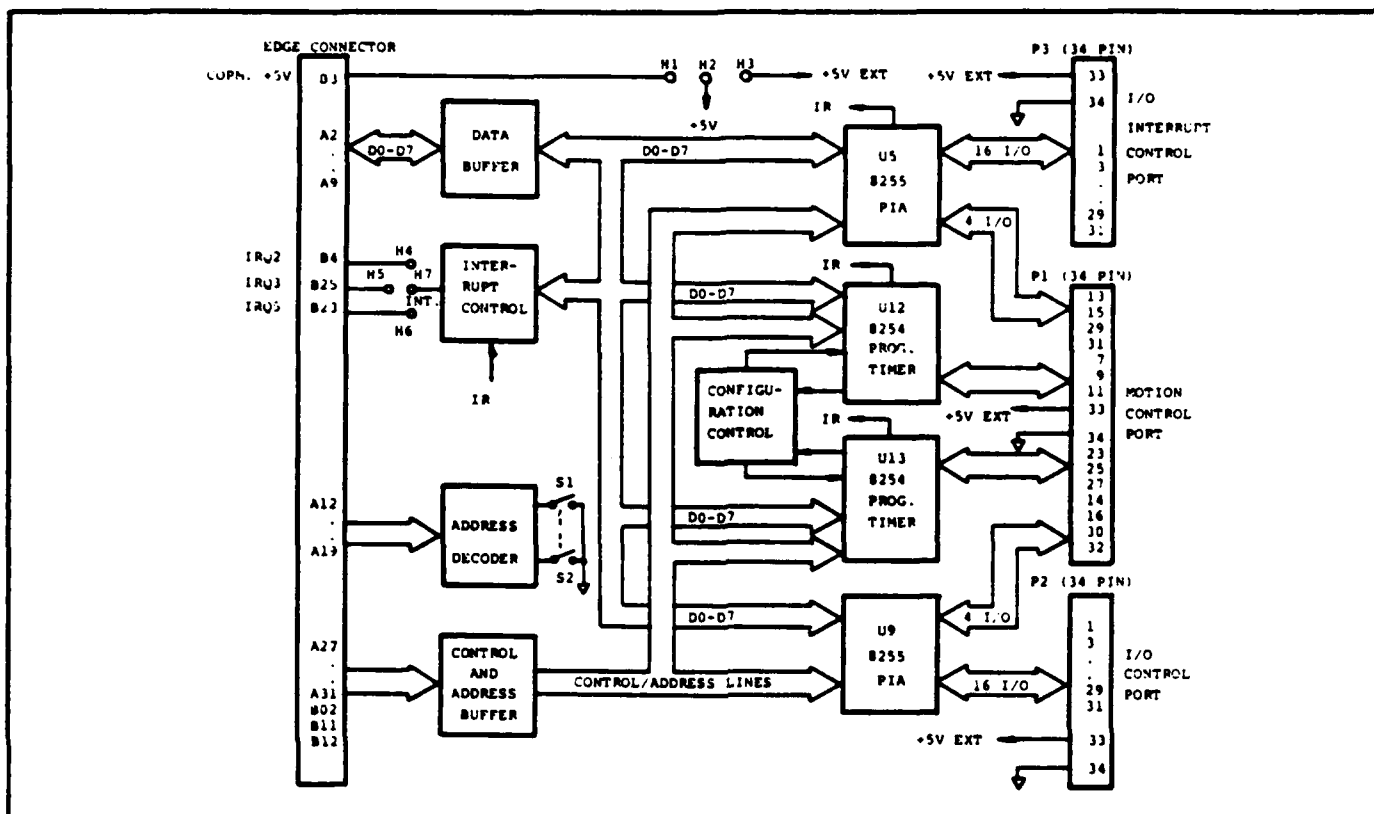
SPECIFICATIONS:

Motion Control Port

- 4 axes of stepper motor control
- 2 high speed encoder input channels
- 8 dedicated discrete I/O signals
- Plug compatible with Rogers Labs' R2 series drivers

Discrete I/O Ports

- 2 connectors, each carrying sixteen channels
- TTL logic levels
- All channels software-configurable as either input or output
- 2 real time interrupts for instant system reset
- Plug compatible with standard solid state relay racks

Software

- System software supplied on 5¼" diskette
- Device handlers written in machine language for speed
- System commands are in the form of one line calls
- Interrupt driven operation minimizes CPU loading

Power

- 5 volts regulated 500 ma. typical (varies with operation)

Multiple board operation provided by jumper selectable interrupt level.

PCMotion BLOCK DIAGRAM

30

ROGERS LABS
2710 SO. CRODDY WAY
SANTA ANA, CA 92704
TEL. (714) 751-0442
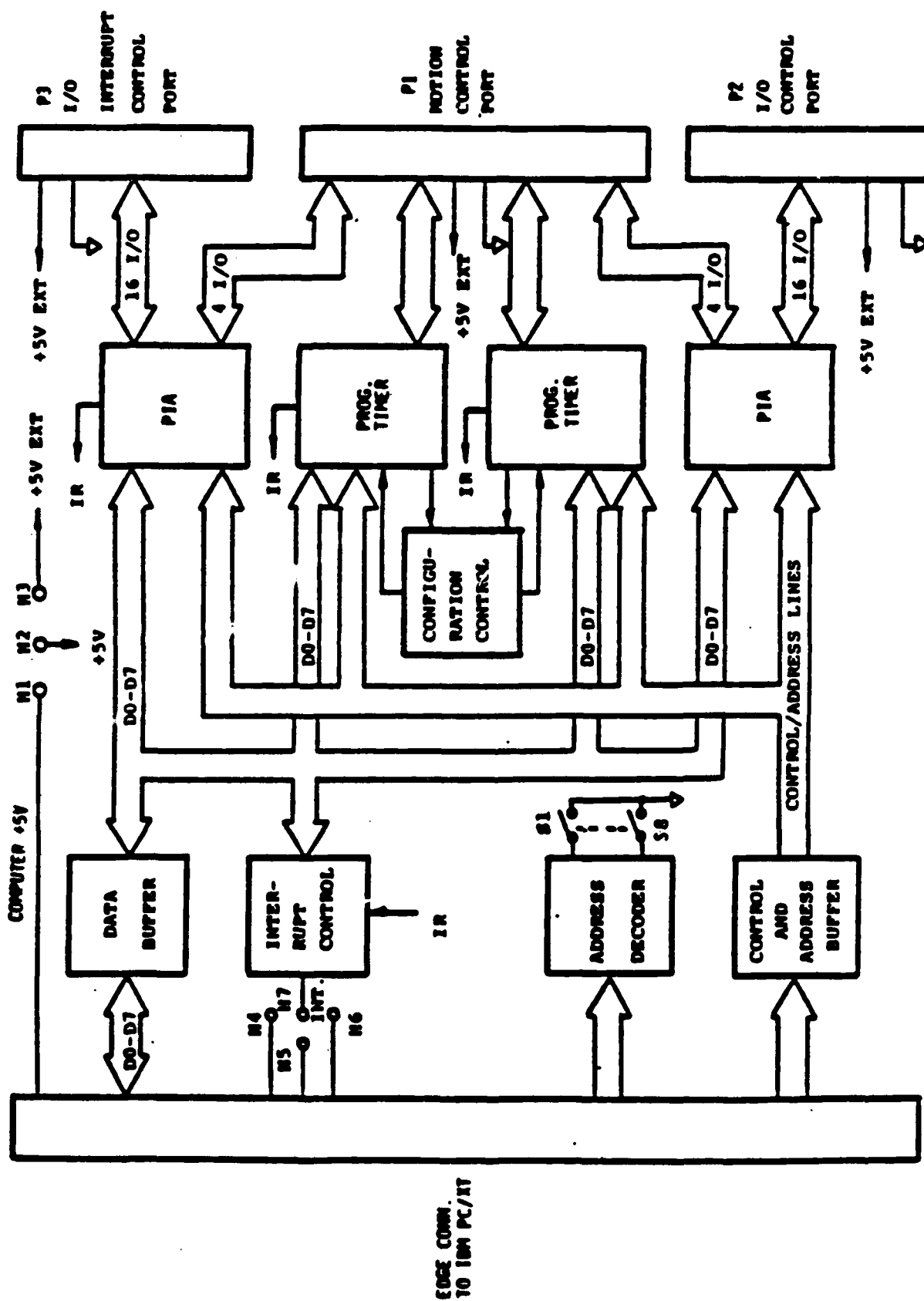
R2D23
DUAL AXIS STEPPER
MOTOR DRIVER BOARD
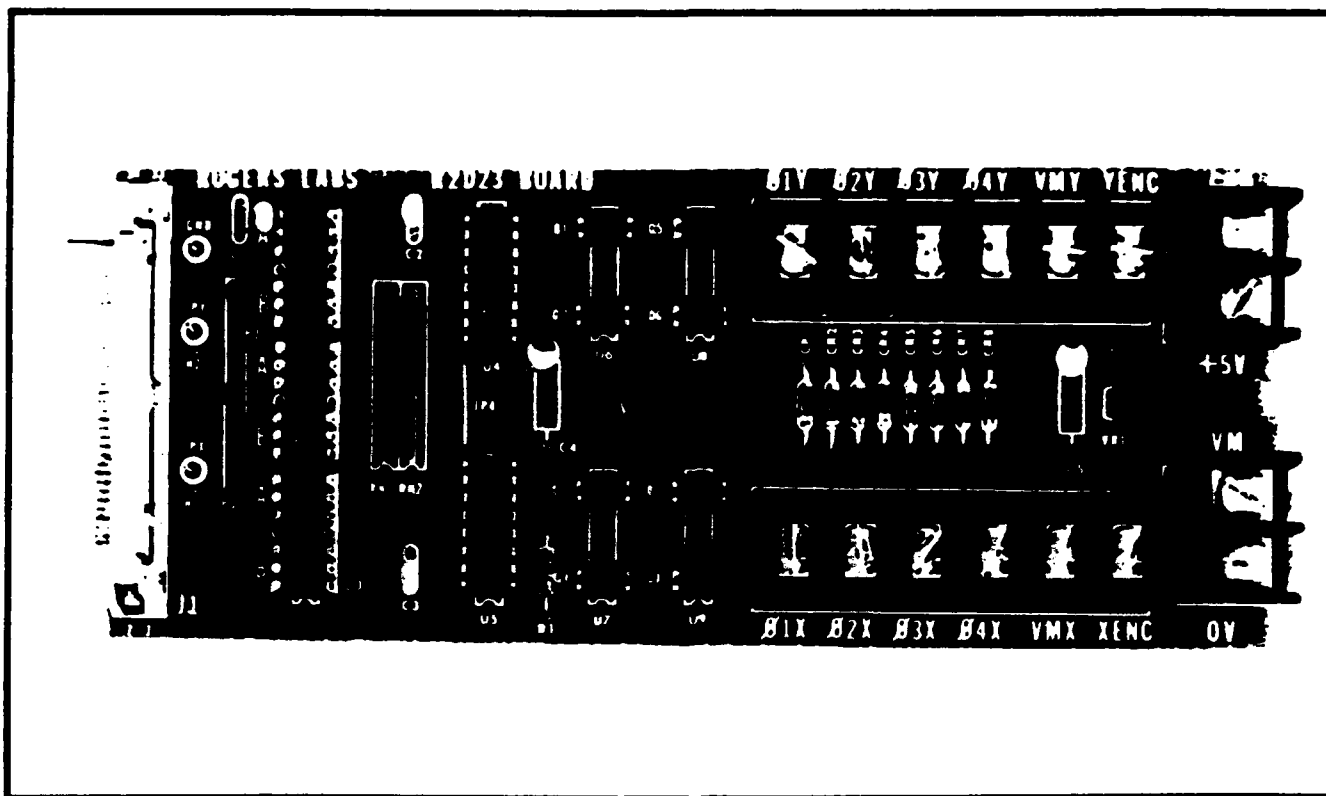
DUAL AXIS STEPPER MOTOR DRIVER BOARD
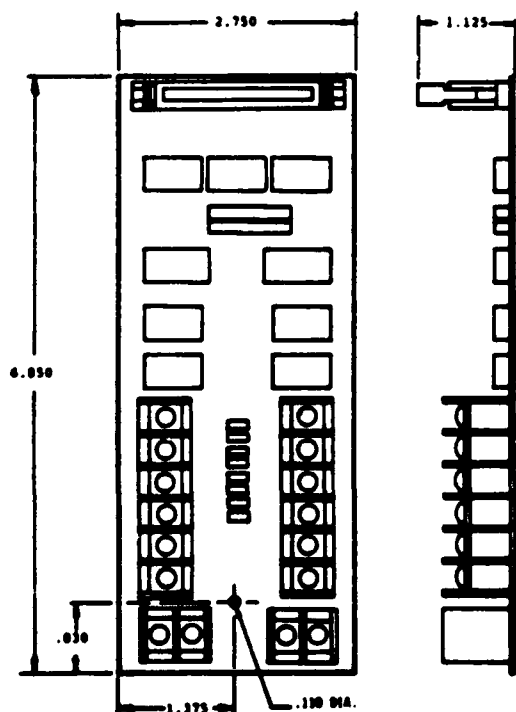
The R2D23 Dual Axis Stepper Motor Driver is capable of driving two 4-phase size 23 stepper motors simultaneously. By incorporating the latest LSI and HEXFET™ technology, the simple circuitry of this board provides up to 1A per phase to both motors.

When used with the A6 T/D Apple II/IIe™ Plug-In Interface Board, the R2D23 provides two axis of computer controlled motion. The clock, mode and direction signals are software generated providing flexible control to many positioning applications including multi-axis robotic controls.

HEXFET is a trademark of International Rectifier Corp.
Apple II/IIe are trademarks of Apple Computer, Inc.

31

ROGERS LABS
2710 SO. CRODDY WAY
SANTA ANA, CA 92704
TEL. (714) 751-0442

R2D23
DUAL AXIS STEPPER
MOTOR DRIVER BOARD
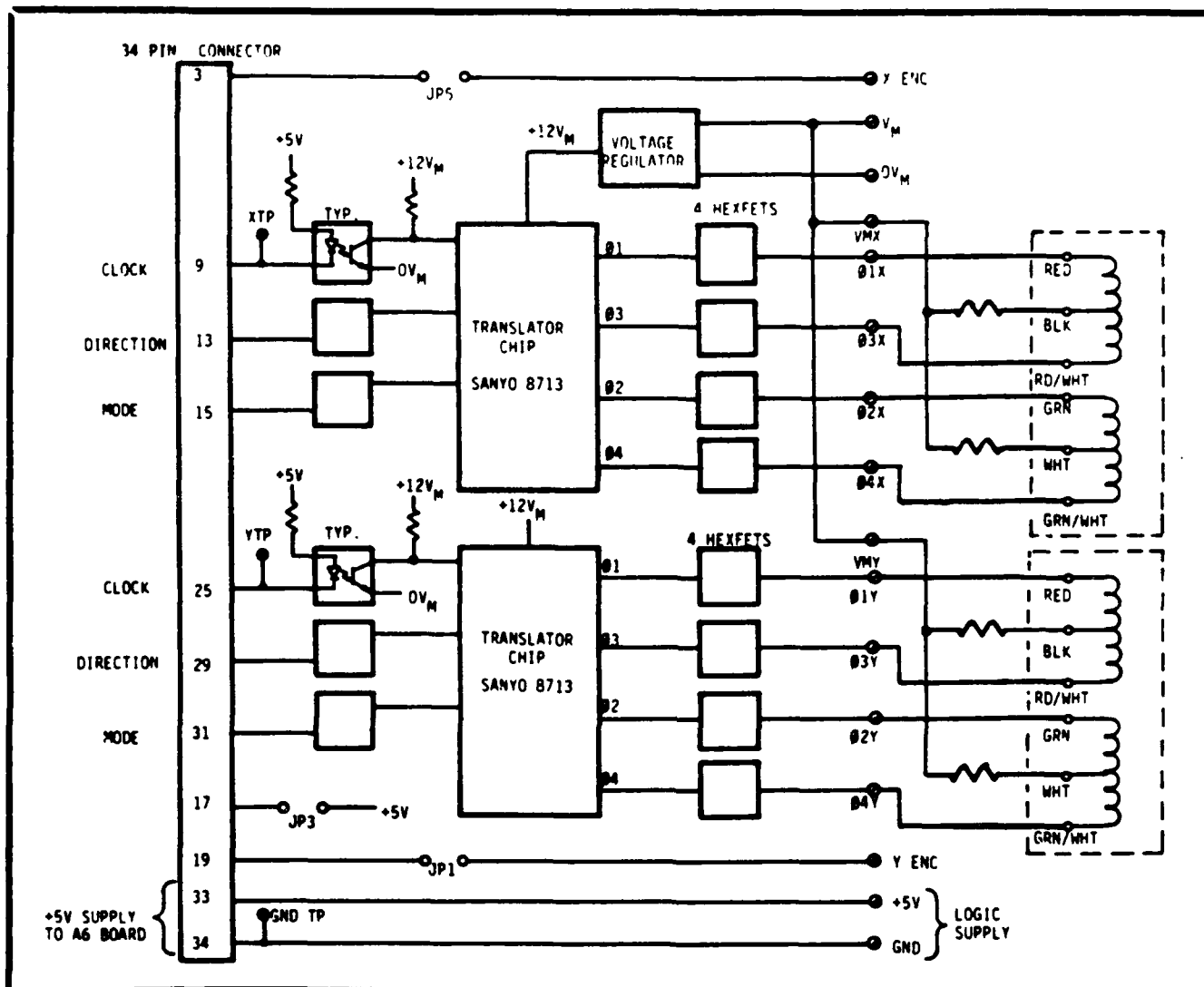
Features:
- Optically isolated input signals for noise immunity
- HEXFET™ output driver transistors diode protected from inductive spikes
- Two input channels for optical encoder feedback
- Industrial barrier strip terminals for wiring

INPUT: Open collector TTL compatible
- Clock frequency: 2 KHZ max (standard); wide band isolators available
- Direction and mode: level controlled

Outputs: High efficiency HEXFET™ driver transistors
- 1 amp continuous rating, 4 amps peak @ 25 C
- 100 Vds device specification with substantial margin
- Completely diode protected against forward and reverse inductive spikes

Power Supply: External power supply required
- 9 to 30 Vdc filtered and unregulated
- On board regulator for stepper motor Universal Controller™ chip

Dimensions: 2¾" x 6⅞"
- Designed for easy mounting on plastic "Snaptrack"™ channel

HEXFET is a trademark of International Rectifier Inc.
Snaptrack is a trademark of Reed Devices Inc.
Universal Controller is a trademark of Sanyo

32

PERSONAL COMPUTER PLUG COMPATIBLE INTERFACE BOARDS

IBM PC BOARDS	DESCRIPTION	LIST PRICE
1432 I/O (PC Motion)	4 AXIS STEPPER DRIVER INTERFACE WITH 32 I/O configurable in sets of (8). 2 channels pulse inputs	$495.00
	HELIX IBM BUBBLE DISK™ 128K	$750.00

PACKAGED SYSTEMS

PCM223	2 AXIS PCMOVER PACKAGE for IBM PC/XT, (SIZE 23)	792.00
PCM423	4 AXIS PCMOVER PACKAGE NON RAMP for IBM PC/XT (SIZE 23)	1,129.00
PCM234	2 AXIS PCMOVER PACKAGE for IBM PC/XT (SIZE 34)	997.00
PCM223P	PCM223 PLUS PACKAGE for IBM PC/XT W/ P. SUPPLY	942.00
PCM423P	PCM423 PLUS PACKAGE NON RAMP for IBM PC/XT W/ P. SUPPLY	1,092.00

Above PCM packages include PCMotion board. motors w/R2 power supply (open frame 12V/2A). drivers. cables & SOFTWARE. (32 I/O INCLUDED).

EXTERNAL INTERFACE BOARDS

R2D34	DUAL AXIS 4 PHASE STEPPER MOTOR DRIVER BOARD for 2 size 34 motors, 3A per phase	282.00
R2D23	DUAL AXIS 4 PHASE STEPPER MOTOR DRIVE BOARD for 2 size 23 motors, 1A per phase	177.00
R1D/A	SINGLE AXIS DC SERVO CONTROLLER INTERFACE BOARD ±10V output, accepts encoder 2 phase pulse input	265.00
RSS8	SOLID STATE RELAY MOUNTING RACK 8 position expandable to 16 by ribbon cable connection to 2nd unit	48.00
R16I T/B	16 CHANNEL OPTOISOLATED INTERFACE TERMINAL BOARD configurable as Input or Output	110.00

STEPPER MOTORS

PH265-02	ORIENTAL Motor size 23 (4) phase stepper motor	59.00
PH299-01	ORIENTAL Motor size 34 (4) phase stepper motor	110.00

ACCESSORIES

R4 T/B	4 MOTOR INTERCONNECT BOARD. for connecting two R2 series drivers to A6 T/D or 1423 I/O for 4 motor operation	40.00
R14 T/B	14 TERMINAL RIBBON CABLE TERMINATION BOARD used to interface A6 T/D with pulse/direction translators opto isolated. accepts encoder input w/line receiver	62.00
R16 T/B	16 CHANNEL RIBBON CABLE TERMINATION BOARD used with A16 I/O or A32 I/O wiring to external devices with common ground connection	37.00
R16S T/B	16 CHANNEL RIBBON CABLE TERMINATION BOARD used with A16 I/O or A32 I/O wiring to external devices with common source connection	37.00
50/34P C/A	CABLE ASSEMBLY for A32 I/O to R16 T/B	19.00
34/34P C/A	CABLE ASSEMBLY for A6 T/D or 1432 I/O to R2D23/34 also used for 1432 to R16 T/B or R16I T/B	17.00
34/16P C/A	CABLE ASSEMBLY for A6 T/D to R14 T/B	17.00
34/D16P C/A	CABLE ASSEMBLY for A6 T/D to (two) R14 T/B	19.00
50/50P C/A	CABLE ASSEMBLY for A32/16 I/O to RSS8	19.00
34/50P C/A	CABLE ASSEMBLY for A16A I/O & 1432 to RSS8	19.00
34C/50P C/A	CABLE ASSEMBLY for cascade connection of two RSS8, 12" long	17.00

Above cables 3 feet long. add $3.00 per foot for extra length

EDWARD R. BYERS CO.

THE BYERS 5B GERMAN EQUATORIAL MOUNTING

BYERS 58 SIDEREAL RATE WORM GEAR DRIVE SYSTEM (Patent Pending):
A research quality BYERS driving system has been specifically developed for the
BYERS 58. Proprietary techniques and a revolutionary design breakthrough make
the BYERS 58 worm gear drive the most accurate tracking system for its size ever
offered by the Edward R. Byers Co. The unique configuration of the new sidereal
drive delivers tracking accuracy equivalent to that of a standard BYERS 9.3 inch drive.
The BYERS drive eliminates most guiding, and makes astrophotography an effortless
pleasure.

PRECISION AZIMUTH ADJUSTMENT:
The portable pier base incorporates an azimuth fine control to facilitate polar alignment
of the equatorial head.

PRECISION ALTITUDE SETTING:
Twin control knobs allow exact adjustment of the inclination of the polar axis.

INSTRUMENT CLASS.
3 INCH DIAMETER BALL BEARINGS:
The BYERS 58 design provides massive 3 inch diameter ball
bearings on both axes.

MANUAL SLOW MOTION RIGHT ASCENSION
AND DECLINATION CONTROLS:
Manual slow motion R.A. and declination controls operate
independently to override the tracking motor and optional
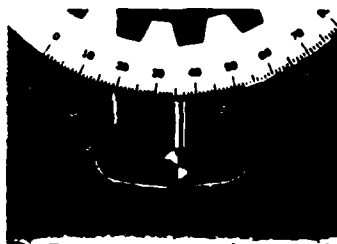declination motor.
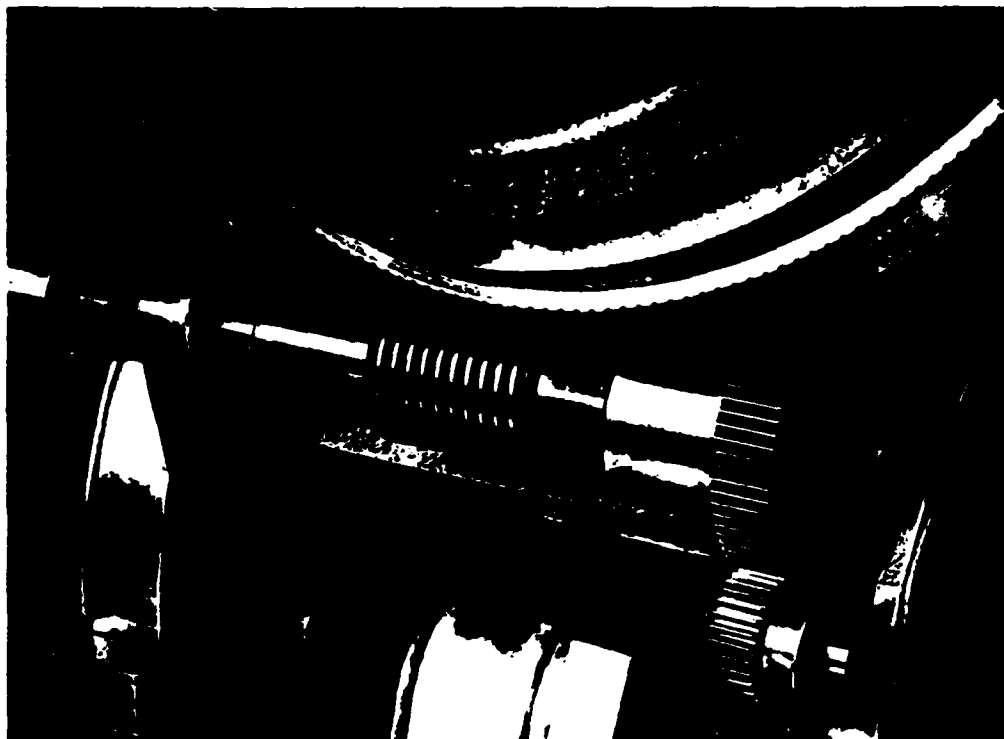
WORM GEAR
DRIVE SYSTEM

POLAR AXIS INCLINOMETER:
A pendulum operates as an inclinometer for adjustment of the polar axis. Since the inclina-
tion of the polar axis must correspond to the geographic latitude of the observing site, it is
possible to 'dial in' the latitude (e.g. polar axis inclination) by turning the control knob and
watching the motion of the latitude scale on the side of the mounting. The pendulum pointer
is quickly calibrated and no leveling of the equatorial head is necessary. In preparation for
long-exposure, deep sky photography, this feature substantially reduces the time required
for polar alignment.

ENGRAVED ALUMINUM SETTING CIRCLES
WITH VERNIER POINTERS:
These setting circles are the finest and most accurate available.
Declination and right ascension circles are indexed and engraved
on the BYERS master dividing engine. Unlike setting circles
provided on other German equatorial mountings, the R.A. circle
on the BYERS 58 is driven in tandem with the pointer and is a
true Porter slip-ring, always displaying the R.A. coordinate of any
object centered in the field of view. It is unnecessary to reset the circle or pointer when
moving from one celestial object to the next. Typical German equatorial mountings lack
this important feature.

POLAR
AXIS
INCLINOMETER

STAINLESS STEEL DECLINATION COUNTERWEIGHT SHAFT:
The stainless steel counterweight shaft is threaded along its length to permit correct
balancing of payloads during tracking. To ensure portability, it is removable from the
declination housing.

POLAR ALIGNMENT TELESCOPE (optional):
A polar alignment telescope with offset illuminated reticle fits
inside the polar axis.

PORTABLE PIER BASE (optional):
An extremely rigid and well designed portable pier base.
which attaches to the azimuth plate of the equatorial head, is
available in varying heights to accommodate Newtonians,
Cassegrains, astrographs, and refractors. Each pier leg wraps
around the vertical post and extends upward to maximize
stability.

MOTORIZED DECLINATION DRIVE (optional):
The standard manual worm gear declination drive may also
be motorized. This option includes a heavy duty motor with
precision clock reduction gears for driving the declination
worm. This motor utilizes dynamic braking and will not coast
or overshoot.

BYERS ELECTRONIC TRACKING CONTROL (optional):
A dual-axis ultra-stable electronic frequency control with
integrated DC power supply is available for critical photographic
applications and battery operation at remote observing sites.
A highly sensitive calibrated adjustment enables effective
compensation for atmospheric refraction. A pushbutton hand
paddle is provided with the unit.

35

THE BYERS 58 GERMAN EQUATORIAL MOUNTING

Edward R. Byers, a master craftsman with an international reputation, combines a specialized background in mechanical engineering, machine design, and metallurgy with over thirty years experience in the design and manufacture of precision astronomical driving systems.

For the scientific community, the Edward R. Byers Co. has continued to provide research level components to such institutions as NASA, Kitt Peak, Jet Propulsion Laboratory, M.I.T. Lincoln Laboratories, and the U.S. National Bureau of Standards. Among professionals and amateurs alike, BYERS drives have achieved legendary status for their phenomenal tracking accuracy.

The BYERS 58 has been developed in response to the demand for a compact, portable equatorial mounting which is both professional in quality and compatible with the astronomical instruments of serious amateurs. Not only does the BYERS 58 meet all necessary criteria for precision and rigidity, it is truly human-engineered for maximum convenience and versatility and offers features unavailable on other telescope mountings.

Sophisticated mechanical stress analyses have resulted in a superior design which incorporates instrument class ball bearings, aircraft-grade heat-treated aluminum castings, and other components of the highest standard.
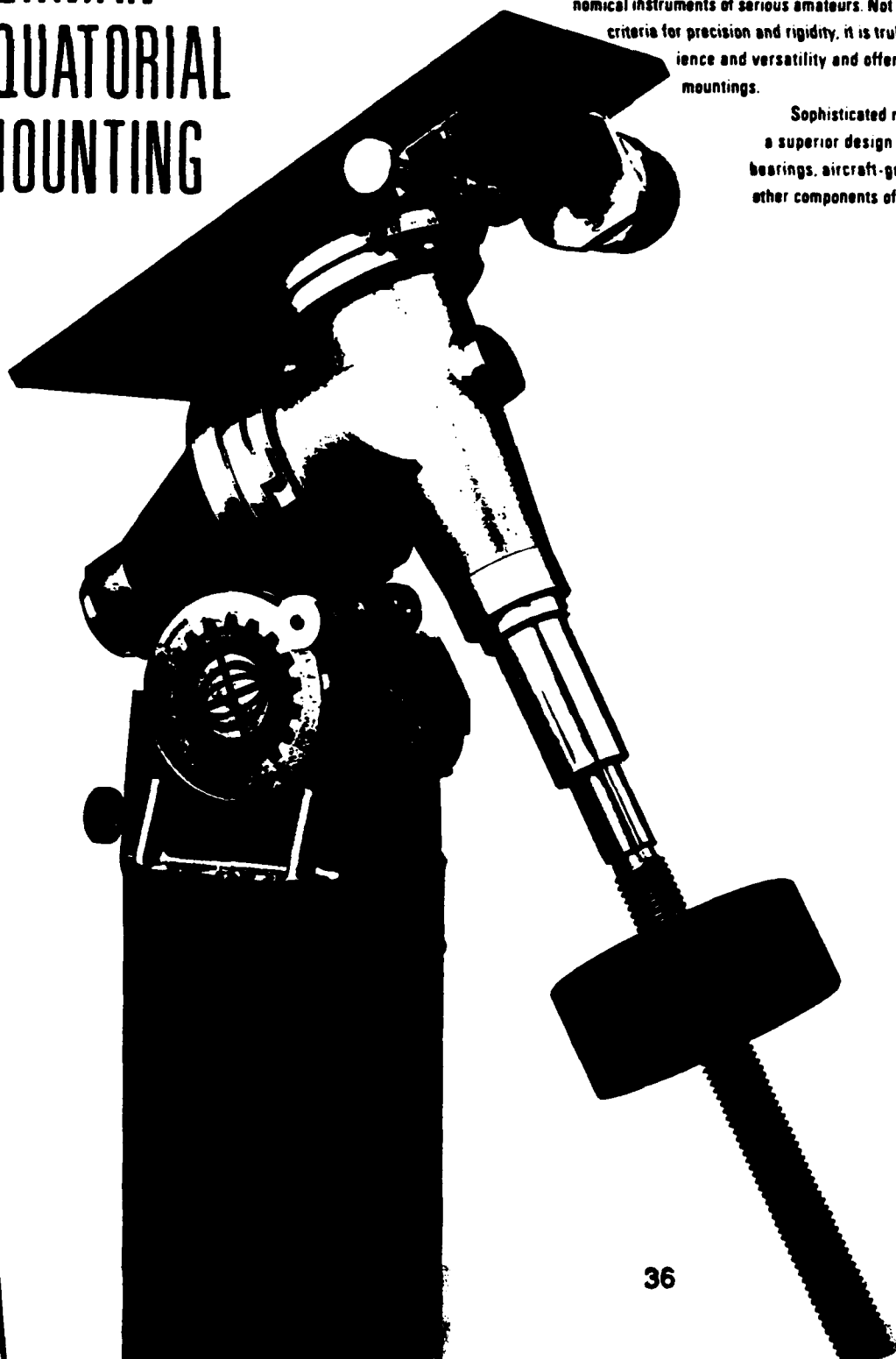
THE ADVANTAGES OF A BYERS MOUNTING
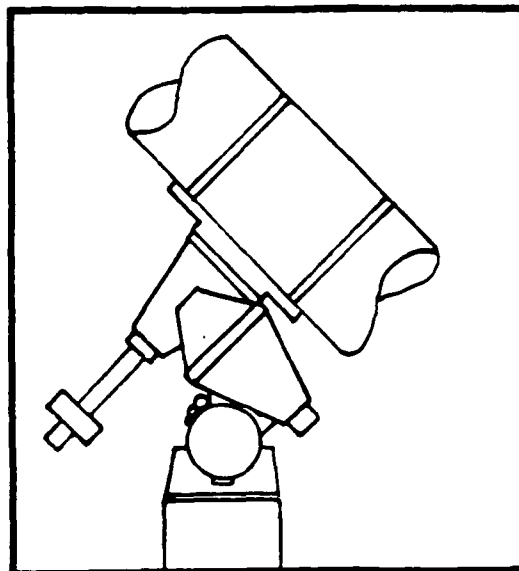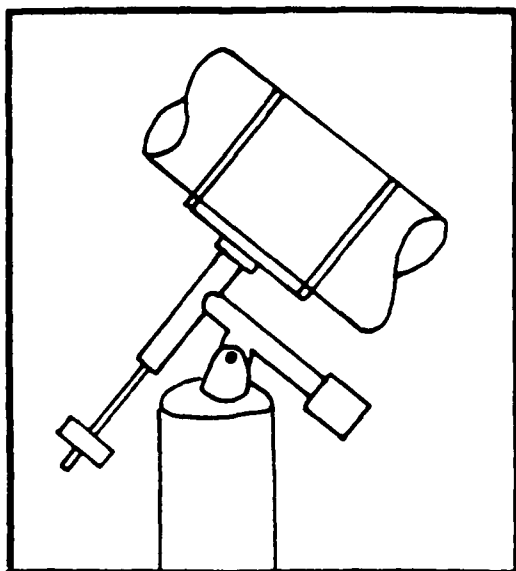
MECHANICAL DESIGN

BYERS mountings are superbly engineered and efficiently designed to maximize stability and rigidity.

The drawing on the left illustrates the common German equatorial mounting available to amateurs. Although the design is simple and inexpensive to manufacture, it represents a flagrant violation of sound principles of mechanical engineering, ignoring virtually all of Russell Porter's recommendations for mounting construction.**

The intersection of the declination axis with the optical tube is the 'Achilles Heel' of most German equatorial mountings. Note the small cross-sectional area at this point in contrast to that of the BYERS mounting on the right. Compare the small shafts and bearings with the oversize shafts, bearings, and huge thrust bearing surfaces of the BYERS design.

TRACKING ACCURACY

BYERS drives have achieved legendary status for phenomenal tracking accuracy. Worm-gear components such as those supplied to the telescope industry by commercial gear manufacturers, while adequate for power transfer applications, are rarely satisfactory for serious research and long-exposure astrophotography.

Highly accurate worm-gear drives for astronomical use cannot be mass produced in the ordinary sense. To meet the demanding requirements of astronomy professionals, all BYERS drives are manufactured to the very highest standards at our own facility, utilizing proprietary techniques and specialized machinery developed by Edward R. Byers.

**Porter, Russell W., "Fundamentals in the Design of Telescope Mountings," in Amateur Telescope Making. Albert G. Ingalls, ed. (NY: Scientific American Press, 1974.) Book 1, page 131. (Originally published 1935.)

BYERS 58 Technical Data

Approximate weights of components:

Equatorial head without counterweight shaft: 25 lbs.
Counterweight shaft: 5 lbs.
Portable pier post: 18 lbs. (for 2' height).
Pier legs: 2.3 lbs. each.
Counterweights: 9.5 lb. provided standard.
                16 lb. optional.
Total weight of BYERS 58 with portable pier: 55 lbs. (not including
      counterweights).

Dimensions:

Distance from pier cap to intersection of polar and declination axes:
      approximately 9" (will vary with geographical latitude).
Diameter of steel pier and base of equatorial head: 6".
Pier height: 2' (recommended for 8"-10" Newtonians).
              Optional pier heights: 2½', 3', 3½', and 4'
              (3' recommended for Celestron 8 and Celestron 11).
Pier leg: 15" length, 11" height.
Tracking platform: 11.85" length, 5.85" width.
Diameter of polar axis through north bearing: 3".
Diameter of declination axis through upper bearing: 3.25".

R.A. and declination drive motors: Heavy-duty, AC synchronous, 3 watts,
      150 in.oz. torque.

Maximum recommended payload for tracking platform: 50 lbs. (Newtonians
      up to 10" aperture and Cassegrains up to 11").

Approximate shipping weight: 75-95 lbs. depending on counterweights provided.

Guideline for selecting counterweights: Payload may be balanced about polar
      axis with counterweights equal to 70% to 100% of payload, depending
      upon location of weights on the counterweight shaft.

BYERS 58 Price List & Ordering Information

BYERS 58 German Equatorial Mounting (portable pier not included)..................$985.00
Portable Pier Base: 2'...275.00
                   2½'...285.00
                   3'...295.00
                   3½'...305.00
                   4'...315.00
Motorized Declination Drive (retro-fitting not recommended) includes clock
      reduction gears and slip clutch assembly......................................145.00
Polar Alignment Telescope with Illuminated Offset Reticle......................... 90.00
BYERS Electronic Tracking Control...315.00
Substitution of 16 lb. counterweight for standard 9.5 lb. counterweight........... 15.00
Each additional 9.5 lb. counterweight... 30.00
Each additional 16 lb. counterweight... 45.00

Cradle Rings for Celestron 8 and Celestron 11......................price to be announced
      (Specify on order form but do not send payment for C8 or C11 rings until notified
      prior to shipment. Rings will be nominally priced.)

Packing Charge... 20.00

California residents add 6% sales tax (Los Angeles County: 6½%).
All prices are F.O.B. our plant, Barstow, California

38

Stepping Motor Basics

Construction and Operation

Hurst permanent magnet stepping motors belong to the class of stepping motors frequently identified as "can-stack" stepping motors with step angles typically in the range of 7.5 to 20 degrees. The motors contain two stacked sets of toothed stator poles and circular coils and a permanent magnet rotor with radial alternating north and south poles as shown in figure 1. The number of rotor poles is equal to the number of stator teeth in each set of poles. The stator pole sets are offset by 1/4 of the pole pitch. With both stator coils energized, the rotor will align itself between the two equal stator fields.

A single step of the rotor is the result of a change of magnetic polarity of one set of stator teeth. This change in polarity is brought about by reversing the direction of current flow in the coil associated with those teeth. The rotor motion for a single step with a load applied is that of a damped oscillation as shown in figure 2. The damping characteristics of this curve may be modified by frictional and inertial loading, the sequence in which windings are energized, and the electronic damping in the drive circuitry.
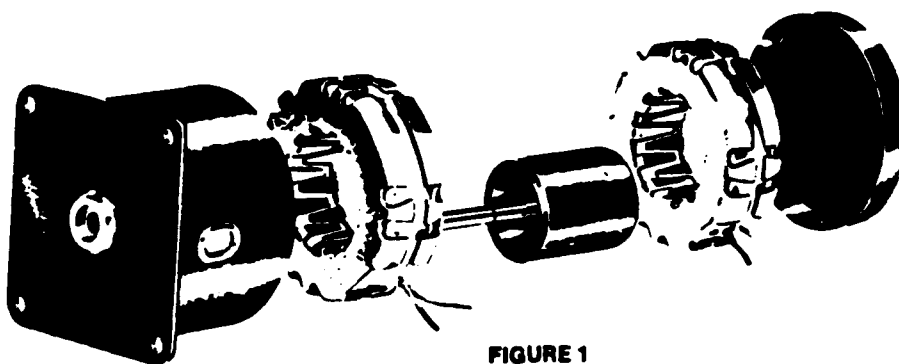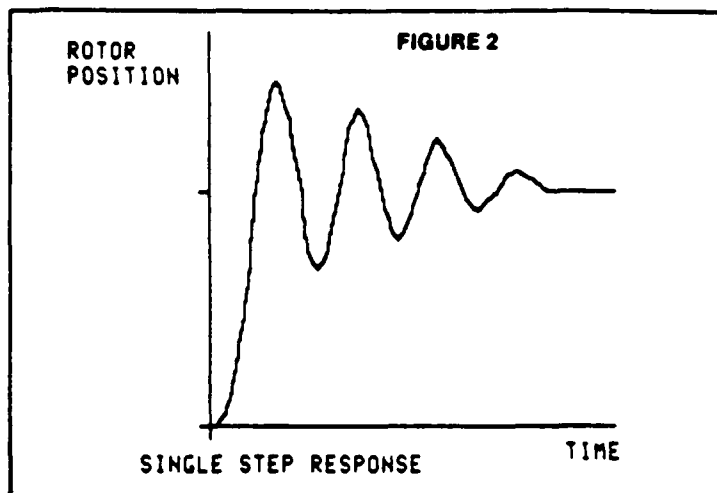

FIGURE 2

ROTOR POSITION

SINGLE STEP RESPONSE   TIME

FIGURE 1

Stepping Sequences

For continuous rotation a repeating sequence of changing tooth polarity is required. Differences in rotor performance characteristics result from different types of sequences.

The most commonly used scheme for stepping the rotor is to energize both stator coils and to reverse the current in alternate coils with each successive step. This results in a four step sequence as shown in figure 3. Reversing the sequence reverses the direction of rotation. This is called a full step mode with two phases on.

It is also possible to step the rotor with the same angular increment by energizing only one phase each step as shown in figure 4. This is also a four step sequence and is commonly known as a wave drive. Since only half the copper volume is being used, the efficiency is lower and there is less damping with this sequence than with two phases on.

A third sequence alternates between one and two phases energized to produce 1/2 the step angle of the previous sequences. The half step sequence shown in figure 5 requires eight steps. Although angular resolution may be improved with half-stepping, an important characteristic to note is the lower torque on alternate steps when only one phase is energized. The smaller step angle does provide an improvement in damping, and half-stepping may be advantageous in applications which require operation of the motor at or near resonant frequencies.

FIGURE 3. Full Step, 2 Phases On Sequence

FIGURE 4. Wave Drive Sequence

FIGURE 5. Half-Step Sequence

39
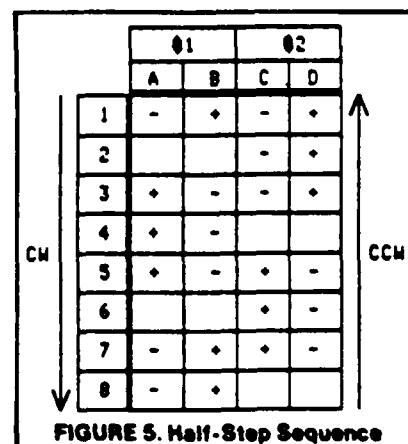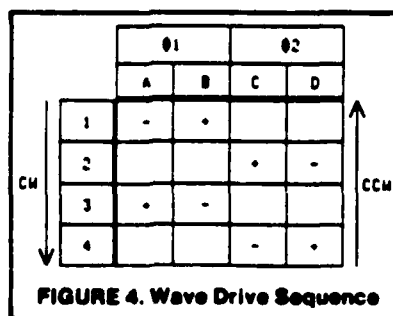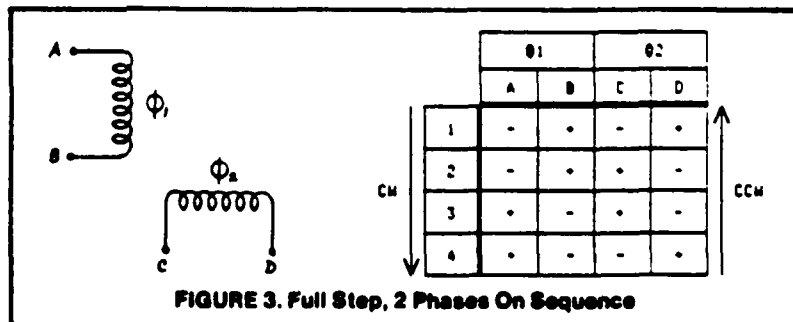
Torque Characteristics

The maximum torque developed by the motor is the static or holding torque. It is measured while displacing the rotor one step with two phases energized (full step mode). The torque developed during continuous stepping decreases with increasing stepping rate since the current rise time when a phase is energized is limited by the inductance to resistance ratio of that coil.

A typical dynamic torque curve is shown in figure 6. The lower curve represents the maximum torque load which the motor will start and stop without losing steps. The upper curve represents the maximum torque which the motor can develop at a given pulse rate or alternately, the maximum rate to which a given load can be accelerated.

The curve of figure 6 is obtained while operating the motor at a constant voltage over the entire range of pulse rates. Thus the input power to the motor is substantially decreased at higher pulse rates. The torque can be increased at higher pulse rates by increasing the input using a variety of drive techniques. These include simple schemes such as increasing the voltage directly or decreasing the time constant by adding external series resistance, and more elaborate techniques such as bi-level voltage drives or chopper type drives which sense the winding current.

When overdriving techniques are used to increase motor performance, consideration must be given to the maximum permissible temperature rise of the motor windings based on the insulation rating of the motor.

Bifilar and Bipolar Operation

The terms bifilar and bipolar refer to two different types of coil windings that may be used in the stator coils. Bipolar windings contain a single coil in each stator half. The switching circuitry used to reverse the direction of current flow with this coil is typically of the full bridge or dual supply type (figure 7). Bifilar windings contain two windings in each stator half. When they are connected as shown in figure 8, the magnetic field may be reversed by switching from one winding to the other. Note that although a bifilar-wound motor does contain four coils or "phases", it is operated as a two phase motor.

The bifilar-wound PM steppers are widely used because of the drive circuit simplicity. However, there are performance differences between the two types of windings. Since the winding volume per phase of a bifilar-wound stepper is only half that of a bipolar-wound stepper, the attainable ampere-turns for a given input power will necessarily be lower for the bifilar-wound motor. As expected the torque is therefore lower. However, it is only lower in a holding mode or at low stepping rates. The reason is that the bipolar coil with its larger volume will also have a larger time constant (L/R) and at higher stepping rates the bipolar-wound motor's torque will decrease to approximately the same level as that of the bifilar-wound motor.

The choice of winding type will depend upon the application. The holding torque for a bipolar version of a given motor will be 20-30% higher than the bifilar version and the dynamic torque will be higher at low stepping rates. Difference in dynamic performance will be small at higher stepping rates. These performance differences must then be weighed against the drive circuit complexity.

Resonance

All stepping motors exhibit resonance at certain pulse rates. typical can-stack type stepper applications the most common encountered resonances occur at lower frequencies (less tha 100 pulses per second). Although there is no loss of steps at thes frequencies, there is an increase in vibration and noise. This be comes even more noticeable when a gear train is coupled to tr motor. When operation at resonant frequencies cannot be avoide some improvement may be made by such methods as increase frictional damping, reduced input power, modified drive circuitry c half-stepping.

Step Angle Accuracy

The average value of the measured step angles of an unloaded stepping motor over 360 degrees will be equal to the nominal step angle. The maximum deviation of the individual steps from the nominal step angle is the error usually specified as a non-cumulative or incremental step angle error.
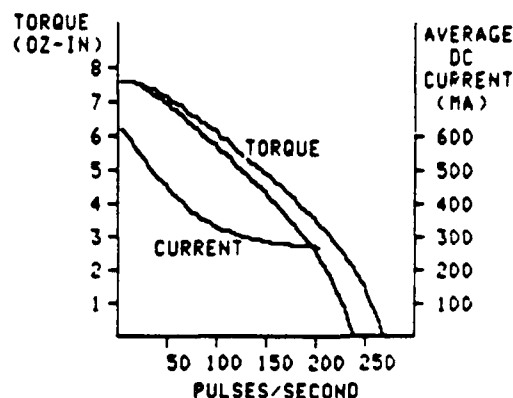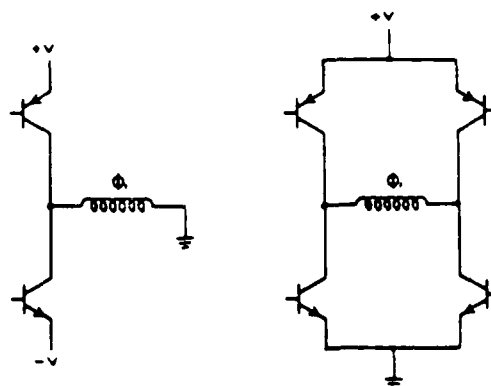

FIGURE 6. Dynamic Torque

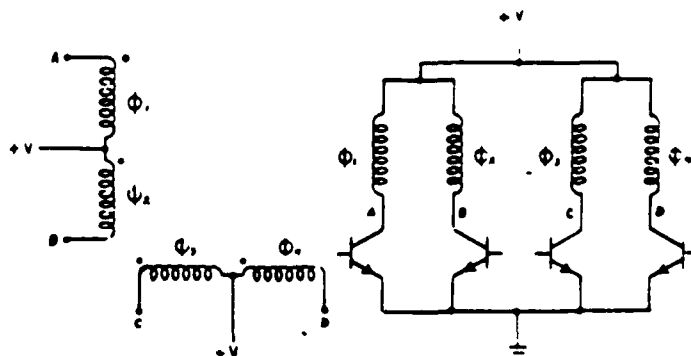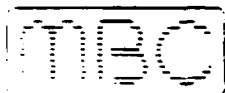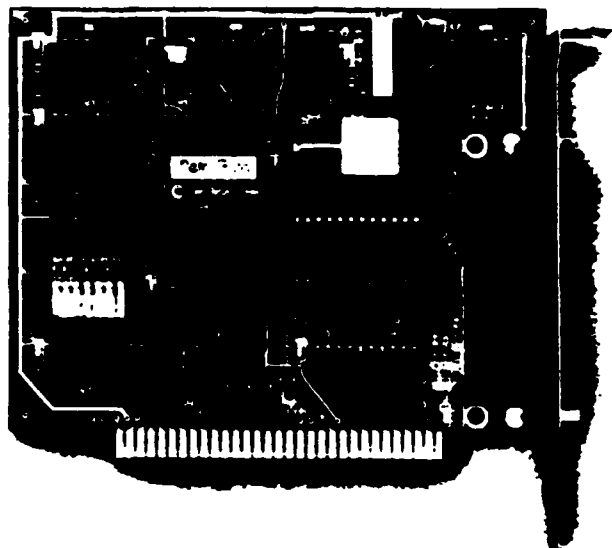FIGURE 7. Dual Supply and Full Bridge Drivers

FIGURE 8. Bifilar Windings

8 CHANNEL HIGH SPEED A/D CONVERTER AND TIMER COUNTER INTERFACE MODEL DASH-8

DATA ACQUISITION AND CONTROL FOR IBM PC/XT/AT AND COMPATIBLE COMPUTERS

FEATURES

- 8 A/D Channels with 12 Bit Resolution
- 4000 Samples/Sec. A/D Throughput with Supplied Software
- Hardware Supports 30.000 Samples/Sec. in Assembly Language
- Programmable Scan Rate
- Foreground/Background Operation
- 7 Bits of Digital I/O (4 Outputs. 3 Inputs)
- Interrupt Handling
- Event. Period. Pulse Width. and Frequency Counting
- SOFTWARE INCLUDED (Graphics. Calibration. Linearization. Installation. I/O Driver)
- Precision 10 Volt Reference Output
- +/−12 and +5 Volt Power from IBM PC/XT
- Accessories-Screw Terminal and Expansion to 128 Channels
- Outputs frequency from 37 Hz to 1 MHz

APPLICATIONS

- Data Logging
- Process Control
- Signal Analysis
- Robotics
- Energy Management
- Product Testing
- Chromatography

FUNCTIONAL DESCRIPTION

MetraByte's DASH-8 is an 8 channel 12 bit high speed A/D converter and timer/counter board for the IBM PC. The DASH-8 board is 5" long and can be fitted in a "half" slot. All connections are made through a standard 37 pin D male connector that projects through the rear of the computer. The following functions are implemented on the DASH-8.

An 8 channel. 12 bit successive approximation A/D converter with sample/hold. The full scale input of each channel is +/−5 volts with a resolution of 0.00244 volts (2.44 millivolts). Inputs are single ended with a common ground and can withstand a continuous overload of +/−30 volts and brief transients of several hundred volts. All inputs are fail safe i.e. open circuit when the computer power is off. A/D conversion time is typically 25 microseconds (35 microseconds max.) and using the supplied software driver. throughputs of up to 4000 samples/sec are attainable operating under BASIC.

An 8253 programmable counter timer provides periodic interrupts for the A/D converter and can additionally be used for event counting. pulse and waveform generation. frequency. period. and pulse width measurements.

There are three separate 16 bit down counters in the 8253 One of these is connected to a submultiple of the system clock. and all I/O functions of the remaining two are accessible to the user. Input frequencies up to 2.5 Mhz can be handled by the 8253.

7 bits of TTL digital I/O provided are composed of one output port of 4 bits and one input port of 3 bits. Each output will handle 5 standard TTL loads (8mA sink curent).

1 precision +10 00v (+/−0.1v) reference voltage output is derived from the A/D converter reference. This output can source/sink 2mA.

An external interrupt input is provided that is jumper selectable for any of the IBM P.C. interrupt levels 2-7 and allows interrupt routines to provide background data acquisition or interrupt driven control. The DASH-8 includes status and control registers that make interrupt handshaking a simple procedure. The interrupt input may be externally connected to the timer/counter or any other trigger source.

IBM PC. buss power (+5. +12. −12v) is provided along with all other I/O connections on the rear connector. This makes for simple addition of user designed interfaces. input signal conditioning circuits. expansion multiplexers etc.

BLOCK DIAGRAM
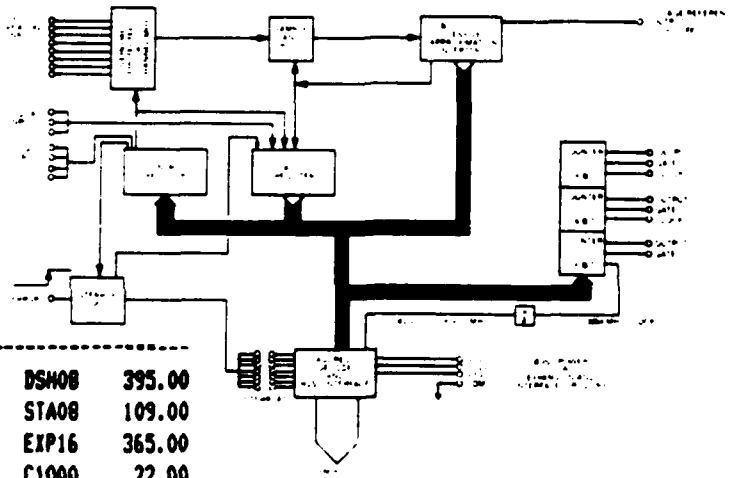
DASH 8 4,000 S/S 8 Ch A/D	DSH08	395.00
Screw Terminal Board , DSH08	STA08	109.00
EXP16 16 Channel Expander Brd	EXP16	365.00
10' Daisy Chain Cable, DSH16	C1000	22.00
DC/DC 5 Volt Power Supply	P6408	42.00
Binary Source Listing, Disk	SLD08	25.00

42

PROGRAMMING

All I/O is accessed via this Call statement:

CALL DASH8 (MD%, DIO%, FLAG%)

There are 18 modes of operation available to the programmer and are represented by the integer variable MD%. The following table lists all its capabilities:

MODE	FUNCTION
0	Initialize. input DASH-8 base address.
1	Set multiplexer channel low and high scan limits
2	Set Multiplexer (channel) address
3	Read Multiplexer (channel) address.
4	Perform a single A/D conversion. Return data and increment multiplexer address.
5	Perform an N Conversion scan after trigger. Scan rate set by Counter 2 or external strobe.
6	Enable interrupt operation.
7	Disable interrupt operation.
8	Perform conversions on N interrupts and dump data in segment S of memory. (Background Operation)
9	Unload data from segment S and transfer to BASIC array variable.
10	Set timer/counter configuration
11	Load timer/counter
12	Read timer/counter.

MODE	FUNCTION
13	Read digital inputs IP1-3.
14	Output to digital outputs OP1-4
15	Measure frequency with timer/counter
16	Measure Pulse Width with timer/counter
17	Tag lower nybble of data with channel number

The integer variable, DIO% represents Input or Output data. FLAG%, the third integer variable contains the error codes. If FLAG% is returned non-zero, then an error has ocurred. There are 13 error codes available to the programmer for easy error diagnosis.

After initializing the DASH-8, the following program illustrates the ease at which 4000 Samples/Sec. can be obtained.

```
xxx10  MD% = 1                              ' set mux scan limits
xxx20  LT%(0) = 2                           ' start scan on channel 2
xxx30  LT%(1) = 5                           ' end scan on channel 5
xxx40  CALL DASH8 ( MD%. LT%(0). FLAG% )    ' setup
xxx50  IF FLAG% < > 0 THEN PRINT "ERROR"    ' checks for errors
xxx60  DIM A% (100)                         ' dimension array of 100
xxx70  MD% = 5                              ' Mode 5
xxx80  TR%(0) = VARPTR (A%(1) )             ' start as element 1
xxx90  TR%(1) = 100                         ' 100 conversions
xx100  CALL DASH8 ( MD%. TR%(0) FLAG% )     ' do conversions  load array
xx110  IF FLAG% < > 0 THEN PRINT "ERROR"    ' checks for errors
```

SOFTWARE

The following utility software is included at no additional expense with the DASH-8. It is contained on a single sided PC-DOS 1.10 format 5-¼" floppy disk (upward compatible with DOS 2.0):

- A machine language I/O driver (DASH-8. BIN) for control of A/D. timer and digital I/O channel functions via BASIC CALL. The I/O driver can select multiplexer channels. set scan limits. perform software command A/D conversions. interrupt driven conversions and scans. set and read the timer counter and measure frequency and pulse width. A source listing is available as an optional item for the assembly language programmer (Model #SLD-08).
- Transducer linearization.
- Initial setup and installation aids.
- Graphics package for display of processed data.
- Examples and demonstration programs.

Using state of the art data conversion components, the DASH-8 has been designed to provide a powerful and inexpensive analog/digital interface on a single half slot board. It is ideally suited to any application requiring high speed 12 bit data acquisition at the lowest possible cost. The freedom from complexity and the I/O mapped control make programming straightforward.

ACCESSORIES

MODEL STA-08
SCREW TERMINAL CONNECTOR BOARD

All I/O is brought out to miniature screw terminal connectors. The digital I/O port lines are monitored by L.E.D.'s and a small breadboard area with +/-12v & +5v power is available for amplifiers, filters and other user circuits. This offers the user, easy access to all I/O lines.

MODEL EXP-16
UNIVERSAL EXPANSION MULTIPLEXER & INSTRUMENTATION AMPLIFIER BOARD

This board multiplexes 16 differential inputs to a single output suitable for connection to one input channel of DASH-8. Up to 8 EXP-16 boards can be cascaded together on a single DASH-8 for a total of 128 channels of analog input. Switch selectable gains of 1, 2, 10, 50, 100, 200, and 1000 are available plus a special user designated gain. Cold Junction Compensation is also supplied on the board for thermocouples and at 0.1 degree per bit resolution.

CONNECTOR PIN ASSIGNMENTS

All analog inputs and digital I/O is through a standard 37 pin D type male connector that projects through the rear panel of the computer. For soldered connections a standard 37 pin D female (ITT/Cannon DC-37S or equivalent) is the correct mating part, and can be ordered from MetraByte as part #SFC37. Insulation displacement (flat cable) connectors are available from Amp (#745242-1), 3M, Winchester, Robinson-Nugent etc.

The connector pin assignments are as follows:
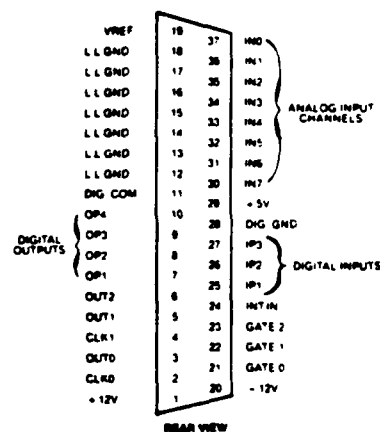
SPECIFICATIONS

POWER CONSUMPTION

+5 v supply:	107 mA Typ. / 80 mA max.
+12 v supply:	6 mA Typ. / 10 mA max.
-12 v supply:	10 mA Typ. / 16 mA max.

8 ANALOG INPUT CHANNELS

Resolution:	12 bits (2.4 mV/bit)
Accuracy:	0.01% of reading +/- 1 bit
Full Scale:	+/-5 volts
Coding:	Offset binary
Overvoltage:	to +/-30 volts
Configuration:	Single ended
Input current:	100 nA max at 25 deg.C.
Temp. Coef.:	Gain or F.S., +/- 25 ppm/deg.C. max. Zero, +/- 10 microvolt/deg.C. max.
A/D Type:	Successive approximation

ENVIRONMENTAL

Operating Temperature Range:	0 to 50 deg. C.
Storage Temperature Range:	-20 to +70 deg. C.
Humidity:	0 to 90% non-condensing
Weight:	4.5 oz. (128 gms.)

5.2 The Silicon Bolometer Operating Manual   (53 pages).

SYSTEM NOTES

The Silicon Bolometer, Unit #1059, has been mounted in a side-looking configuration in conjunction with field mirror optics, aperture slide, filter wheel and extensive cold baffling. The bolometer itself has been mounted within a hemispherical cavity and overcoated with a black absorbing coating. An aperture of 1.05 mm diameter mounted directly over the unit provides the defining area. The system layout within the HD-3 is shown on the enclosed drawing. Details of the key system components are outlined in the following paragraphs:

1) Bolometer:

Material:	Silicon
Area:	1.05 mm x 1.20 mm
Operating Temp.:	1.6°K
Freq. Resp.(70%):	115 Hz
Thermal Cond.(G):	$\sim$ 1 μW/°K
Responsivity (S):	2.2 x 10^6 V/W
N.E.P.: (20 Hz):	2.2 x 10^{-14} W/Hz $^{1/2}$

2) Fabry Mirror:

Shape:	Off-axis Paraboloid @F/24
Original Paraboloid size:	25.40 mm
Radius of curvature:	50.80 mm at the center of the original paraboloid
Focal length of Paraboloid:	25.40 mm
Diameter of off-centered Mirror:	11.40 mm
Off-center distance:	7.00 mm
Field Stop to Mirror:	30 mm (not critical)
Geometrical spot size:	1.06 mm

3) <u>Aperture Slide:</u> The aperture slide is positioned on the rear face of the bolometer substrate and is controlled by a remotely actuated rod located on a dewar face 90° from the vacuum window. The slide features 5 positions with the following location:

     Position 1 (Full In) - Blank

           2 - 2.0 mm dia.

           3 - 3.0 mm dia.

           4 - 5.0 mm dia.

           5 (Full Out) - 10 mm dia.

Operation of the slide should be performed in the following manner:

a) From a full out position, slowly insert the control rod until contact with the internal coupler is made.

b) Rotate the rod until the index arm aligns with the coupler index slot; this will allow positive contact to be established.

c) Move the slide to the desired location. No external index has been provided; however, a simple counting of the ball index positions is easily established.

d) Disengage the control rod and return to the full out position to minimize thermal heat leak.

e) Slide operating tension may be adjusted by means of the "Allen" type socket screw on the slide top.

4) <u>Filter Wheel</u>

CVF STEPPER DRIVE

The remote CVF drive consists of a stepper motor, a tooth-belt reduction, and a control unit. Additionally, a high resolution potentiometer gives absolute rotational position. Power is supplied by the control unit, which contains the stepper translator and logic circuits. Direction, on/off, choice of external or internal control, and single step are all accomplished at the control unit. The driven shaft can be rotated by hand with power on or off, and the potentiometer readout is conveniently available even if the manual modes are chosen.

Several custom modifications are available at no charge, such as non-standard voltage operation, final drive ratios different from standard, etc.

CVF DRIVE NOTES

1. "External Controls" are TTL compatible.
2. Nominal step rate with hand controls is 2 steps/sec.
3. Motor step increment is 7.5°; standard drive reduces this to 1.46°/step at CVF drive output. The following final increments are available on special order.

       1.31°
       1.19°
       1.09°
        .94°
        .82°

4. Resolon Potentiometer readout specifications:

   Electrical travel   - 340°
   Mechanical travel   - Continuous
   Nominal Resistance - 10 K Ohm
   Linearity   -   0.25%   or   51   arc   minutes
   Repeatability   - 0.1% or 22 arc minutes
   Temperature coeff. - -0.03% per °c or 6 arc minutes/°c
   Recommended Readout (Furnished by customer)

       3 1/2 Digit Ohmeter $\Rightarrow$ 3° per least significant digit
       4 1/2 Digit Ohmeter $\Rightarrow$ 18 arc minutes per LSD

5. Control Unit

       Size   - 7" x 5" x 4"
       Weight   - 6 Pounds
       Power Consumption   - 10 W

6. Drive Unit

       Size   - 7" x 5" x 3 1/2"
       Weight   - 3 Pounds
       Output Shaft   - .250" (final drive shaft)

FILTER WHEEL STEPPER DRIVE NOTES

The final drive ratio for the CVF/filter wheel is derived from the following information:

       1. Drive gear = 14 teeth
       2. Driven shaft gear = 128 teeth
       3. Motor step increment = 7.5°

thus, the final increment at the wheel is (128 ÷ 14) x 7.5° = 0.82° per step.

FWD drive causes the wheel to rotate clockwise when viewed from the dewar entrance window. The wheel will advance from maximum wavelength to minimum wavelength in this direction. REV rotation causes the opposite effect.

OPERATION

1. Plug the motor drive into a source of 110 VAC (Nom)/50 or 60 Hz.

2. Select direction of rotation (FWD or REV).

3. Select drive mode; internal or external.

4. Move drive switch to "on" for internal operation & wheel will rotate.

5. Turn drive switch "off" when desired position is reached.

6. Single step switch (pushbutton) may be used in "INT" mode to move drive by one increment only.

7. All external signals are 5V level compatible (1 TTL load each) and are arranged as follows:

> Direction: + 5 = FWD; 0 = REV
> Drive: 0- +5V square wave DC $\leq f \leq$ 200 Hz

8. "Sync" jack is provided as a monitor of the internal oscillator.

9. Potentiometer readout is on pins 1 & 2 of J1 with pin 2 being ground. This is a 0-5 volt readout with the potentiometer "0" position set between two filter positions.

Specification changes for University of Utah system

> Drive Ratio Gives   0.82°/step
>
> Nom. Step Rate = 0.82°
>
> 0 - 5V Output on Readout (10 K ohms impedance)

TO POSITION READOUT

READOUT POTENTIOMETER

CVF DRIVE

STEPPER MOTOR

TRANSLATOR

OSC.

FWD
REV
DRIVE

FWD
REV

HAND CONTROLS

EXTERNAL CONTROLS
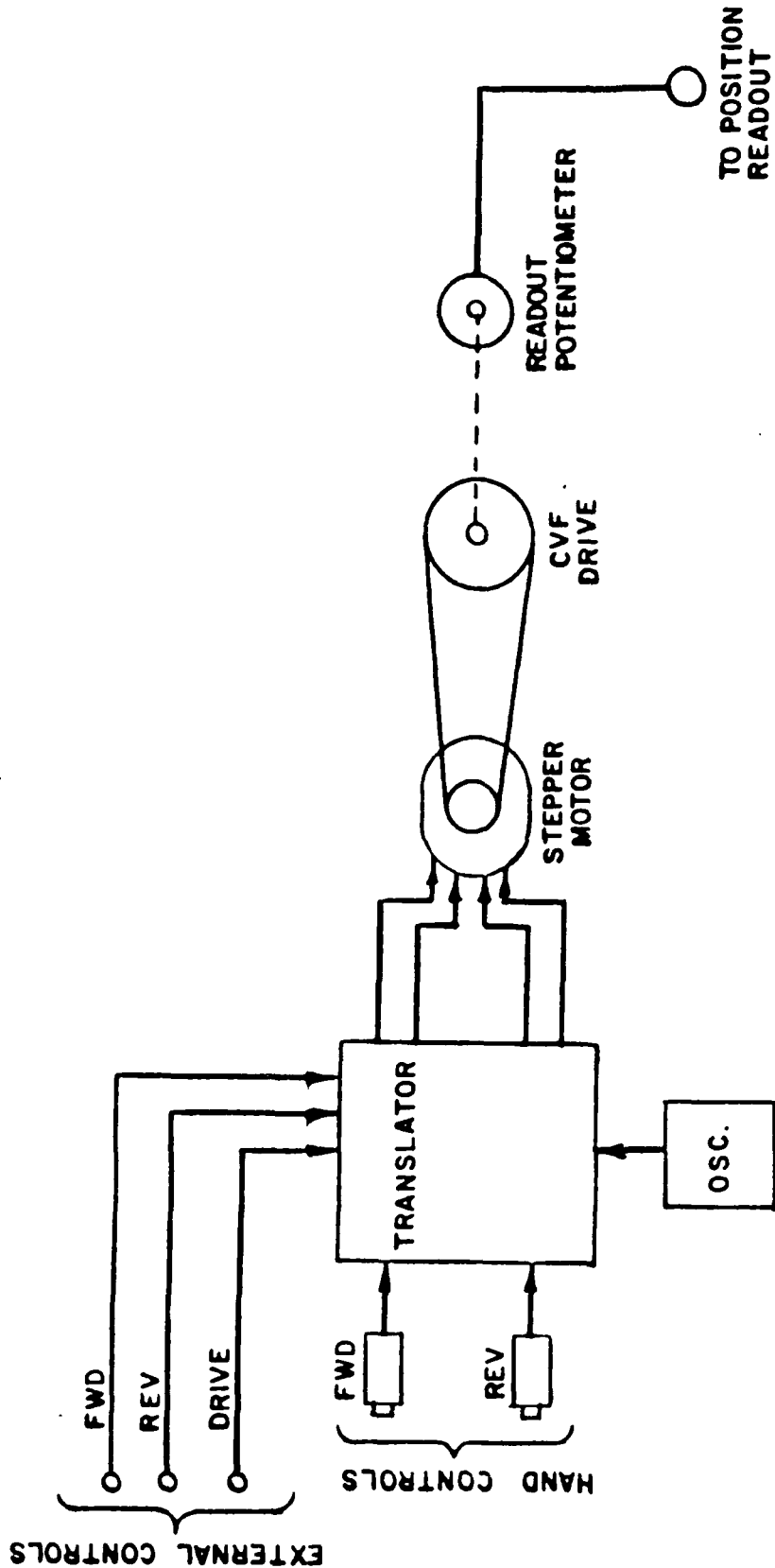
DIGITAL DRIVER
BLOCK DIAGRAM

INFRARED LABORATORIES INC.
1808 EAST 17th STREET
TUCSON, ARIZONA 85719
U.S.A.

MOTOR DRIVE

Direction Input

Step Input

INT. OSC (2H₃)

Motor Drivers

Current Source

Power Supplies

AC Power Input

Stepper Motor

Resolon (Continuous) Pot

Position Readout
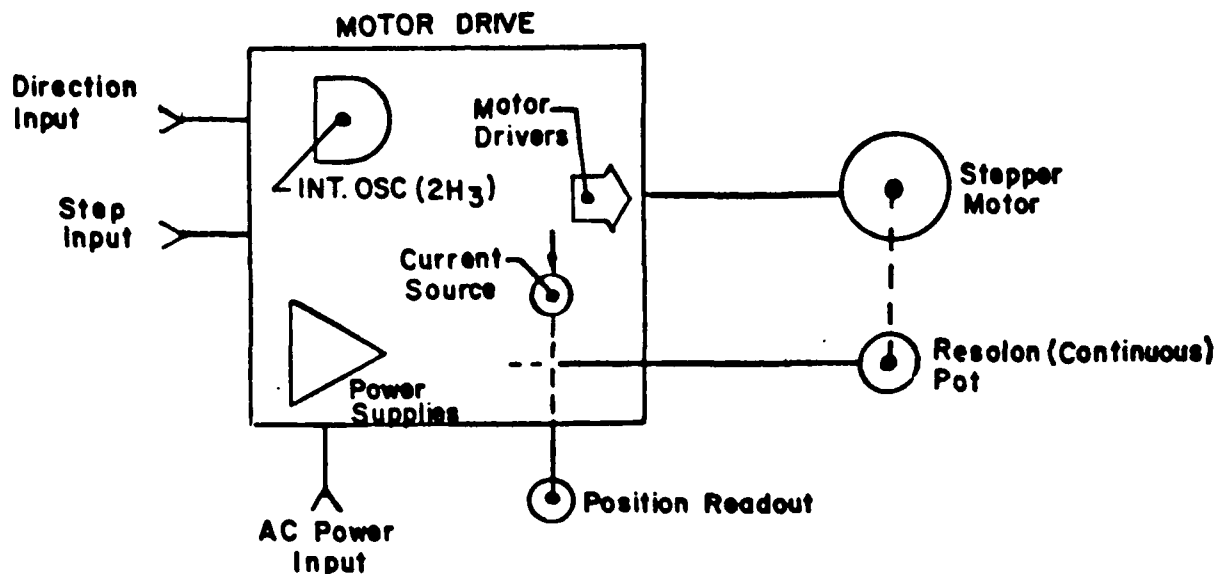
Readout for stepper drive is current-source driven resolon potentiometer. Output to the data system is 0 - 5 volt or 0 - 10 volt (specify desired range). All inputs are TTL compatible. Interface connector is Canon "D" with 9 pins (male panel connector).

DIGITAL DRIVER FUNCTIONAL DIAGRAM	
INFRARED LABORATORIES INC. 1808 EAST 17th STREET TUCSON, ARIZONA 85719 U.S.A.	
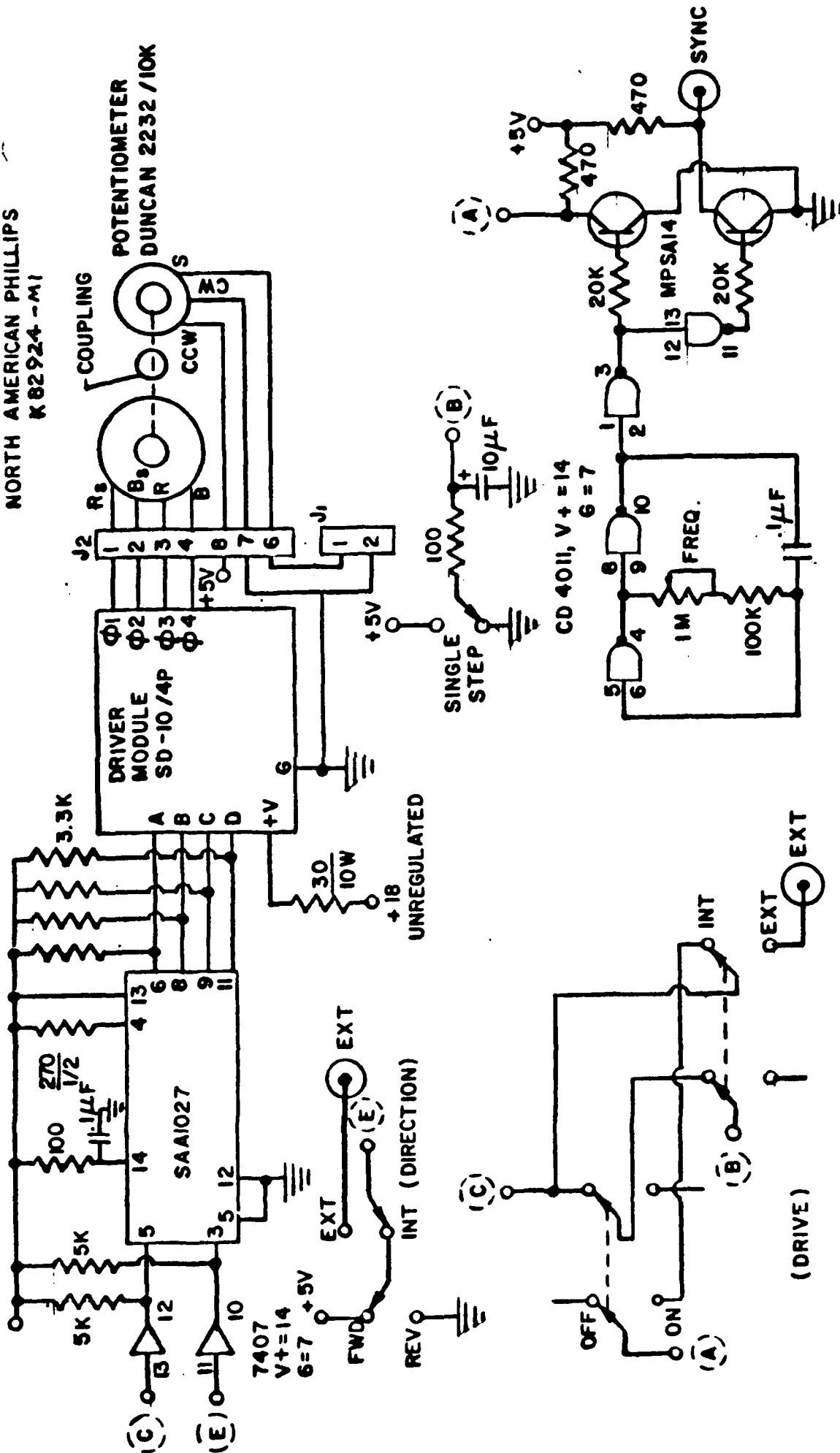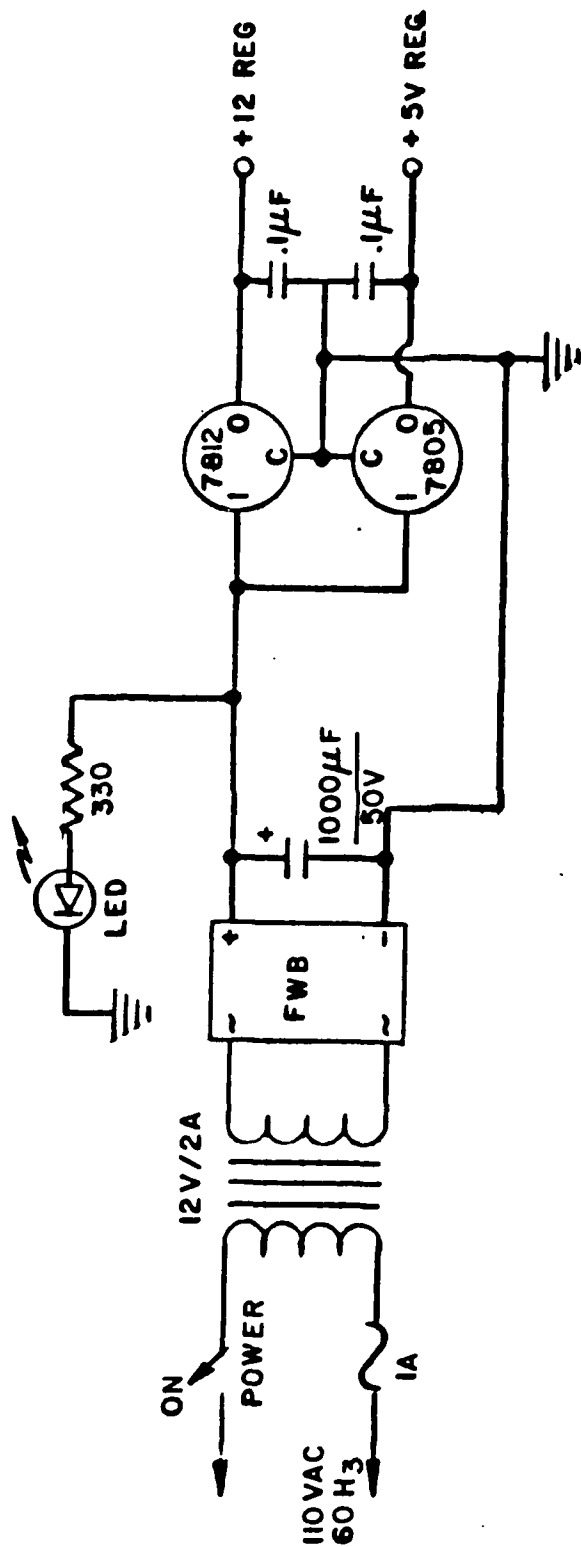
DIGITAL DRIVER
SCHEMATIC DIAGRAM

INFRARED LABORATORIES INC.
1808 EAST 17th STREET
TUCSON, ARIZONA 85719
U.S.A.
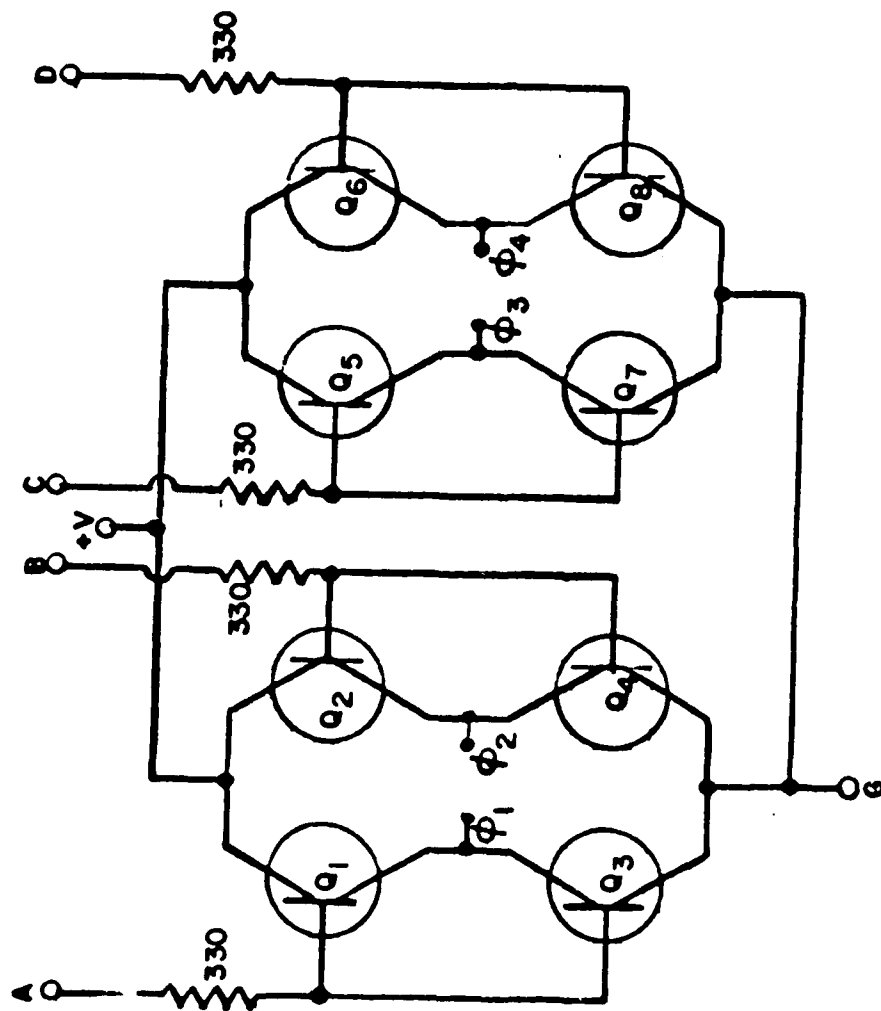
$Q_1 - Q_2 - Q_5 - Q_6 = ECG\ 254$

$Q_3 - Q_4 - Q_7 - Q_8 = ECG\ 258$

DIGITAL DRIVER
DRIVER MODULE

INFRARED LABORATORIES INC.
1808 EAST 17th STREET
TUCSON, ARIZONA 85719
U.S.A.
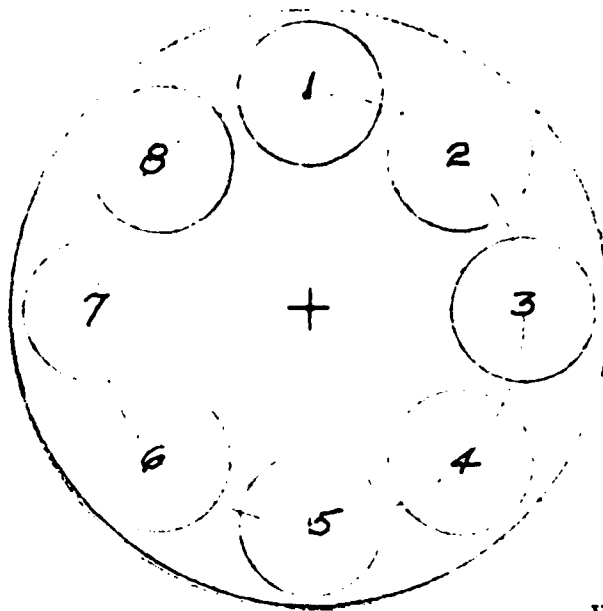
Viewed from front

TABLE I

Readout Position	J1 pins 1 & 2 (Volts)	Filter Shipped (μ)
1	3.490	2.2
2	4.127	5
3	4.778	8.4
4	0.303	11.5
5	0.960	Blank
6	1.577	Open
7	2.240	Open
8	2.874	Open

FILTER WHEEL

5) <u>Electronics:</u> The Model LN-6/C preamplifier features a cooled 1st stage J-Fet mounted near the bolometer with the remaining electronics and bias circuits located in the control box on a top flat of the dewar. (See LN-6/C instruction section).

6) <u>Optical Baffling:</u> A light-tight baffle box with several apertures restrict the input focal ratio to about F/24. Blackening of the internal baffle structures serve to further reduce reflections and suppress excess background noise.

7) <u>General Notes:</u>

a) All metal on the cold plate is O.F.H.C. copper, gold plated to prevent tarnish and assist cooling.

b) Wiring is #35 teflon-insulated Constantan, varnished down to suppress excess microphonic noise.

c) The outer vacuum window is 2 mm thick KRS-5 with transmission as shown on the enclosed graph.

d) The system detector beam profile was mapped utilizing a small chopped source at a distance of about 350 cm. A plot of this response is shown on the enclosed curve.

e) The filter wheel has been shipped with four narrow-band filters installed. Identification of these units is shown on the filter wheel sketch. Note that positions 1 and 2 feature a thru aperture of 6 mm while positions 3 and 4 have an aperture of 3 mm.

f) Filters may be changed or added to the wheel in the following manner:

1. Invert the dewar on the bench and remove the outer case and radiation shield bottom caps.

2. Remove one of the side panels of the motor drive box. This will allow manual control of the filter wheel drive.

3. Rotate the wheel to expose the set screw heads of the shaft coupler. The front screw (nearest the vacuum window) should be removed to decouple the drive motor from the wheel.

4. Loosen the set screw of the shaft retainer located at the radiation shield heat sink module. This will allow the shaft to be moved to the rear and fully decouple the filter wheel. It will also be necessary to loosen the rear plate of the motor housing to fully allow movement of the entire motor/shaft apparatus.

5. Loosen the six, 4/40 hold-down screws located in the foot of the filter wheel bracket. This will allow the entire apparatus to be removed from the cold plate for easy installation of new filters. The filter recess is 0.750 + .005 with 0.625 thru aperture.

6. Filters are retained within the wheel by means of small clips. Insure that these are tight and hold the filter quite firmly.

7. Reverse the above procedure to reinstall the wheel. Insure that the brass fixture at the face of the radiation shield cooling box actually applies positive pressure to the face of the box. This insures adequate heat sinking of the rod to the radiation shield and preserves thermal integrity.

g) The bolometer load resistor consists of dual 10.0 megohm Nichrome chip resistors mounted within a flatpack, wired in series, and bonded to the rear of the detector substrate.

8) Cryogenic performance of the dewar is heavily influenced by the massive optical installation, the filter wheel with remote drive, and the aperture slide. Measured LHe boil-off at 4.2°K indicated a hold time of about 26 hours per fill based on the design volume of 1.45 liters. This should translate to about 15 hours at 1.6°K after a normal pumpdown.

The initial precool LN2 should remain in both containers for at least one hour to insure complete cooldown of the filter wheel and control rod. After LHe transfer, allow the initial boiloff to subside somewhat ($\sim$ 30-45 min) before pumping. A normal pump-down will consume 45-60 minutes and some frosting of the pumping device will occur.

The LN2 boil-off indicated a hold time of about 20 hours per fill. The volume is 0.8 liters.

The personnel of Infrared Laboratories, Inc. stand ready to assist you. Please do not hesitate to call on us.

ARNOLD W. DAVIDSON, MGR.

BOLOMETER CHARACTERISTICS
TEST DATA SHEET
UNIT NO. _1059_

TEST CONDITIONS

BACKGROUND - $\sim 10^{-7} w$

BOLOMETER TEMPERATURE - $1.6°K$

BOLOMETER AREA - $1.05mm \times 1.20mm$

BOLOMETER THICKNESS - $\sim$

FILTERS -

  SEE BOLOMETER NOTES

T_o _____ $1.6°K$

G _____ $\sim 1\mu w/°K$

R_o _____ $\sim 19m\Omega$

S _____ $2.2 \times 10^6 v/w$

N.E.P. _____ SEE BELOW

NOTES: _____

D - C LOAD CURVE DATA			NOISE (V_N) $(10^{-9}$ VOLTS/HZ$^{1/2})$				
I_B' (ua)	E_1 (VOLTS)		BIAS (ua)	FREQUENCY (HZ)			
			Amp # 922	20	40	80	
0.013	0.248	—	SHORTED	5.6	5.2	48	—
.020	.349	—	~ 0.25	46.8	38.2	34.1	—
.028	.443	—					—
.046	.593	—					—
.064	.721	—					—
.085	.799	—					—
.105	.904	—					—
.148	1.043	—					—
.193	1.133	—					—
.240	1.204	—					
.290	1.252	—					
.340	1.255	—					
.380	1.31	—					
.430	1.33	—					

FREQUENCY RESPONSE		BIAS RESPONSE	
FREQUENCY (HZ)	OUTPUT (%D.C.)	BIAS (ua)	OUTPUT (% OF D
40	100	0.15	100
60	97	.25	95
80	87		
100	77.5		
120	68		

N.E.P. $\left(\dfrac{V_N}{S}\right)$

20 HZ:

$$N.E.P. = \frac{4.63 \times 10^{-8} v/Hz^{1/2}}{2.2 \times 10^6 v/w (.95)} = 2.2 \times 10^{-14} w/Hz^{1/2}$$

* - BIAS CONDITIONS

7.0V @ 20mΩ

D-C LOAD CURVE
TEST DATA SHEET
UNIT NO. 1044
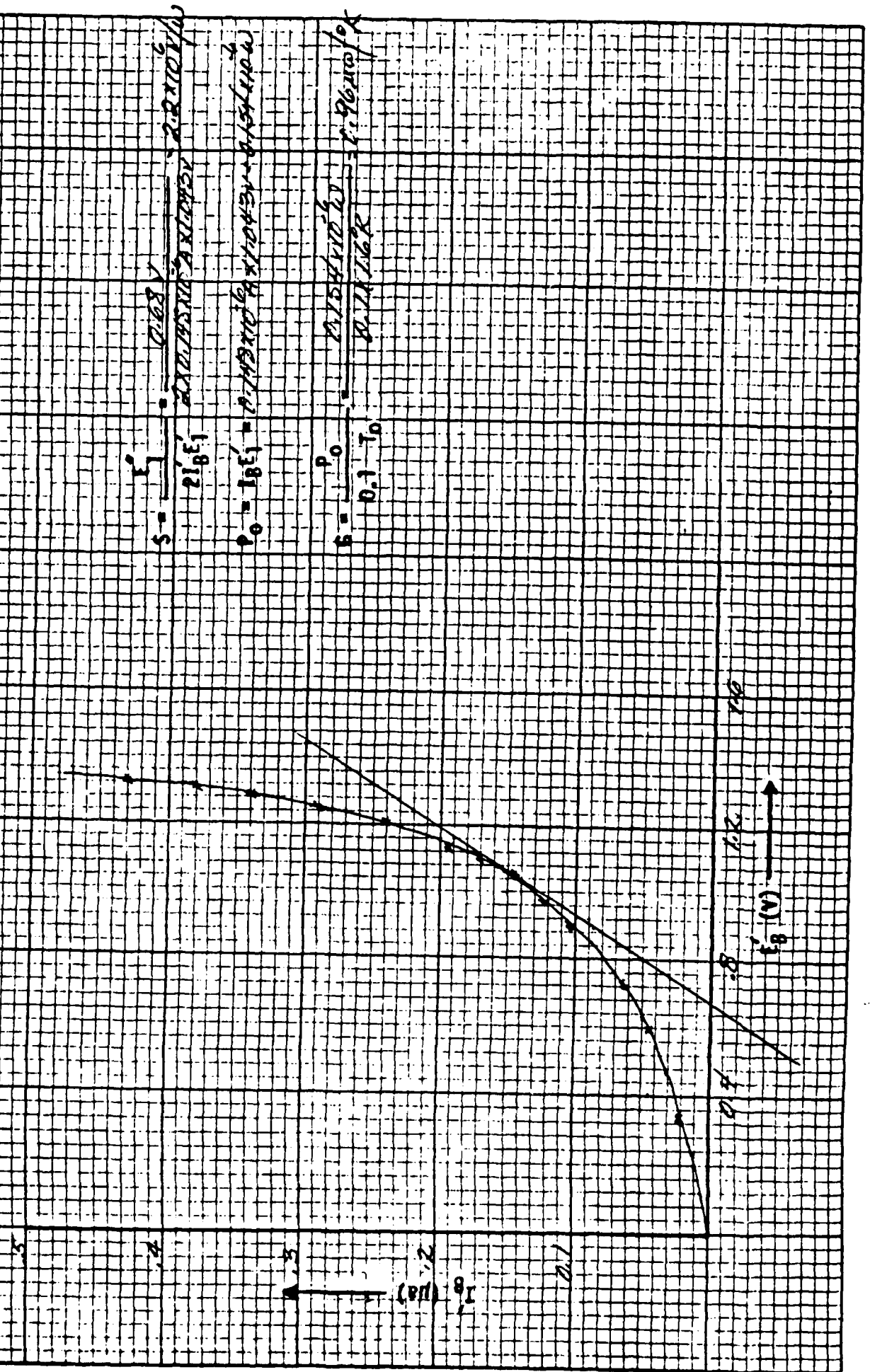
FREQUENCY RESPONSE
TEST DATA SHEET
UNIT NO. V2254

RESPONSE (% OF D. C.)

FREQUENCY (HZ)

20   40   60   80   100   120

20   40   60   80   100
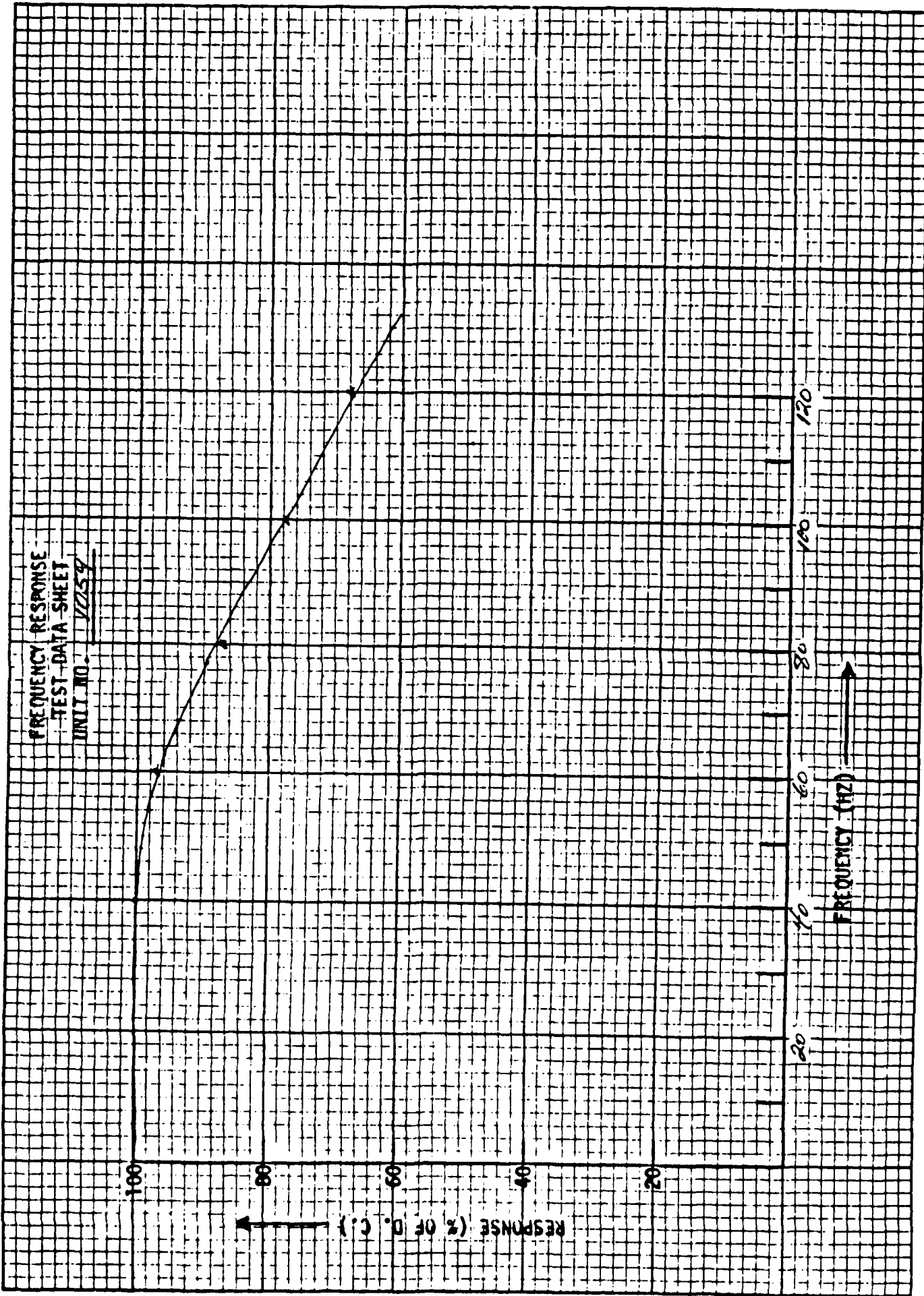
LN-6/C PREAMPLIFIER

The LN-6/C preamplifier is a low-noise voltage amplifier employing remote first stage electronics. By placing the first amplifier stage near the detector on the cold surface, microphonics and excess input capacitance are essentially eliminated. This preamplifier is ideally suited to Infrared thermal sensors such as Bolometers operating from 0.3K to 4.2K at very high impedance. The J230 JFET remote amplifier along with its thin film heater are mounted on a thin-wall fiberglass thermal insulator, allowing 77K operation of the FET even when the module is mounted to a low-temperature cold plate. Power dissipation to the cold surface is less than 3mW. The system load resistor is thermally sunk to the liquid Helium surface to minimize its Johnson noise, and a small (#40) constantan wire connects it to the remote amplifier module.

Bias on the detector is conveniently switched from the preamplifier enclosure, and a BIAS TEST BNC jack allows monitoring of the applied bias as well as providing an input for external bias.

Load curves can be measured conveniently at test points provided on the circuit board.

Power is supplied by two internal 9volt batteries and continuous operation up to 100 hours is standard.

LN-6/C SPECIFICATIONS

First Stage	Remote at cold surface
Voltage Gain	200/1000 $\pm$5 percent (switched)
Input Impedence	> 1 X 10^{13}
Output Impedence	< 500 ohms
Frequency Response	0.75Hz to 30KHz
Maximum Output	$\pm$7V
Power Requirements	$\pm$9V (Batteries included) @ $\pm$2mA
Shorted Input Noise	< 5nV/Hz$^{1/2}$
Bias Voltage	Switched, to suit application
Size	6 1/2" x 3" x 4" wide
Weight	Approx. 2 pounds

LN-6/C PREAMPLIFIER
OPERATING INSTRUCTIONS

1. **Initial Inspection**

   After unpacking the preamplifier, remove the 4 lid screws & inspect to see that two, 9V Alkaline batteries are in place and connected with battery snaps. It will be necessary to have the lid removed to attach the unit to a dewar or other device containing the detector. Check to see that preamplifier power is turned off, and that the bias & input switches are turned off.

2. **Attaching Preamplifier**

   With lid removed, attach the preamplifier to a dewar or other device containing the detector with two, 8-32 screws near the connector cut-out at the rear of the box. Some installations will offer a tapped hole to match the clearance hole near the base of the two batteries at the top rear of the box. The standard clearance hole is for an 8-32 screw. Plug the electrical connector (preamplifier input connector) into the appropriate jack and replace the lid.

   Note: Refer to 6 if wiring of the cold module is to be done by the customer.

3. **Normal Operation**

   Check to see that the bias is correctly set for the particular detector being used. To do this, connect a voltmeter to the "Bias Test" BNC jack and turn "Bias On" switch to "On".

   Bring the detector to normal operating temperature and turn the preamplifier power on (Input switch off). "White" noise should be evident at the output BNC jack, as seen on an oscilloscope or spectrum analyzer, with zero volts DC ± 100 mV. Noise should be less than 3 nV/Hz$^{\frac{1}{2}}$ at 20 Hz and above, referred to preamplifier input.

   Unshort the input and allow 60 seconds for stabilization of the circuitry before making measurments. Signals as large as ±7.5 V at the output, corresponding to ±7.5 mV @ gain = 1000 at the input, may be displayed without saturating the amplifier.

4. Cold Module Operation

Under normal operation, the cold module is "self-starting" due to the heater resistor (which dissipates about one milliwatt) cemented to the active end of the cold module. Since JFet electrical conduction diminishes at temperatures below 60K, this heater insures adequate temperature rise, even from 1.8K, to allow the self-heating of the JFet to take place and maintain its internal die in the range 70 - 80K. In some cases (e.g., short wires to cold surface) as much as ½ hour of time is required for complete temperature stabilization of the active end of the JFet cold module.

5. Detector Load Curve Measurement

Since the detector lead is not brought out directly, measurement of the load curve requires monitoring of the cold JFet source. This voltage is nominally 1 volt ± 0.4V with no bias applied to the detector. This source voltage must be <u>subtracted</u> from the measured voltage to obtain a normal <u>load curve</u>. Bias for the load curve is injected at the "Bias Test" BNC jack with the <u>Bias switch turned off.</u>

For convenient connection to the JFet source, a BNC type connector has been provided. This has been labeled "V_s" and is located at the top left side of the case.

The well-known formula gives detector current:

$$I_D = \frac{V - V_B}{R_L}$$

where I_D = detector current
V = bias voltage applied at Bias Test BNC jack
V_B = detector voltage (minus source voltage at zero bias)
R_L = value of load resistor in ohms

6. Cold Module Installation

Refer to drawing and notes supplied. The low thermal conductance tube, which connects the lower part of the module (mounted to cold surface) to the active end, is very fragile; great care should be taken to insure that no forces or torques are applied to this tube during installation. Constantan and Manganin wire are available from the factory.

<u>CAUTION</u>: Use only low thermal conductance wire to connect the module active end to the load resistor & detector. Failure to do so will cause overcooling of the module during operation and possible malfunction of the JFet (not permanent).

7. Maintenance

The only maintenance required under normal conditions is replacement of the power supply batteries. To do this, turn the preamplifier off and remove the lid. Carefully unsnap the battery electrical connectors and place them to the side. Loosen the 4-40 screw (with nut), at the top left of the enclosure, which retains ½ of the battery hold-down clamp. Remove & replace the batteries with Alkaline 9V units - other types will have shorter life, except for certain re-chargeable Nickel-Cadmium cells. Tighten the screw, making certain that the battery posts are well below the lid level of the enclosure. Replace the electrical snaps.

Normal battery life will exceed 75 hours of continuous operation.

8. Troubleshooting (Requires D.C. voltmeter with input impedance of 10 megohms or greater)

In case of difficulty, use the following procedure to isolate a fault. Always check power supply batteries before beginning. Acceptable range is ± 8.0 V to ±9.2 V.

A. Short input
B. Turn unit on
C. Measure D.C. voltage at output BNC jack
    1) If value is 0 ± 100 mV, go to E.
    2) If value is outside this range, go to D.
D. Measure D.C. voltage at TP2 (refer to board layout sketch)
    1) If value is 0 ± 100 mV, Op 12 is probably faulty
    2) If value is outside this range, Op 27 has probably failed. (Note: Grounding TP2 with a test lead should cause the output voltage at BNC jack to be 0 ± 100 mV).
E. Measure voltage at TP1
    1) If value is 1 ± .4 volts, trouble is probably in the detector load resistor circuit.
    2) If value is outside this range, be sure that sufficient time has elapsed after amplifier turn-on to allow start-up of the JFET module (See Section 4). Check bias voltage to see if it is in the correct range. Start-up not required if the dewar is at ambient temperature.

Note: Dewar may be either cold or warm to diagnose faults using the above procedure.

F. Consult factory if difficulty persists.

9. Spare Parts

A complete stock of spare parts for immediate shipment is maintained at the factory for this unit, both at the component and subsystem levels.

ADDENDUM TO LN-6C PREAMPLIFIER OPERATING INSTRUCTIONS

CAUTION: Never turn the disconnected amplifier on unless "Input On" switch is in the off position or unless a signal generator (10 K ohms or less impedance) is plugged into the "Input Test" BNC jack.   When the cold module is properly connected to the amplifier, it is safe to turn the unit on.   These precautions are necessary to avoid reverse - bias of the input coupling capacitor, rendering it permanently shorted.

NOTE: The "Input on" switch for some models is connected to the positive terminal of the input coupling capacitor instead of the negative end as shown on the schematic.
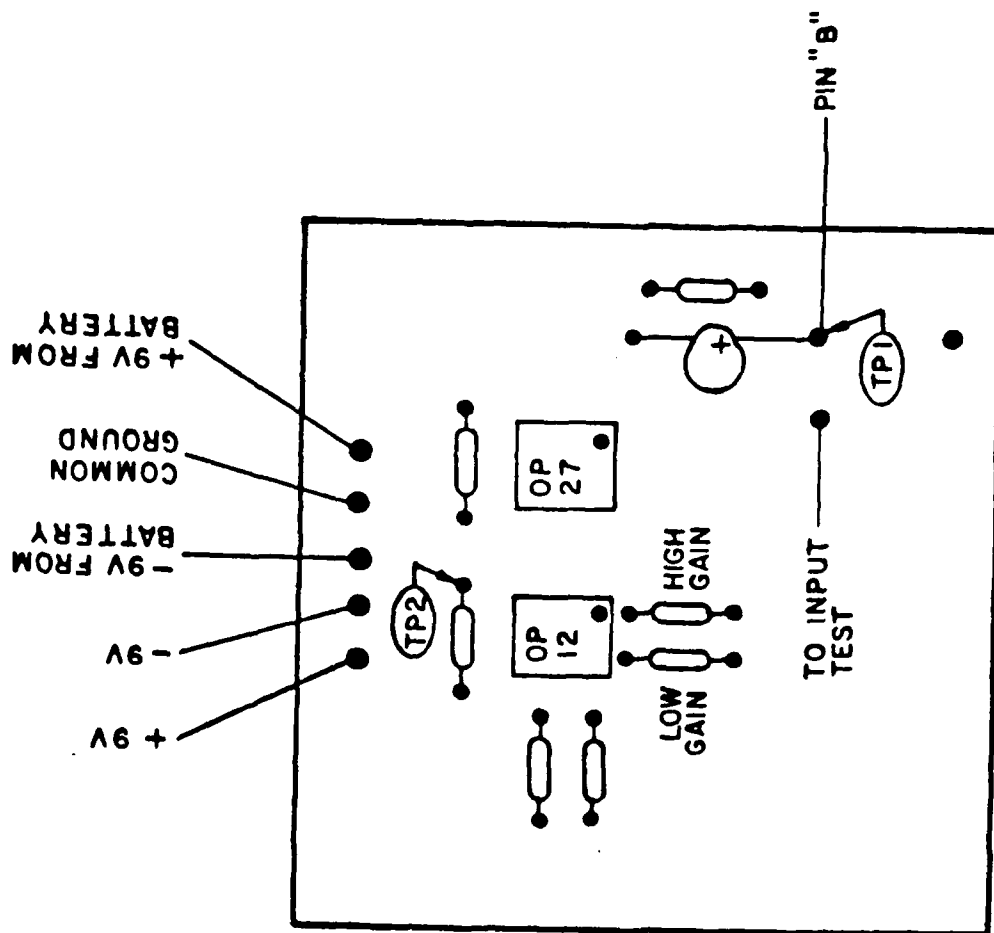
LN6-C BOARD LAYOUT

INFRARED LABORATORIES INC
1808 EAST 17th STREET
TUCSON, ARIZONA 85719
U.S.A.

SCALE

PIN "B"

+ 9V FROM
BATTERY

COMMON
GROUND

- 9V FROM
BATTERY

- 9V

+ 9V

TP2

TP1

OP 27

OP 12

HIGH GAIN

LOW GAIN

TO INPUT TEST

LN-6/C COLD MODULE

JFET

STAND-OFF
5 EACH.

RH

FIBERGLAS
INSULATOR

.375

MOUNT TO COLD
SURFACE.#4-40 SCREWS

RL

BOL

J230

HEATER 61K1

PIN A

GND

PIN B

TO PIN A
TO PIN B
TO BOLOMETER

TO GROUND

6 PIN CONNECTOR

A	DRAIN
B	SOURCE
C	BIAS
D	---
E	GROUND
F	---
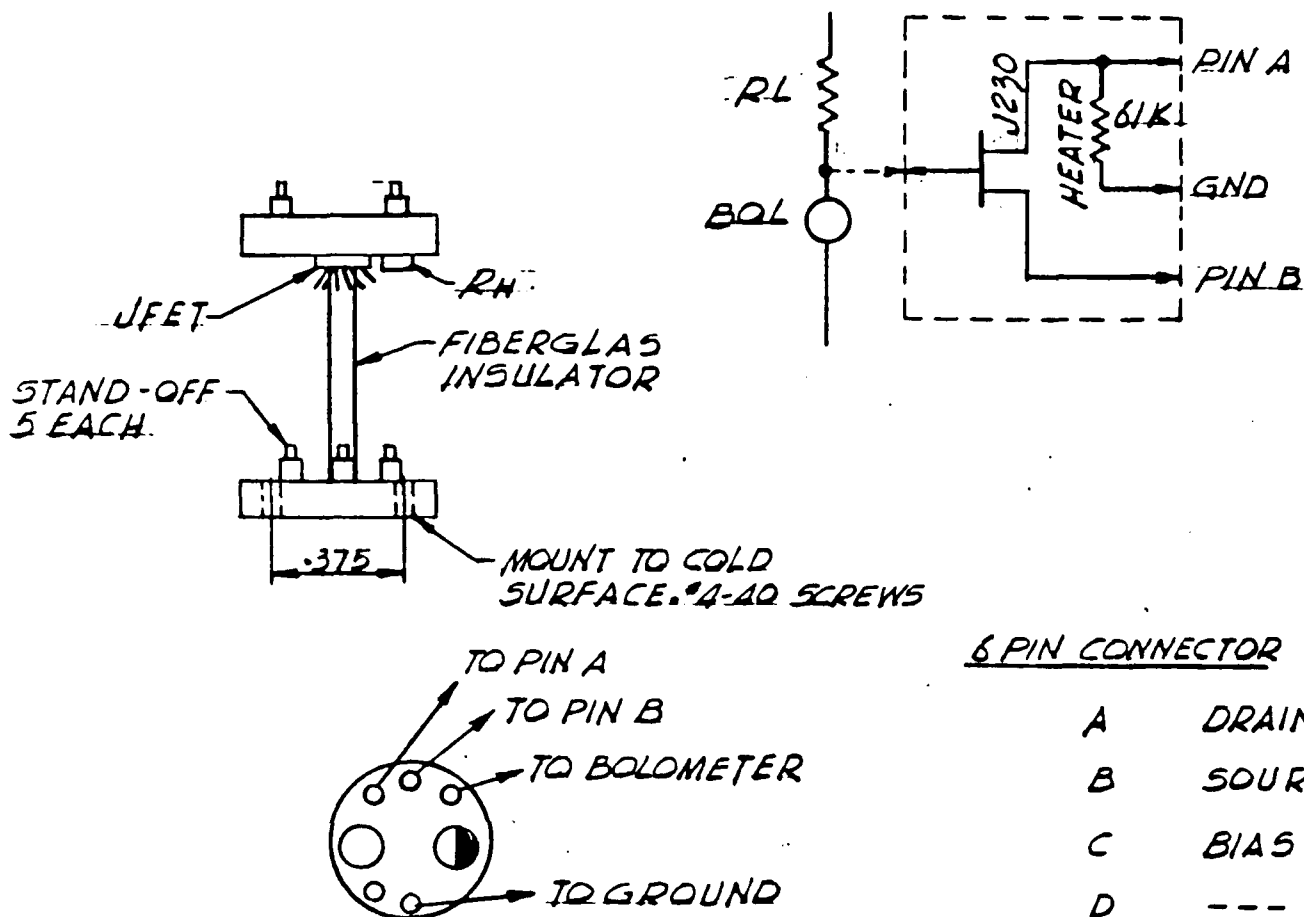
Notes for Installation

1. Use Constantan or Manganin wire (#30 or smaller) to connect module to connector.

2. Load resistor should be mounted on cold surface as close as possible to detector.

3. The G_1 lead from cold module to junction of R_L & Det should be kept as short as possible. Cement this lead to the cold surface to avoid microphonics.

COLD MODULE (TOP VIEW)

R_B = BOLOMETER LOAD RESISTOR - 26 mΩ

R_{HEAT} = "COLD START" HEATER

solubility

KRS-5 is somewhat less soluble than that of TlBr, since TlI is about a hundred times less soluble than TlBr.

optical properties

Refractive Index: Varies from 2.62758 at 0.577 μ to 2.21721 at 39.38 μ[1]. The dispersion formula is:

$$n^2 - 1 = \sum_{i=1}^{5} \frac{K_i \lambda^2}{\lambda^2 - \lambda_i^2}, \text{ where } \lambda \text{ and K are:}$$

i	λ_i^2	K_i
1	0.0552	1.8293958
2	0.0625	1.6675593
3	0.1225	1.1210424
4	0.2025	0.04513366
5	27089.737	12.380234

Temperature Coefficient dn/dT[1]: Is given from 0.577 to 39.38 μ. It varies from $25.4 \times 10^{-5}/°C.$ to $-15.4 \times 10^{-5}/°C.$ Refractive indices are also given for 0.6907, 0.6438, 0.5791, and 0.5770 μ, for temperatures from -5 to $+45°C.$ in steps of 5°C.

Dispersion dn/dλ: See page 9.

Transmission Range[2]: In prism thickness from 0.6[2] to 40 μ for filters up to 60 μ.

WAVELENGTH (MICRONS)
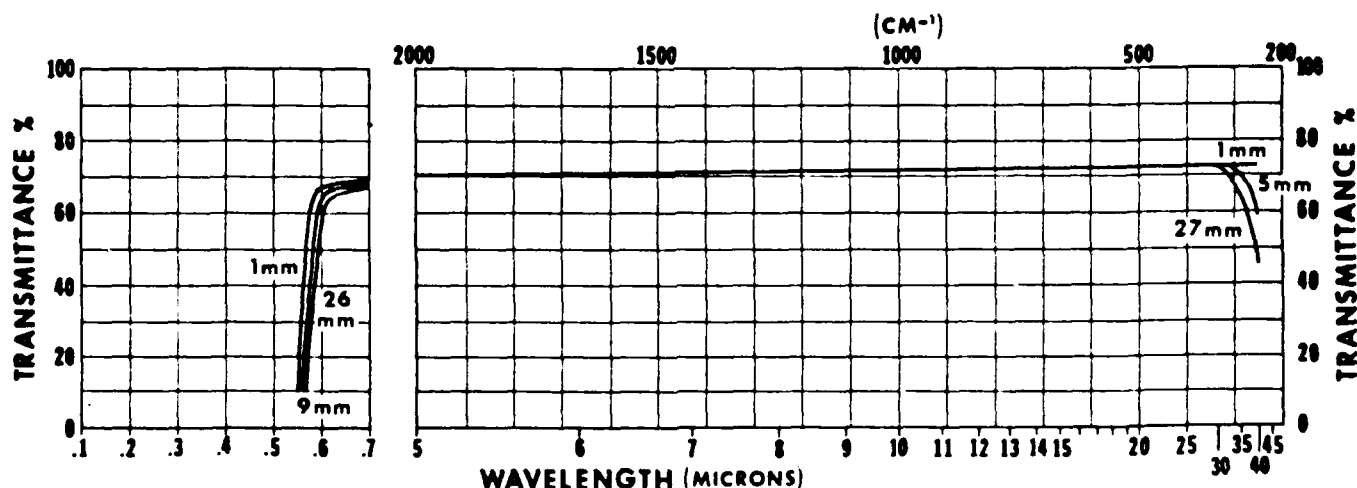
Reflection Loss:

For n_D = 2.61 of a plane parallel plate and θ = 0°
Without multiple reflection 36%
With multiple reflection 33%

Reststrahl Frequencies: Reststrahl maxima: Estimated to be at 135 μ, and reflection above 50%, similar to TlBr. Range $112 - > 400 \mu$.

BEAM PATTERN

HPBW = $f/24$

RESPONSE (NORMALIZED)

Θ (DEGREES)

8/8/86
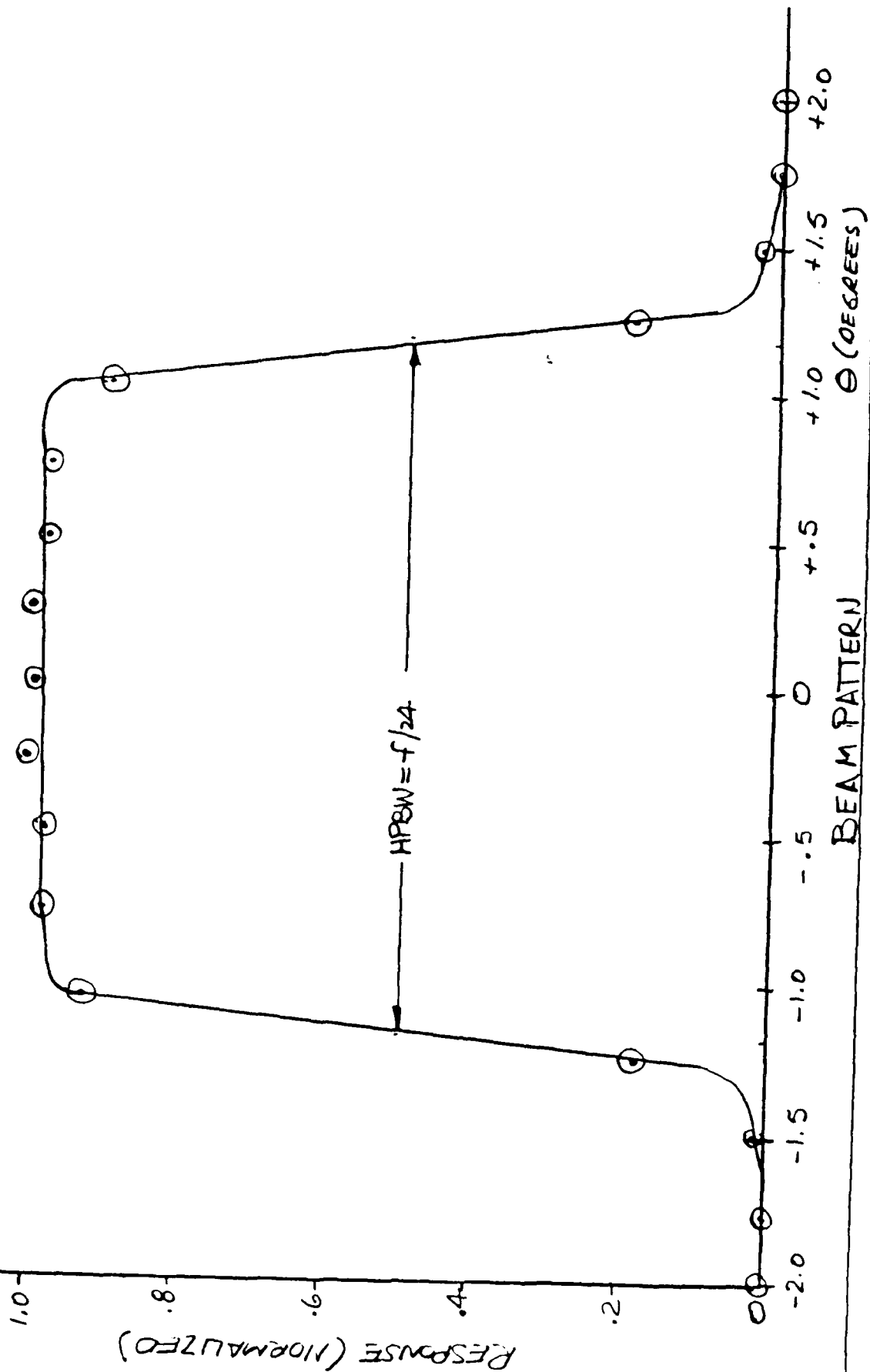
OCLI OPTICAL COATING LABORATORY, INC.

SPECTRAL PERFORMANCE

DATA IDENTIFICATION
C419

SAMPLE IDENTIFICATION

INST. OPERATING PARAMETERS

CARY 90   IR-12
CARY 14   IR-4
PE 180

TEST CONDITIONS

λp ~ 5.03μ
BW: 0.89μ

WO5052-4

4.533μ →   ← 5.42μ

100   10μ
90   90
80   80
70   70
60   60
50   50
40   40
30   30
20   20
10   10
0   0

5.0   6.0

$\lambda_o = 2.284\,\mu$

$HBW = 0.47\mu$

'022 84 - 7

$\lambda_o \approx 2.284\mu$ W02284-7

$HBW = 0.47\mu$

$\dfrac{2.050\mu}{2.049\mu}$ .081
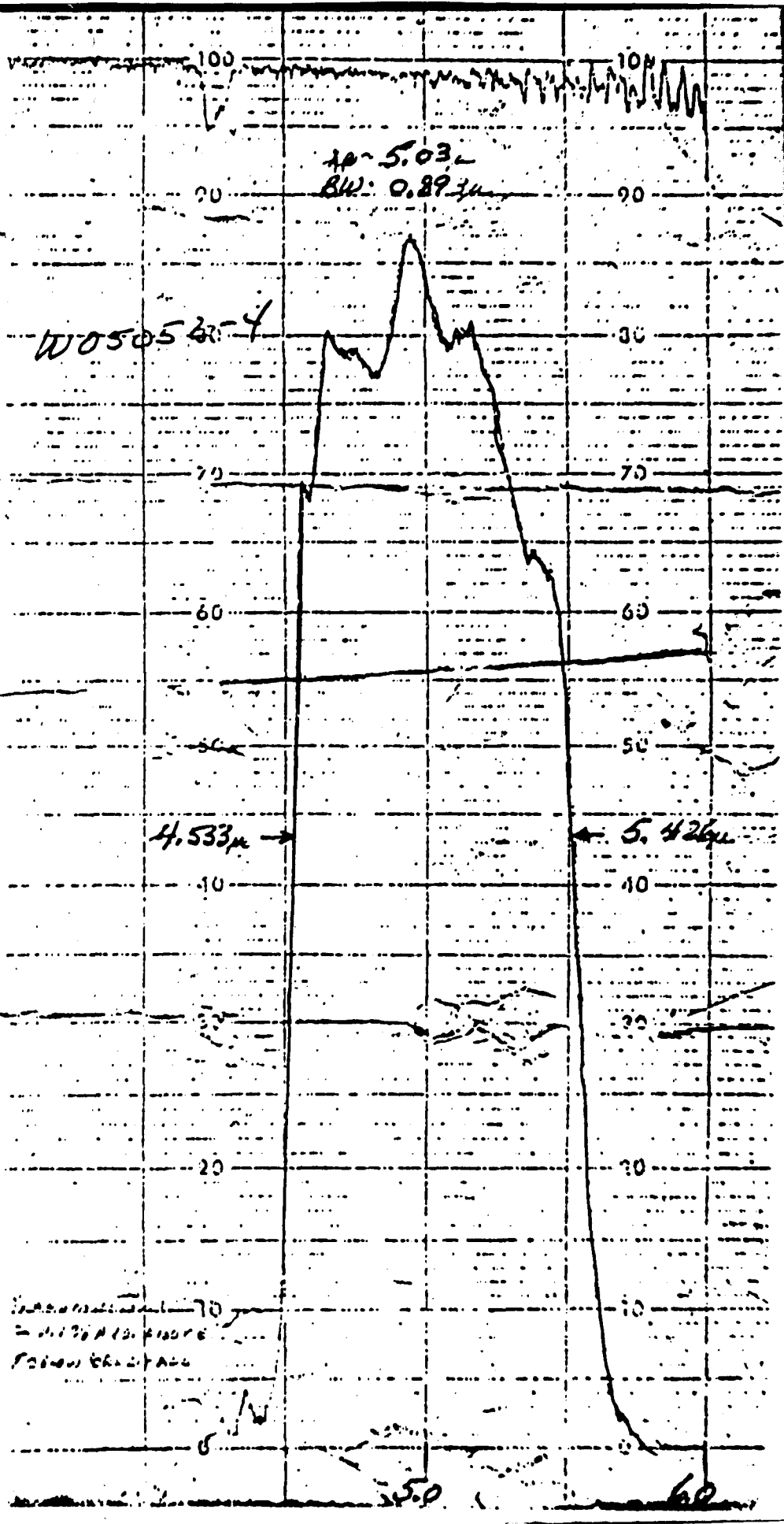
'EMISSION
% ABOVE AND
ON & BELOW
λ_o.

TRANSMISSION :
≥ 0.1% Above Band
To 5:0n.4 Below
Band →

2.0   2.1   2.2   2.3   2.4   2.5

A. GENERAL DESCRIPTION

A complete detector system consists of three main parts: the detector mounted on a copper substrate, the liquid helium dewar, and the preamplifier. The preamplifier is bolted directly to the side of the dewar case and is powered by an external battery supply. This system is mechanically rugged and can be operated under a wide range of environmental conditions and in any attitude within a few degrees of horizontal. The usual precautions for handling cryogenic liquids should be followed.* The case of the dewar is evacuated to forepump pressure before use. After periods of several weeks, it may be necessary to reevacuate the case. Access to the detector work surface is obtained by removing the bottom plate of the dewar and the radiation shield. A system of internal supports is provided to allow accurate alignment of the cooled surface with respect to the outer case. These supports are the most fragile components in the system. Excessive mechanical shock may fracture one or more of the

----

*One of several standard textbooks on this subject is Cryogenic Engineering by Russell B. Scott, published by D. Van Nostrand Company, Inc., Princeton, New Jersey, Copyright, 1959.

supports. In order to minimize the possibility of such damage in shipment, the following precautions have been taken. The two bottom plates have been removed and a rigid clamp attached in their place with the internal supports partially loosened. It is necessary to remove the clamp and tighten the internal supports to produce the desired alignment. The two bottom plates may then be replaced according to the enclosed instructions. The case can then be evacuated to forepump pressure and dewar cooled for operation.

B. COOLING THE DEWAR

After evacuation of the case to forepump pressure, the dewar should be precooled with liquid N_2 or liquid air. A minimum precooling of 5 minutes should be used. Precooling for several hours reduces the consumption of helium.

Before transferring liquid helium, all precoolant must be removed, either by pouring out the liquid or by transferring it. The helium transfer tube should be flushed with helium gas and slowly inserted into the storage dewar. Sealing the top of the storage dewar traps the evolving helium gas and starts to build up pressure which vents through the transfer tube. When the tube is touching bottom of storage dewar, an overpressure of approximately 1/4 - 1/2 psi of helium should be maintained. As the transfer tube cools, it should be inserted into the experimental dewar until it almost touches bottom. Rapid efflux of cold vapor continues for several minutes until liquid begins to collect. A sudden drop in blow-off signals that the liquid is collecting. At a pressure of 1/2 psi, the 1.2 liter dewar should fill in about 2 minutes. When liquid reaches the restricted neck, a sudden jet of very cold gas signals that the transfer is complete. The pressure applied to the storage dewar is released and the tube withdrawn. Do not fail to cap the storage dewar or to turn off the supply of helium gas.

A normal transfer will consume about 2.5 liters of liquid helium and will last about 5 minutes. It is normal for the initial boil off to be readily visible. As the radiation shield cools, this visible plume will gradually disappear.
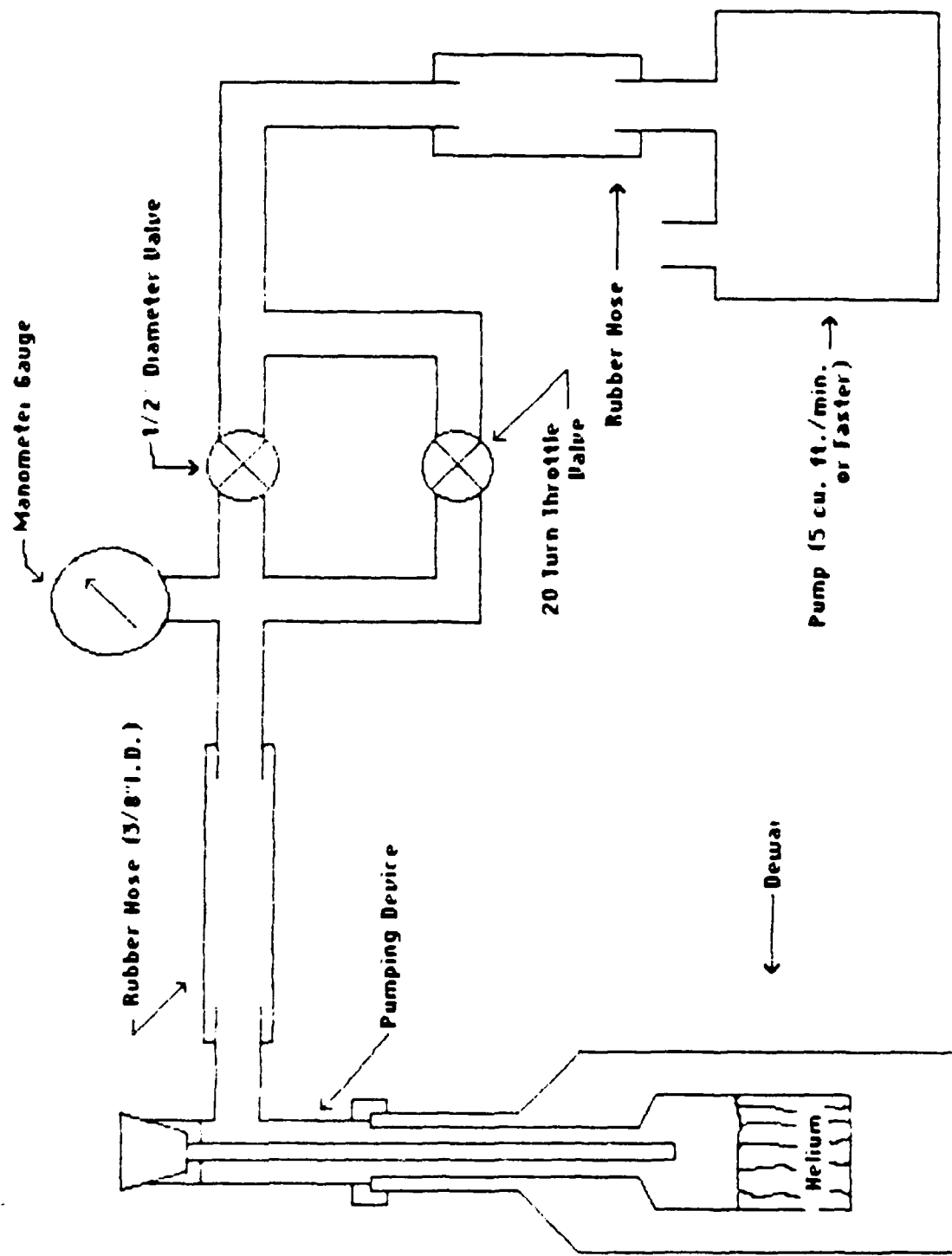
Monometer Gauge

1/2" Diameter Valve

Rubber Hose

20 Turn Throttle Valve

Pump (5 cu. ft./min. or faster)

Rubber Hose (3/8"I.D.)

Pumping Device

Dewar

Helium

Figure 1 - Pumping System

C. PUMPING ON THE DEWAR

At sea level liquid helium boils at 4.2°K. Most bolometers will be operated below the lambda point of liquid helium at 2.17°K. In the super-fluid state, liquid helium is quite stable.

By reducing the vapor pressure above the liquid, temperatures down to 1.2°K may be attained. 1.8°K corresponds to a vapor pressure of about 14mm Hg, a very desireable operating point. Figure 1 shows the pumping system used for this purpose.

A slow pump-down conserves helium. A good indicator is the temperature of the pumping fitting. If ice forms on the outside, you are going a bit fast. After about 45 minutes the lambda point at 38mm Hg should be reached. Once through the transition, the throttle valve can be opened and equilibrium can be reached in about 15 minutes. This recommended period of 1 hour can be shortened to perhaps 30 minutes, but going too fast may simply pump all the helium out of the dewar.

In some pumping systems thermo-mechanical oscillations may occur and rapidly consume the liquid helium. This problem is always solvable by increasing or decreasing the diameter of various sections of the system. This is an annoyance which fortunately is not too common.

A word of caution about air leaks in the pumping system: If air leaks in, it will freeze in the neck tube. If the neck tube becomes blocked, the dewar can rupture! Test for air leaks beforehand and always use the safety feature built into the pumping fitting. The reentrant tube prevents complete blockage of the neck should an air leak be present.

D. RECOMMENDED TEST PROCEDURES

D.C. Load Curve:

With bath stabilized at operating temperature and instruments connected as shown in Figure 2, the E. I. characteristic may be measured. The imput impedance of the voltmeter used to measure E_1 should be more than 10 times R_0, the bolometer resistance. The current, I_B, is simply, $(E_2-E_1)/R_L$. A typical load curve is shown in Figure 3.
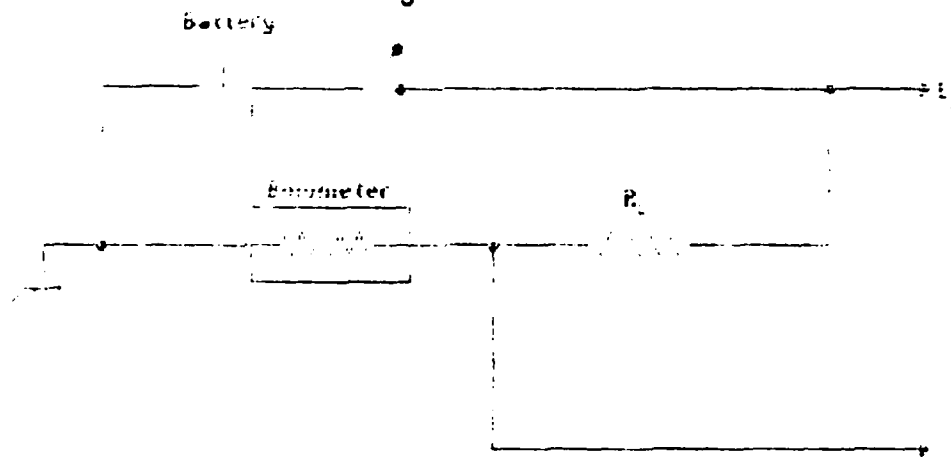
Note: E_2 varied from 0 to R_L/I_B (Max)

$E1$ is measured by high impedance voltmeter

Figure 2 - LOAD CURVE SET-UP
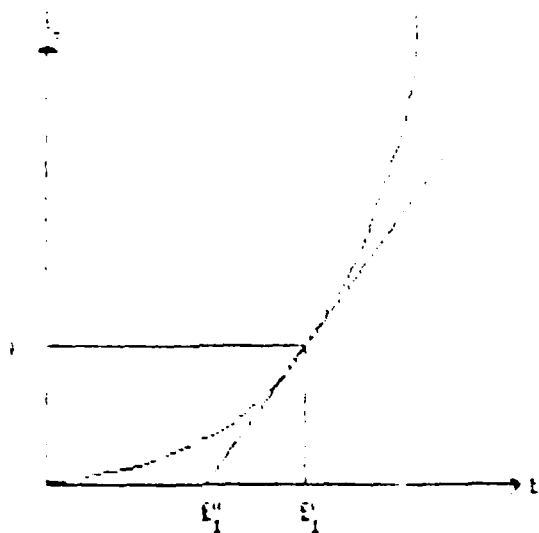
Figure 3 - LOAD CURVE

FREQUENCY RESPONSE:

If a bright source can be placed close enough to the window, the arrangement of Figure 4 may be used where the oscilloscope responds to D.C. If higher gain is needed, A.C. coupling must be used. The preamplifier, for example, could be utilized with a low gain oscilloscope. In any case, it is necessary to be certain that the true D.C. signal level has been measured, i.e. the A.C. response must be low enough to allow extrapolation to zero frequency. If the bolometer is properly constructed, it will have a single time constant and its frequency response will be as illustrated in Figure 5a. If, however, there are two time constants, with one very long, the result may resemble Figure 5b.
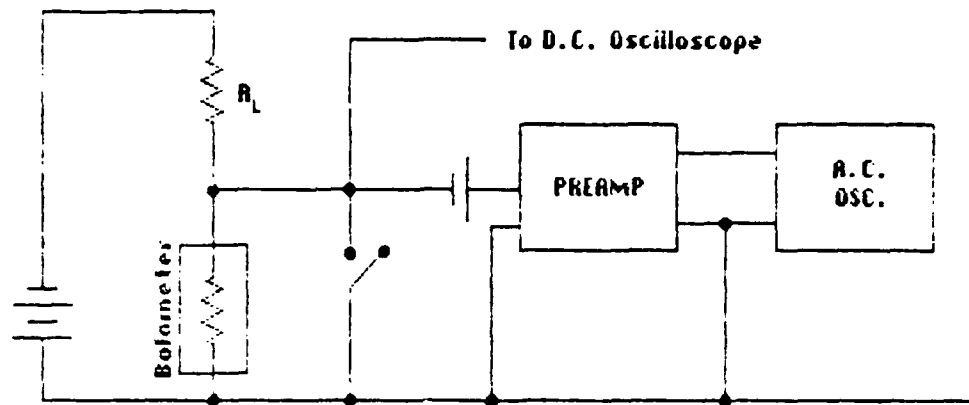
Figure 4 - FREQUENCY RESPONSE SET-UP
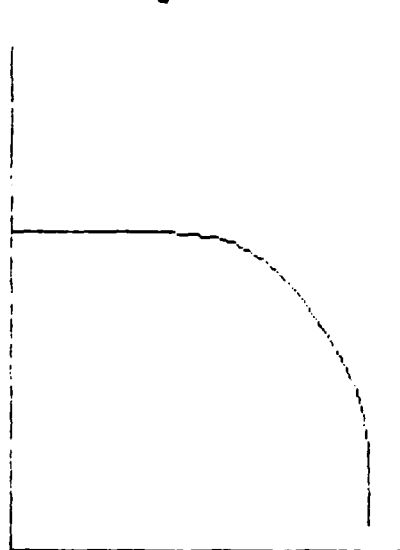
Figure 5a - Frequency Response,

Single T
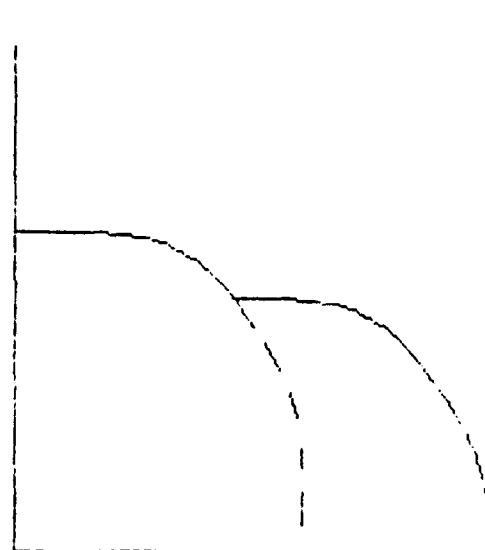
Figure 5b - Frequency Response,

Double T

RESPONSE VERSUS BIAS CURRENT:

The A.C. output should be measured for various bias currents up to the highest used in the load curve and well beyond the value which produces maximum output.

ABSOLUTE NOISE MEASUREMENT:

This is the most important measurement to be undertaken here. It verifies that the bolometer is working properly and that no serious degradations are occurring in the detector or associated equipment. A number of difficulties may arise, although the following procedures are intended to avoid most of the common problems encountered in noise measurements.

(a) In the frequency range of interest, 10 to 1000 Hz, a number of narrowband filter systems are available. Any filter may be used here if its effective $Q \approx \Delta f/f \geq 10$. Narrow bandwidths are undesirable since if $\Delta f < 1$ cps, inconveniently long measuring times become necessary. An inexpensive filter may be constructed using the circuit supplied upon request. In choosing the frequencies to be used the power line fundamental and its harmonics should be avoided. We usually employ the following set of frequencies: 10, 20, 40, 80, 160, 320, 640 Hz.

(b) The voltmeter need not be of the true rms variety since we will calibrate it on noise very similar to that we wish to measure. A linear amplifier may be needed between the filter and the voltmeter to increase its sensitivity to about 0.1 mv rms full scale.

(c) It is necessary that the preamplifier have performance equivalent to our standard model; the circuit and a brief description are included.

(d) After connecting the apparatus as shown in Figure 6, checks must be made to eliminate all interference from power line or other sources. With preamp input shorted or connected to the detector, the waveform on the oscilloscope must be free of ripple or other signals such as partially rectified r. f. coming from nearby transmitters. Ground loops, lack of a good, common proximity to transformers in oscilloscope or other equipment or poor shielding between detector and preamplifier are common causes of pick-up.
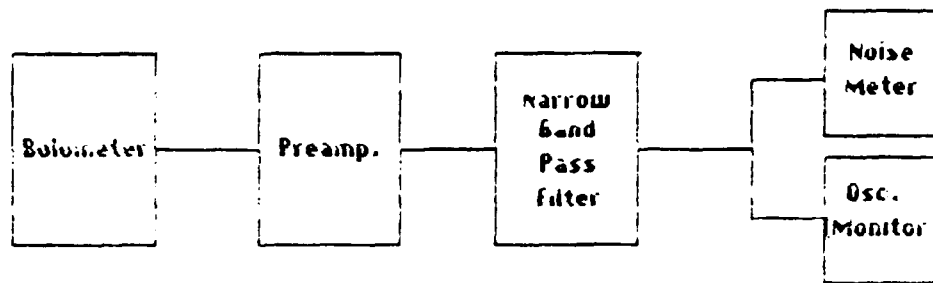
Figure 6 - NOISE MEASUREMENT SET-UP

(e) Once the setup is free of interference, it may be calibrated by placing across the input several resistors of known value. The resulting data should be plotted as follows:
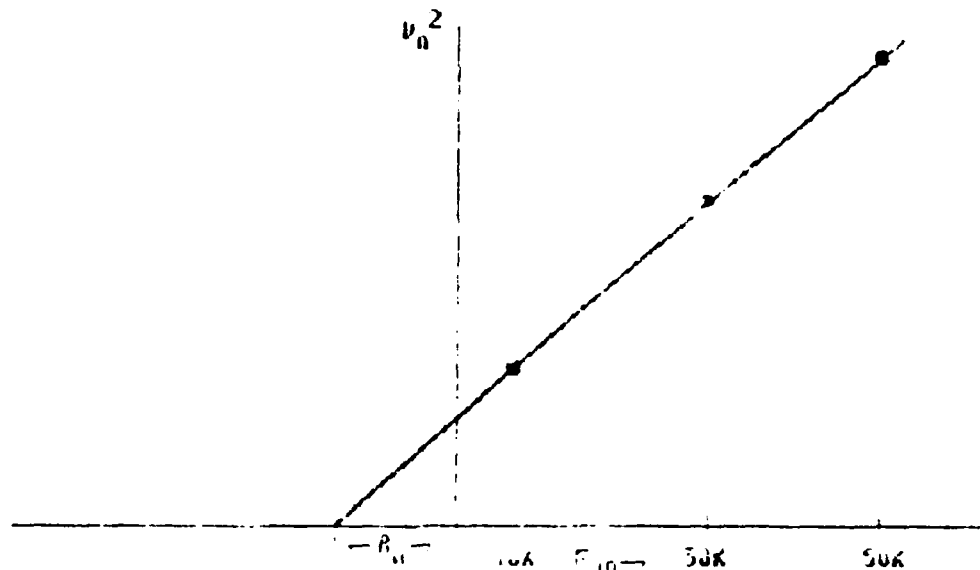
Figure 7 - NOISE CALIBRATION

This procedure should be followed for each frequency to be used. In addition to calibrating the noise meter, it determines the value of R_n, the noise equivalent resistance of the preamplifier.

(f) Detector noise may now be measured as a function of I_B. Values of I_B should be chosen from zero to the highest value on the load curve. Various small batteries can be selected for this purpose. A word of caution on installation of the bias battery is in order: First, always solder leads to each battery to avoid noisy contacts; second, we must solder with great care to avoid damaging the battery; and last, we usually try more than one battery to be sure the battery is not noisy itself. If all is well, the zero bias noise should just equal the calculated value for R_0 and T_0. Optimum value of detector impedance is decreasing as the current increases and this can offset the increasing current noise. These measurements should be carried out for various frequencies including the chosen chopping frequency.

Microphonics and pump noise can complicate the problem of ascertaining true detector noise. Even if the window is blocked off, the slightest motion of the inner parts of the dewar can produce a random

fluctuation in background. The dewar has been constructed to minimize this problem. Also, our preamplifier is relatively non-microphonic. Pump noiise arises when surges in the vapor pressure of the helium bath are large enough to produce temperature fluctuations of the detector. A good test is to suddenly shut off the pump and moniter the noise. Only under rare circumstances have we encountered pump noise.

T_0 (°K)   - Bath Temperature.

R_0 (Ω)   - Bolometer Resistance as $I_B \to 0$.

I_B (amp)   - Bias Current.

E_1 (volt)   - Voltage Across Bolometer.

R_L (Ω)   - Load Resistor, usually cooled.

E_2 (volt)   - Bias Supply Voltage.

S_0 (volt/watt)   - Maximum Responsivity.

$P_0 = I_B E_1$ (watt)   - Bias Power at Maximum Responsivity.

G (watt/°K)   - Thermal Conductance.

T (sec)   - Thermal Time Constant

f_0 (Hz)   - Chopping Frequency.

V_n (volt)   - rms Noise Voltage.

NEP (watt/Hz$^{1/2}$)   - Noise Equivalent Power.

A (cm^2)   - Active Area of Detector (one surface)

D^* (cm⊕Hz$^{1/2}$/watt)   - Detectivity.

Rn (Ω)   - Noise Equivalent Resistance.

$$S_0 = .7(R_0/T_0 G)^{1/2}$$
$$NEP = 2T_0(kG)^{1/2}$$
$$P_0 = .1T_0 G$$
$$S = E_1{}^*/2I_B E_1$$

MODEL HD-3 HELIUM DEWAR

The HD-3 helium dewar features a liquid-nitrogen cooled radiation shield to provide extended helium hold times of up to 140 hours per liter at 4.2 K. When pumped, temperatures as low as 1.4 K may be had with hold times in the 75 hour range. This, compared with the large cold work area and the rugged, all-metal construction, provides the experimentalist with a versatile aid in those cryogenic applications requiring temperatures in the range 1.4 - 4.2 K.

The achievement of the above hold times necessitates a few precautions when installing equipment within the dewar. The 140 hour/liter helium hold time is roughly equivalent to a heat input of 3.5 milliwatts. This is, of course, with all ports closed, but with all supports in place. If a 1 cm^2 aperture is opened in the radiation shield and no restrictions are placed on the incoming radiation, then an additional heat load of about 50 milliwatts is introduced in the cold area, seriously degrading the hold time. This problem can be alleviated to a large extent by the following means

1) Keep the holes in the radiation shield to a minimum and of a minimum diameter.

2) Filters can be placed over the entrance port in the radiation shield if the system spectral response will allow. For example, a quartz filter would reduce the 300K background by about 90%

3) Baffling on the radiation shield entrance port can be utilized if

possible. A short section of blackened tubing will reduce the entrance cone of radiation and attenuate the background radiation appreciably.

4) The radiation shield-cold surface centering and support rods are fabricated from Kel-F rods hollowed out to minimize heat leakage. One spare rod is furnished with each dewar, and additional rods are available from Infrared Laboratories, Inc.

5) All wiring from the cold work area to the outer electrical plug should be of small diameter (#36-40) and of low-loss material (Constantan is very good). Infrared Laboratories can furnish small quantities of #40 Teflon-insulated Constantan wire at no charge if desired.

6) All material mounted on the cold work surface should be clean with the mounting surfaces in intimate contact. Poor contact will introduce a virtual heat leak with mounted equipment never quite attaining the bath temperature.

The liquid nitrogen container has a capacity of 0.8 liters and will provide about 30 hours of hold time. Degradation of this hold time will occur under any of the following conditions:

1) Poor vacuum caused by a case air leak. Introduction of liquid helium into the inner chamber will provide a high vacuum in the vacuum space. A case air leak, in addition to causing an excess helium heat leak, will degrade the vacuum, especially in the outer chamber surrounding the nitrogen container.

2) The two pins centering the radiation shield in the outer case have been hollowed out to minimize heat leak; if additional contact is

added, then a special effort should be made to reduce the cross-sectional area.

3) A wrapping of heavy-duty aluminum foil has been placed over various surfaces of the outer case, radiation shield, and inner helium and nitrogen containers. This serves to reduce surface emissivity and increases the nitrogen hold time by about 20% and the helium hold time by about 15%.

4) All interior surfaces of the dewar should be kept as clean as possible and a vacuum maintained within the dewar vacuum space.

Most equipment can be mounted on the cold work surface through the dewar bottom opening of about 4.75 inches; however, if it becomes necessary to disassemble the dewar to facilitate mounting equipment, then the following procedure should be followed:

1) Invert the dewar in a suitable stand to facilitate ease of access.

2) Remove the dewar bottom plate and the radiation shield bottom plate.

3) Stand the dewar upright on a clean surface and loosen and remove the eight bolts holding the main dewar body.

4) Very carefully remove the inner assembly by lifting it out of the dewar outer case; replace this inner assembly on the dewar stand.

5) Remove the 12 screws holding the radiation shield to its mount; also remove the three nuts holding the radiation shield standoffs. The radiation shield can now be removed by gently prying upward, being very careful not to exert any sideway thrust. The neck tubing is 0.006" wall thickness stainless steel tubing and is fairly fragile.

6) The cold work surface is now exposed and can be utilized to its full diameter. To re-assemble, simply reverse the above procedure.

If it becomes necessary to drill additional mounting holes in the cold work surface, then the shipping brace should be re-installed to reduce the possibility of neck tube damage. Holes should be no deeper than 1/4", as the plate thickness is 0.350 tapering to 0.325 at the center.

It is rather important that the helium pumping device with its built-in safety features be utilized at all feasible times. The heat transfer up and down the neck tube of the dewar is such that it is fairly easy to build up an ice plug in the neck tube. The pumping device bypasses this by allowing an airpath out of the dewar.

COLD WORK AREA
MODELS HD-2,3 DEWAR
FIG. I

VACUUM VALVE

TOP COVER

CASE

NITROGEN CAN

RADIATION SHIELD

HELIUM CAN

COLD WORK SURFACE

WINDOW HOLDER

OPTICAL AXIS

12.50

1.75

1.062

7.00

ELECTRICAL
CONNECTOR

CAP

DETECTOR
HOLDER

"A"

"B"
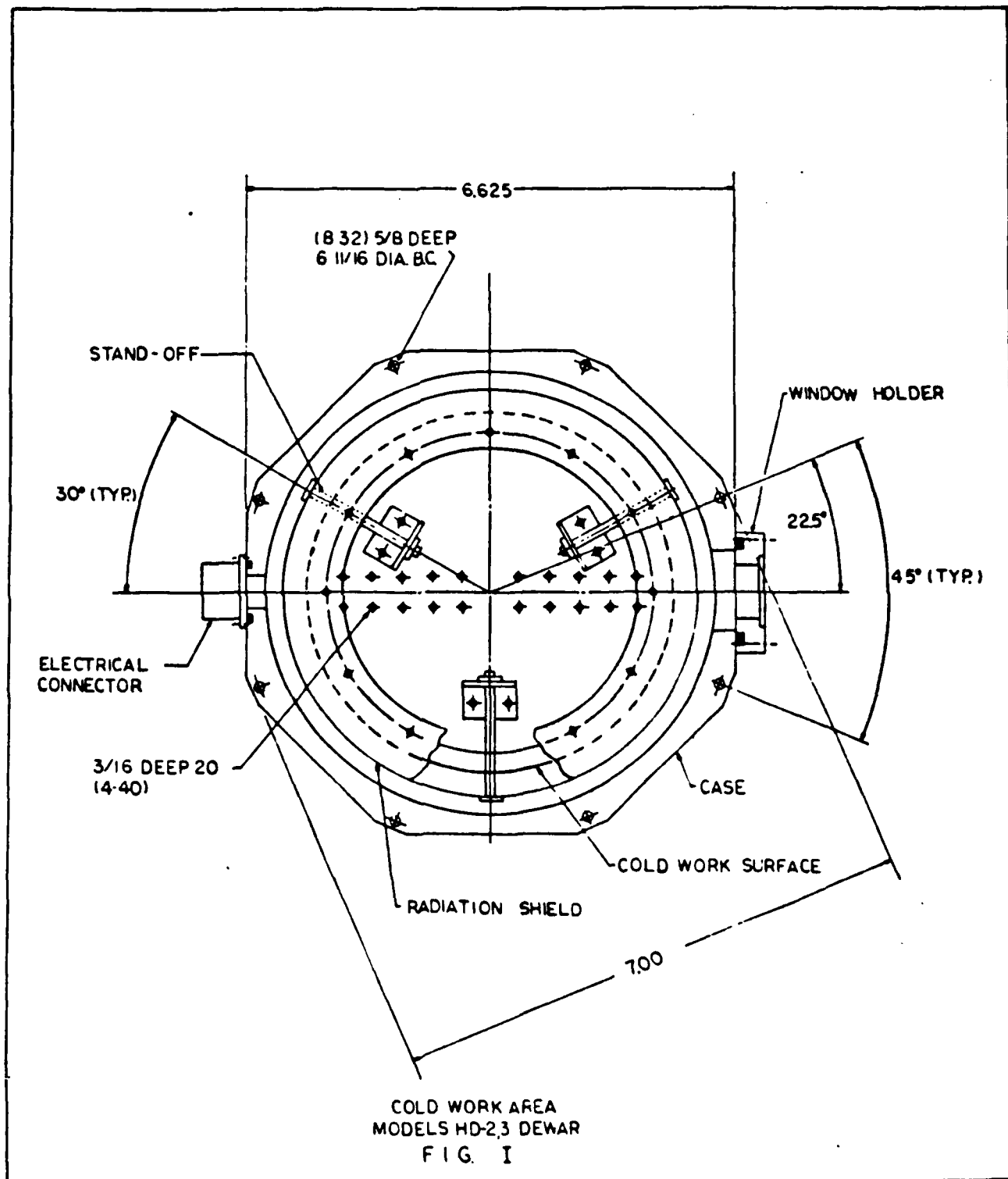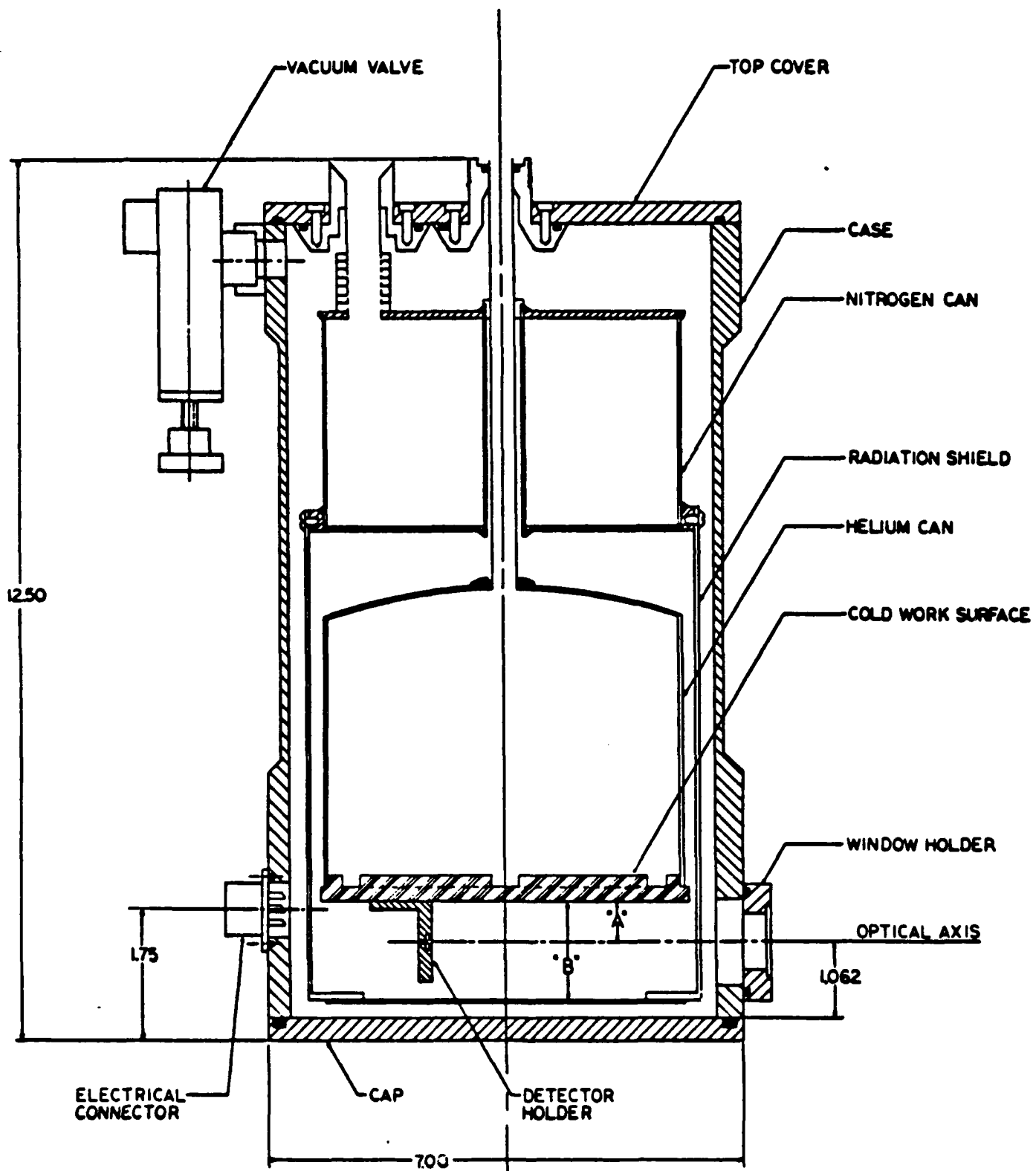
FULL SCALE

MODEL HD-3
F I G Ⅲ

RUBBER STOPPER

BRASS TUBE. (HOSE TO VACUUM PUMP)

KNURLED NUT. (THREADS TO DEWAR HELIUM FILL CONNECTOR)

BRASS BODY (SEALS TO TEFLON GASKET)

COPPER

1/8" DIA. STAINLESS TUBE

* DIMENSION CUSTOMIZED TO DEWAR
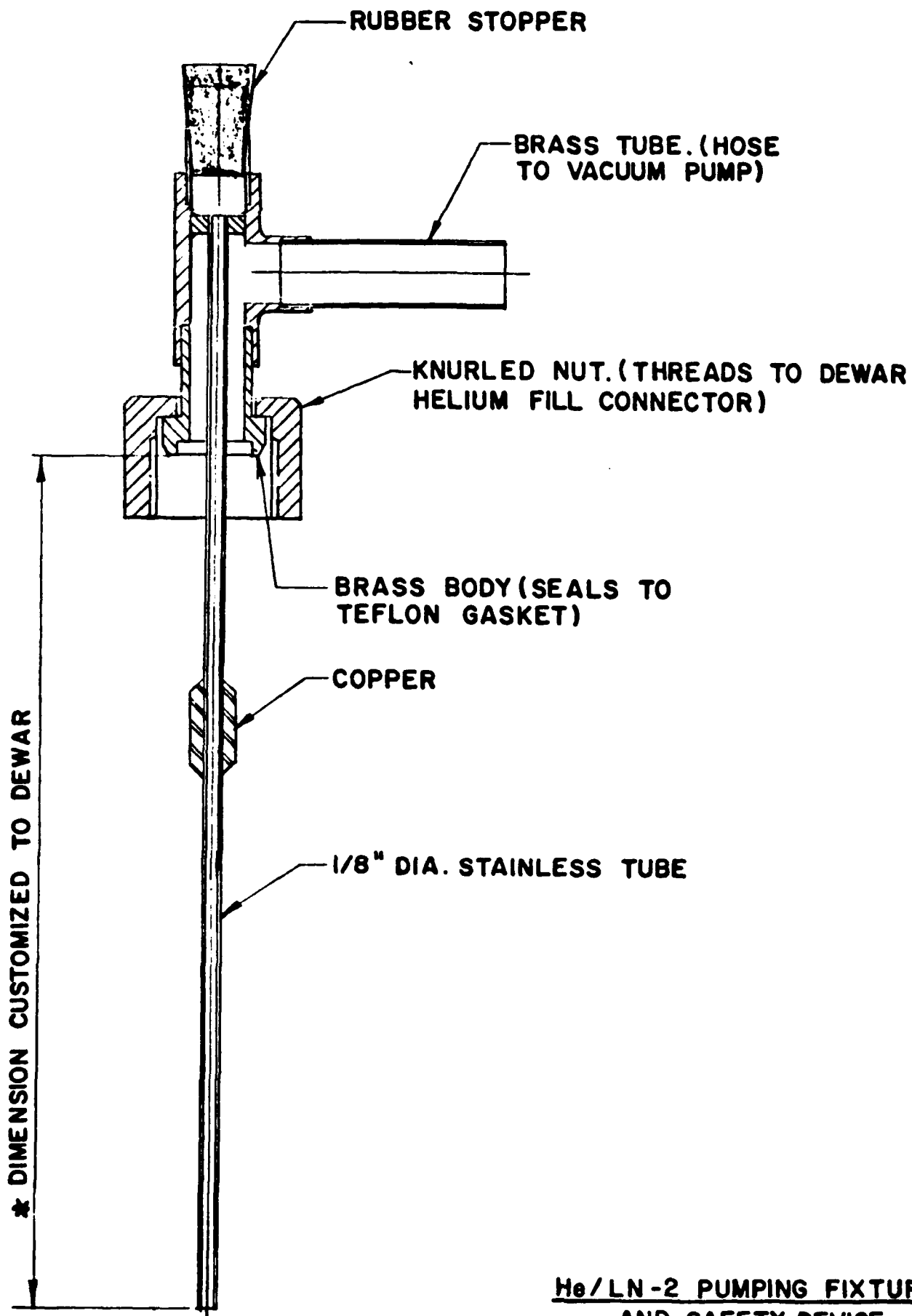
He/LN-2 PUMPING FIXTURE
AND SAFETY DEVICE

SCALE: 1:1

BRASS TUBE.(HOSE TO
he GAS, TO EVACUATE
LN2

COPPER TUBE.(HOSE
TO N2 SUPPLY

BRASS BODY. (SEALS TO
TEFLON GASKET)

1/4" STAINLESS TUBE

✳ DIMENSION CUSTOMIZED TO DEWAR

SCALE: 1:1

NITROGEN FILL TUBE

INFRARED LABORATORIES, INC.
1808 EAST 17th STREET 85719
TUCSON, ARIZONA
U.S.A.

CROSS SECTION VIEW OF HELIUM VESSEL COPPER BOTTOM PLATE (COLD WORK SURFACE)
SHOWING COPPER THICKNESSES.

HOLES MAY BE DRILLED TO $\frac{1}{4}$" DEPTH AT ANY LOCATION EXCEPT IN THE CENTER, WHERE
DEPTH SHOULD BE LIMITED TO 3/16".
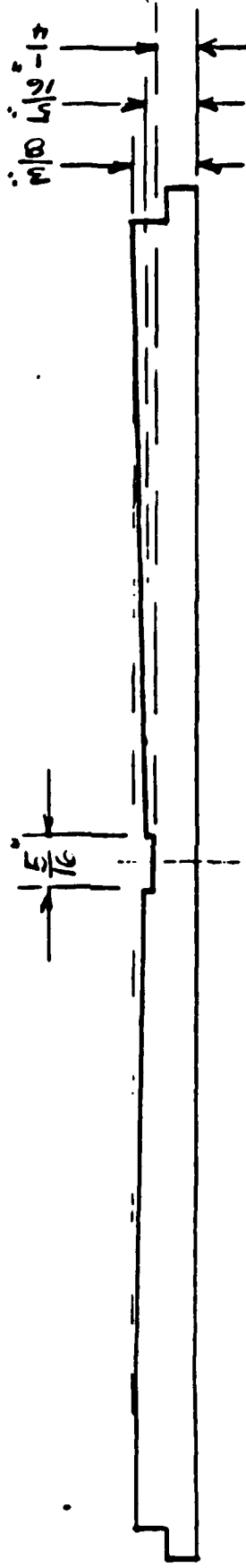
APPLICABLE TO ALL INFRARED LABORATORIES, INC. DEWARS, INCLUDING MODELS ND-1,
ND-2, HD-2, HD-2(8), HD-3, HD-3L, AND HD-3(8), BEGINNING WITH SERIAL NO. 470.

INFRARED LABORATORIES, INC.

1806 EAST 17TH STREET
TUCSON, ARIZONA 85719
PHONE: (602) 622-7074
TLX 364412 INTR

GUARANTEE

GENERAL:

All equipment sold by Infrared Laboratories, Inc. is guaranteed for a period of one year against failure caused by defective materials or workmanship. Defective parts will be repaired or replaced upon return to our Laboratory. Infrared Laboratories, Inc., assumes no liability for the loss of life or property caused by the use or misuse of our products.

DETECTOR:

Each detector is supplied with a set of test data describing its performance. It is strongly recommended that the user repeat the test procedures as described in our operator's manual as soon as possible upon receipt of the detector. Infrared Laboratories, Inc. guarantees that the detector will exhibit the same level of performance described by the test data as furnished. If the detector fails to exhibit this level of performance upon its return to our Laboratory within one year, and if the failure is not caused by misuse or mishandling after delivery, then it will be replaced at no cost.

ARNOLD W. DAVIDSON, MANAGER

5.3 Research Conducted at the Lunar and Planetary Institute.

Summary Report of Research Conducted at the

Lunar and Planetary Institute

By Karl J. Vogler
Visiting Graduate Fellow

May 31,1988 to July 31,1988

During my appointment as a Visiting Graduate Fellow at the Lunar and Planetarty Institute (June 1, 1988 to July 31, 1988) I continued research on the project I am working on with Dr. Paul Johnson (Univ. of Wyoming) and Dr. Richard Shorthill (Univ. of Utah) involving infrared observations of the Moon and asteroids in an effort to improve the calibration base for ground-based and spacecraft infrared detector systems. The thermophysical properties of solid-surfaced planetary bodies are also being studied through the use of thermal computer models. The models are currently being tested with lunar data available in the literature. Measurements of the Moon made with our detector system will also be used to constrain the models. The purpose of my visit to LPI was to become familiar with the known surface morphology and composistion of the Moon and asteroids so that our thermal computer models can be made more realistic.

Improving and modifying the thermal computer models algorithms through use of the Library and Computer Centers was given priority during my visit. Improving our lunar observing program and developing an asteroid observing program were given a secondary role. Relevant information on lunar crater morphology, albedo variations, surface composistion and physical properites, and larger scale topography was obtained through a literature search and an examination of the Apollo Panoramic and Metric Photography. Secondly, our lunar observing program has been improved by the addition of Lunar Topographic Orthophotomaps and

Apollo Metric Photography of selected regions. Knowledge of topography on this scale will aid the interpretation of high resolution lunar images taken with our detector system. Finally, a literature search on asteroids and their surface properties was conducted so that an observing program can be developed.

As part of my investigation of lunar crater morphology, a project was initiated with the intention of obtaining contour information for small craters with diameters between .5 km and 5 km. Photographs of four highland and four mare craters were chosen from Apollo Metric and Panoramic Photography. In addition to acquiring contour information, it is desirable to compare small highland and mare craters since data for fresh lunar craters indicate that craters on the mare are up to 10% deeper than similar craters in the highlands (Wood and Anderson, 1978). Copies of these photographs were obtained so that vertical measurements could be made using the Bausch and Lomb Stereo Zoom Transfer Scope available in the Planetray Image Center.The Apollo Panoramic photographs contain more distortions than can be accounted for by the Vertical Measurement System on the Zoom Transfer Scope and could not be used. Vertical measurements were made for two craters using the Apollo Metric Photography. The errors associated with these measurements are sufficiently large that no improvement can be made on contour information available on the Lunar Topographic Orthophotomaps, hence no further measurements were made. Topographic maps with contour intervals of 50 m can be prepared from the Apollo Metric Photographs, while

Panoramic Phototgraphs can yield topographic maps with 5 m contours (Wu and Moore, 1980).

There are a few special scale lunar maps with contour intervals of 10 to 20 m at scales between 1:10,000 and 1:50,000, i.e. the Lunar Topophotomaps. An examination of these maps revealed about six craters which are similar to the original craters chosen. A minimum of eight profiles for each crater are being derived from the contour information so that a rigorous analysis of their geometric shape can be made.

In addition, I spoke with Dr. Wendell Mendell (NASA JSC) about infrared instrumentation, potential calibration problems that might arise in making lunar measurements, and how such problems might be corrected. I presented a seminar entitled "Modeling and Measuring the Non-Grey-Body Thermal Emission of Solid-surfaced Planetary Bodies" on July 27, 1988 in the Berkner Room at LPI. I also attended the tours, films, and seminars required of the Summer Interns, as well as the weekly LPI seminars.

References:

Wood, C.A. and Andersson, L. (1978) Proc. 9th Lunar Planet. Sci. Conf. "New Morphometric Data For Fresh Lunar Craters" p3669-3689.

Wu, S.S.C. and Moore, J. (1980) "Experimental Photogrammetry of Lunar Images" U.S.G.S. Professional Paper 1046-D

5.4 Modeling the Non-Gray-Body Thermal Emission from the Full Moon.

MODELING THE NON-GREY-BODY
THERMAL EMISSION FROM THE FULL MOON

Karl J. Vogler
Paul E. Johnson
Department of Physics and Astronomy
University of Wyoming
Laramie, WY 82071
(307) 766-6150

Richard W. Shorthill
Department of Mechanical and Industrial Engineering
University of Utah
Salt Lake City, Utah 84112
(801)581-8623

MODELING THE NON-GREY-BODY THERMAL EMISSION FROM THE FULL MOON

Abstract

In an attempt to understand the non-grey-body brightness temperature spectra of the Moon and Galilean satellites we have developed a series of thermophysical computer models of solid-surfaced planetary bodies. Surface roughness is modeled as paraboloidal holes (craters) of a specified depth to diameter ratio. Multiple scattering of incident solar radiation and the re-emitted thermal radiation inside craters are included. A directional emissivity derived from Kirchoff's law and the Fresnel equations for reflection from a dielectric surface is also included. The model agrees well with published limb-scans for the Moon. It is concluded that negative surface relief and the Fresnel equations are required to explain deviation of lunar thermal emission from that expected from a smooth, Lambert surface. This may allow for the quantitative measurement of surface roughness under some circumstances.

Introduction

We are studying thermal emission from solid-surfaced planets with the goal of improving the calibration base for ground-based and spacecraft infrared detector systems in the mid- and far-infrared ($\sim$ 5 to 100 μm). In addition to telescopic observations, we are developing a series of thermophysical computer models to tie together infrared photometry of standard stars, the moon (an asteroid prototype), and asteroids with potential for use as infrared calibration objects.

The need for accurate long wavelength calibration sources for space-based infrared detector systems exists since current celestial photometric standards do not appear to be viable in the region of 100 μm, as illustrated by the IRAS experience (Beichman et al. 1986). The method for calibration of IRAS was to use standard stars and stellar models for the 12, 25, and 60 μm bands, which are ultimately tied to the absolute flux calibration of Vega and α Tau (Beichman et al., 1986). This method is unsuitable near 100 μm due to the scarcity of bright stellar sources and source confusion in the galactic plane. The 12μm IRAS band was calibrated using stellar measurements. The 12μm calibration measurements were then extrapolated to the 25μm and 60μm bands using stellar models normalized to observations of the sun. Extrapolation of the calibration from 60μm to 100μm is based on observations and model calculations of asteroids whose absolute flux at 60μm is tied to the 60μm stellar calibration. This particular group of asteroids is comprised of the larger asteroids which are nearly spherical in shape and have low albedos.

Asteroids are reasonable choices for infrared calibration standards for the following reasons. First, asteroid thermal emission spectra have no significant emission or absorption features. Hansen (1976) obtained thermal emission spectra for 24 asteroids and the Galilean Satellites between 8 and 23 μm which exhibit this effect. Second, asteroids are bright in the infrared because the blackbody curves corresponding to their surface temperatures peak at infrared wavelengths. Third, one can, in principal, model asteroid thermal emission spectra as a function of illumination/viewing geometry. Finally, asteroids are

1

very nearly point sources.

The difficulty in using asteroids for calibration standards arises in the non-grey-body emission spectra caused by a distribution of temperatures over an asteroid's surface. The non-grey-body nature of asteroid emission spectra is best illustrated by the strong decrease of infrared brightness temperature with increasing wavelength reported in the literature. Matson et al. (1983) have reported a marked decrease of brightness temperature with increasing wavelength for the Galilean satellites confirming earlier reports by Hansen (1976). The observed decrease of brightness temperature between 10μm and 20μm is steeper than can be explained by a simple disk or smooth sphere model. Matson et al. (1983) have also shown that photometric calibration errors and wavelength dependent emissivity will not explain the observations. Murcray's (1965) 6 to 12 μm data for the Moon shows a negative slope in the brightness temperature spectrum. The same effect is also observed in the Voyager IRIS 4 to 55 μm data for the Gallilean satellites. Spencer (1987) rules out calibration errors and wavelength dependent emissivity as causes of the slopes in the IRIS spectra. Spencer (1987) also states that temperature variations across the instrument's field of view due to global temperature gradients make only a small contribution to the spectral slope. Thus having ruled out these possible causes of the observed behavior of the infrared brightness temperature spectrum, we are left with local temperature contrasts as the probable cause.

Measurements by Pettit and Nicholson (1930) first revealed the non-Lambertian emission of the lunar surface at full moon. Their temperature measurements along the lunar equator varied as $\cos^{1/6}\theta$ instead of $\cos^{1/4}\theta$ which is expected for a Lambertian surface. (θ is the angular distance from the subsolar point). Deviations from diffuse emission were explained by a general surface roughness. Saari and Shorthill (1972) using their measured isophotic and isothermal contours of the full moon (Shorthill and Saari 1965; Saari and Shorthill 1966a,b) characterized the lunar brightness temperature by the least squares fit of $T(K) = 324.2 + 72.6 \cos\theta$. In addition, the directional infrared emission from the full

2

moon was determined as a function of observer elevation and azimuth angles for three sun elevation angles. It was concluded that the brightness temperature of the sunlit lunar surface is influenced primarily by an average surface roughness and albedo variations (Saari and Shorthill 1972).

Local Temperature Contrasts

A local temperature contrast is defined as any variation in surface temperature on a scale smaller than the field of view at the detector. For example, a detector with a spatial resolution corresponding to a single lunar crater, 10 km in diameter, would encounter local temperature contrasts with scales of up to a few kilometers. The same system detecting an asteroid would measure local temperature contrasts on scales up to tens of kilometers as well as contrasts due to global temperature distributions. The following discussion serves to illustrate the behavior of a generic local temperature contrast.

Consider a diffuse, grey, surface of total area A which has a checkerboard temperature distribution of temperatures T_1 and T_2, each occupying one half of the total area. Each smaller area of constant temperature T_i radiates a monochromatic flux given by

$$F_\lambda(T_i) = A_i \pi \epsilon_i B_\lambda(T_i), \tag{1}$$

where $B_\lambda(T_i)$ is the monochromatic intensity given by the Planck function, A_i is the area over which T_i is constant and ϵ_i is the grey-body emissivity. If our instrument has a field of view which covers only one of the regions of constant temperature we would measure a flux $F_\lambda(T_i)$ which would result in a flat brightness temperature spectrum since we would not observe any local temperature variations. However, if our instrument has a field of view that covers all of the checkerboard temperature distribution we would detect

$$F_\lambda(T)_{total} = \pi\left(\frac{A}{2}\epsilon_1 B_\lambda(T_1) + \frac{A}{2}\epsilon_2 B_\lambda(T_2)\right). \tag{2}$$

3

Then using $F_\lambda(T)_{total}$ and the Planck function we can solve for the overall brightness temperature, T_B. Results of these calculations with A=1, $\epsilon_1=\epsilon_2=0.95$, $T_1=340$ K and $T_2=400$ K are shown in Figure 1. For purposes of comparison the same calculations have been done for the temperature distribution in Figure 1 with $T_{avg} = 370$ K and $\epsilon=0.95$. Two obvious results are the difference in brightness temperature and the marked difference in curvature between the two spectra. These differences are a result of the Planck function being a highly non-linear function of temperature at short wavelengths and an approximately linear function at long wavelengths. Therefore the two curves deviate greatly at short wavelengths and approach each other asymptotically at long wavelengths. More power will be detected from an area with a distribution of temperatures than with the mean of the distribution because the total power emitted is proportional to the temperature of the surface to the fourth power. By the same reasoning a large temperature contrast over an area will result in more emitted power than a small temperature contrast.

There are a number of mechanisms capable of producing local temperature contrasts on solid-surfaced planetary bodies, a few of which are (1) albedo variations, (2) thermal inertia variations and (3) macroscopic surface roughness. Albedo variations can cause local temperature contrasts since higher albedo surfaces will in general be cooler than lower albedo surfaces. In addition, high thermal inertia material exhibits smaller diurnal changes in surface temperature than materials of low thermal inertia. Hence, high thermal inertia material will be cooler during the day and warmer at night than a lower thermal inertia material. Thus a mixed distribution of high and low thermal inertia material would result in local temperature contrasts. Surface roughness on a macroscopic scale will cause local temperature contrasts as a direct result of variations in illumination of the surface. The term macroscopic implies that the scale of roughness is larger than wavelengths under consideration and large enough so that temperature contrasts will not be removed by conduction, (i.e. larger than a few centimeters)(Spencer 1987). Flat surfaces tilted toward the sun will be warmer than those tilted away. More obviously shadowed regions are cooler

4

than those in full sunlight. In addition, features with negative relief, (holes, crevices, etc.) will see scattered incident radiation and re-emitted thermal radiation from other points inside the same depression and thus will appear hotter than their surroundings. All of these effects will occur in a real planetary surface to some degree and are amenable to thermal modeling. We will model thermal emission from the full moon assuming negative surface relief is of primary importance on a small (< 10km) scale. A summary of our models is shown in Table 1.

Thermal Models

In modeling thermal emission from solid-surfaced planetary bodies it is desirable to be able to study surface properties as a function of position on the sphere as well as the disc-integrated properties. In order to model the thermal emission from the integrated disc of a solid-surfaced body, one needs to determine the temperature distribution over the surface of a rotating body with arbitrary pole orientation. Our initial model, Model A, (Johnson et al. 1983) is a thermophysical model of the subsurface which calculates the surface temperature on a grid in planetocentric latitude and longitude, sufficiently fine to obtain 1% precision in the modeled flux. For these computations a one dimensional heat flow equation is solved simultaneously for the upper layers of the subsurface (within 5 thermal skin depths of the surface) using the same method as Cuzzi (1973) and Landau (1975). Input parameters include: pole orientation, heliocentric distance, rotation period, bolometric Bond albedo and emissivity, anisotropy of emission, wavelength, and thermal inertia ($(kpc)^{1/2}$ where k = thermal conductivity, ρ = density, c = specific heat capacity). Geometrical effects caused by the orbital inclination of the body are accounted for explicitly. Photometric effects due to macroscopic surface roughness were not included in this model.

In general, the emissivity of a planetary surface is anisotropic. Specifically, macroscopic surface roughness creates illumination conditions which result in enhanced emission at the limbs relative to the center for the full moon as compared to a smooth Lambert

5

Sphere (Saari and Shorthill 1972). In order to begin modeling the effects of surface rough-ness, Model B was created by adding surface roughness to Model A in the form of a statistical mixture of low albedo spots on a higher albedo surface. The low albedo spots mimic depressions in that they absorb more radiation than the surrounding surface and thus are at a higher temperature. We choose a low albedo of 0.01 with 60% coverage, a high albedo of 0.18 with 40% coverage and input parameters corresponding to the full moon to obtain a disc-integrated brightness temperature spectrum and test the assump-tion. The spectrum is compared to Murcray's (1965) 6-12 micron data in Fig. 2. The brightness temperatures are comparable but the theoretical slope (-9.1 ± 0.3 K/μm) is a factor of three greater than the observed slope of -3.0±0.1 K/μm. The results suggests that a rigorous treatment of the surface roughness is in order.

Model C, treats macroscopic surface roughness as paraboloidal holes (craters) of spec-ified depth to diameter ratio, albedo, emissivity, and illumination/viewing geometry. The geometry is the same as used by Hämeen-Antilla et al. (1965). With this geometry, one can calculate the illumination conditions for each point inside the crater, and the emission characteristics seen by the observer. Inside the paraboloid any surface element will see scattered incident radiation from other elements, determined by the surface bidirectional reflectance, as well as re-emitted thermal radiation from other point in the depression. Our analysis of the scattered and re-emitted radiation inside the crater is similar to that used by Spencer (1987) and Bevens and Edwards (1965). In addition, similar types of analyses are also found in standard textbooks on radiative heat transfer (e.g. *Radiative Transfer and Interactions with Conduction and Convection*, by Ozisik). For this analysis the crater is divided into N surface elements (N $\geq$ 180) over which the following assumptions are made: 1) each surface element is grey and diffuse, 2) temperature, reflectance, emissivity, and incident and emitted flux are constant over each element, 3) thermal inertia is assumed to be zero so that for each element the emitted radiation is equal to the incident radiation (direct, scattered and re-emitted). We assume zero thermal inertia due to the small relative

size of the lunar thermal inertia and the slow rotation rate of the moon (Saari and Short-hill, 1966c). Model C can also treat the emissivity as a directional emissivity as calculated from the Fresnel equations for reflection and Kirchoff's law. From these conditions a set of matrix equations is derived from which the temperature of each element is calculated. Once the temperature of the crater elements is known the thermal emission from the crater is calculated. This model produces a temperature map of the crater surface and a corresponding brightness temperature spectrum for a flat surface saturated with the specified craters. Figure 3 shows 10μm brightness temperature profiles for a flat surface saturated with the specified depression as a function of depth to diameter ratio and angle θ, where θ is equal to both the illumination angle and emission angle with the phase angle equal to zero degrees ($i = \epsilon = \theta, \alpha = 0°$). In general we note that the brightness temperature of a rough surface increases with increasing depth to diameter ratio and that as θ approaches 90° the brightness temperature is enhanced relative to a flat surface (h/D = 0.0) with the same illumination/viewing conditions.

Near the subsolar point we see that the brightness temperature first decreases with increasing depth to diameter ratio, and then increases when the depth to diameter ratio is increased further. This results from competing effects caused by macroscopic surface roughness. The distribution of slopes for a depression near the subsolar point acts to decrease the solar insolation relative to a flat surface for a given surface element. In addition, when viewing a depression near the subsolar point an observer sees less than maximum emission from a given surface element since the emission angles are greater than zero degrees. Countering these effects is an increase in surface temperature due to scattered incident and re-emitted thermal radiation from other points inside the depression. Surface temperature maps calculated by the model show that the mean surface temperature inside the depression increases with increasing depth to diameter ratio. Thus when depressions near the subsolar point are integrated over to produce the brightness temperature profiles in Figure 3, the surface temperature enhancement due to scattered incident and

7

re-emitted thermal radiation does not counter the reduced emission and solar insolation caused by the distribution of slopes in depressions of small depth to diameter ratio (0.0 $<$ h/D $\lesssim$ 0.3). This is about a 4K effect in the 10μm brightness temperature. For depth to diameter ratios greater than 0.3 the surface temperature enhancement dominates and brightness temperature increases with increasing depth to diameter ratio. We note that the subsolar point brightness temperature (for large enough depth to diameter ratio) is enhanced over that of a blackbody in radiative equilibrium with the solar constant. This result is consistent with results obtained by Mendell (1976) using the Apollo 17 Infrared Scanning Radiometer (ISR). Measurements with the ISR became saturated within 20° of the subsolar point. The ISR saturation temperature is approximately 401K from which a subsolar point temperature of 406K can be inferred (Mendell, 1976).

Figure 3 also shows that the mean slope of the 10μm brightness temperature profiles decrease with increasing depth to diameter ratio and is characterized by "flat" regions. As the depth to diameter ratio of a paraboloidal depression is increased the sides become steeper and the depression becomes deeper. Thus for shallow depression we expect that shadows will form only for large incidence angles, whereas a deeper depression will have shadows at smaller incidence angles. In addition as the illumination angle is increased, the sides of the depression become more normal to the incident radiation relative to a flat surface at the same illumination angle. If we observe the depression at the illumination angle ($i = \epsilon = 0, \alpha = 0°$ as before) shadows are obscured by the edge of the depression, thus only the illuminated portion of the depression is observed. Near the subsolar point where the entire crater is illuminated and visible, the brightness temperature profiles exhibit a $\cos^{\frac{1}{4}}\theta$ dependence. The "flat" regions form at values of θ where shadows form and are unobservable, the illuminated of the depression are more normal to the observer, and most of the depression is observable. As θ is increased further less of the depression interior is visible and the regions that are become less normal to the observer. Thus we expect the "flat" regions to move to smaller values of θ as the depth to diameter ratio is increased.

This has the effect of decreasing the mean slope of the brightness temperature profile. In addition, the finite size of the depression elements introduces small oscillations in the brightness temperature profile. The size of these oscillations decrease as the number of crater elements is increased.

Having obtained results for a single crater under a variety of conditions, Model C was modified so as to randomly distribute craters of a single depth to diameter ratio over the surface of a smooth grey sphere with a weighting representing the amount of surface covered with craters. This results in Model D. The emissivity of a smooth sphere is anisotropic as a result of the Fresnel equations for reflection from a dielectric surface and Kirchoff's law as shown in Heiles and Drake (1963). Heiles and Drake successfully used this to model the anisotropy of 21cm emission from the moon. This algorithm is summarized below.

The power reflection coefficients for a plane electromagnetic wave incident at angle ϕ on a dielectric surface are:

$$ R_{\parallel} = \left(\frac{\epsilon\cos\phi - (\epsilon - \sin^2\phi)^{1/2}}{\epsilon\cos\phi + (\epsilon - \sin^2\phi)^{1/2}} \right)^2 \quad R_{\perp} = \left(\frac{\cos\phi - (\epsilon - \sin^2\phi)^{1/2}}{\cos\phi + (\epsilon - \sin^2\phi)^{1/2}} \right)^2 \tag{3} $$

where ϵ is the dielectric constant, ϕ is the angle between the surface normal and the direction of propagation of the incident wave, $R_{\parallel}$ is for linear polarization with the electric vector parallel to the plane of incidence and $R_{\perp}$ is for the orthogonal polarization. Using Kirchoff's law for the smooth sphere allows us to write:

$$ E_{\parallel}(\phi) = 1 - R_{\parallel}(\phi) \qquad E_{\perp}(\phi) = 1 - R_{\perp}(\phi) \tag{4} $$

It is assumed that the surface emits equal amounts of energy in both polarizations, hence we write:

$$ E_{total}(\epsilon, \phi) = \frac{1}{2}(E_{\perp}(\epsilon, \phi) + E_{\parallel}(\epsilon, \phi)) \tag{5} $$

where $E_{total}(\epsilon, \phi)$ is the directional emissivity used on the dielectric sphere in Model D.

This same directional emissivity has been added to the calculations inside the crater in Model D, resulting in Model E.

There are four basic model parameters in Model E, the depth to diameter ratio, the reflectance (Bond albedo, hemispherical reflectance, and bidirectional reflectance), the dielectric constant and the percentage of rough surface, which affect the model differently. The depth to diameter ratio characterizes the roughness of a given surface and is responsible for local temperature contrasts in the models. The effect of increasing the depth to diameter ratio is to raise the mean surface and brightness temperatures of a rough surface and to flatten the slope of the brightness temperature as a function of angle θ ($i=\epsilon=\theta$), where θ is the angular distance from the center of the sphere. Figure 3 illustrates this effect most clearly. The details were discussed previously in the explanation of Figure 3.

The reflectance parameters used in Model E are a bidirectional reflectance and a hemispherical reflectance (or albedo), both of which are related to the Bond albedo. Values for the reflectances are derived from measured values of the Bond albedo assuming nearly isotropic scattering and using the results of Hapke (1981). The hemispherical albedo is used to determine the solar insolation for any given surface element inside or outside of a depression. The bidirectional reflectance describes the reflections between surface elements in a depression as per Bevens and Edwards (1965). Increasing the value of the Bond albedo, increases these reflectances which decreases the surface and brightness temperatures as one expects provided other parameters are held constant.

The dielectric constant is used to calculate the emissivities as described previously. Since the Fresnel emissivity decreases with dielectric constant, the effect of viewing a surface at a given temperature and using these emissivities is a lower brightness temperature and an enhanced ratio of limb emission to emission from the center of the disk. In addition, decreasing the emissivity (E) increases the surface temperature as $E^{-0.25}$, as expected from simple calculations.

Increasing the ratio of rough to smooth surface results in an increasing brightness

10

temperature over the entire disc. This creates larger local temperature contrasts which increases the slope of the disc integrated brightness temperature spectrum. Having discussed the general behavior of the model parameters we can now look at specific model results for the full moon.

Discussion of Results

Both Models D and E use the illumination/viewing conditions for the full moon ($i=\epsilon=\theta$, $\alpha=0°$) so that the model calculations may be compared to data available in the literature, specifically the 10μm brightness temperature vs. θ from Saari and Shorthill (1972), and the disc-integrated data from Murcray (1965).

The data from Saari and Shorthill (1972), shown for comparison in Figures 4 and 5, are for a phase angle of -2°16', just prior to full moon. The data is the measured 10μm brightness temperature taken in a direction north from the center of the lunar disc. Resolution is on the order of 10 arc seconds. The scan contains both highlands and maria, the names of associated features and their extent along the scan are presented in Table 2. The apparent irregularities in the data are due to albedo differences between the highlands and the maria. The reflectance variations can introduce a 2% difference in the brightness temperatures between the highlands and maria, which corresponds to an 8 K effect at 400 K (Montgomery et al. 1966). The data in question are derived from earlier measurements by Saari and Shorthill (1966a) and (1966b). The errors in the brightness temperatures are less than ± 10 K and are probably closer to ± 5 K (Montgomery et al. 1966). Differences in brightness temperature along the scan are not well correlated with reflectance variations caused by changing from highlands to maria along the scan. This may be due to mixed highland and maria features within the beam which cannot be accounted for by looking at large scale features.

Murcray's (1965) 6-12 μm data were taken near the full moon during the September and October 1964 lunations and are whole disc measurements. Since no error bars are given

11

in the data, we assume that the measurements are approximately as good as those of Saari and Shorthill (1966a) and (1966b) since similar instrumentation is used. Hence, we assume that the error bars on the brightness temperatures given by Murcray's data are less than ± 10 K and are probably closer to ± 5 K. Murcray's data appears in Figure 6.

Figure 4 depicts upper and lower depth to diameter solutions which bracket the observed 10μm brightness temperatures. The depth to diameter ratio of the upper curve is 0.51 while that of the lower curve is 0.46. The two solutions predict subsolar point brightness temperatures between 400K and 410K which is consistent *Consistant ?.* with previously discussed results. The differences between the two solutions are smaller near the limb which is mostly due to seeing only the illuminated walls of the depressions. The discussion of the "flat" regions in the brightness temperature profiles from Figure 3 also applies here.

Figure 5 shows model solutions bracketing the observed 10μm brightness temperatures for cases of high and low reflectances. The depth to diameter ratio used is an average of the values used in Figure 4. The reflectances used in the lower limit solution were derived from a Bond albedo of 0.06 using results from Hapke (1981) and assuming nearly isotropic scattering. Those used in the upper limit solution were derived from a Bond albedo of 0.15. The lower limit parameters were chosen to depict a "dark" mare while the upper limit parameters mimic a "bright" highland region. There is some correlation between the model calculations and the observed 10μm brightness temperatures. For example, the lower limit solution agrees well with the mare region between $\theta = 25°$ and $\theta = 40°$. Similarly the upper limit solution agrees well with the highland region from $\theta = 65°$ to $\theta = 80°$. As noted earlier there are mixed highland and mare regions in the data.

Figure 6 contains Murcray's (1965) data and disk integrated brightness temperature spectra for the solutions in Figures 4 and 5. The Model E calculations have slopes of -3.8 ± 0.2 K/μm to -3.6± 0.2 K/μm which agree relatively well with the slope of -3.0 ± 0.1 K/μm for Murcray's data. These slopes are good only in the region shown. The upper limit depth to diameter solution and the lower limit reflectance solution just fit inside the

assumed ± 10K error bars.

Heliocentric Distance: Model Fits for Callisto

The solar constant scales as $\frac{1}{R^2}$ where R is the heliocentric distance in AU. Hence at larger distances the solar insolation will be diminished resulting in lower surface temperatures which increases emission at longer wavelengths. This implies less steep brightness temperature spectrum slopes (Hansen, 1977). As a further check on the model the heliocentric distance was varied so that we could compare an averaged brightness temperature spectrum of Callisto from the Voyager 1 IRIS data (Spencer, 1987 p.23) to a disc-integrated brightness temperature spectrum calculated by Model E. The input parameters used were heliocentric distance of 5.34 AU, depth to diameter ratio of 0.15, a bidirectional reflectance of 0.073 and a hemispherical reflectance of 0.182 corresponding to a $\overset{B}{\text{bond}}$ albedo of 0.22, a dielectric constant of 3.0 and a weighting of 25% smooth surface and 75% rough. The dielectric constant was chosen to approximate the dirty water ice composition of Callisto's surface (Spencer 1986, pp. 1-8). The observed slope over the 8 to 20μm range is -0.80±0.1 K/μm which is compared to a calculated slope of -0.76±0.1 K/μm. The wavelength range was chosen so that fitting a straight line to the data and model calculations is reasonable. These slopes are not valid outside of the 8 to 20μm range. The measured 10μm brightness temperature is $\overset{150.0}{\cancel{150}}$ K whereas the calculated 10μm brightness temperature is 151.7 K. No attempt was made to adjust parameters for a better fit. This indicates that the model adequately accounts for the observed decrease in slope of the brightness temperature spectrum with increasing heliocentric distance.

Conclusions and Future Work

The current level of our thermal models contains effects due to macroscopic surface roughness in the form of craters and an anisotropic emissivity derived from the Fresnel equations and Kirchoff's law. By including these effects, we are able to calculate ap-

proximate fits to the 10μm brightness temperature versus θ data for the full moon, the disc-integrated brightness temperature for the full moon and the disc-integrated brightness temperature spectrum of Callisto. The crater depth to diameter ratio and the percentage of rough surface are the only free parameters. The dielectric constant and emissivity and the albedo are constrained by independent measurements in the literature. The approximate fits to the data are not necessarily unique.

Our current models are limited to the sunlit lunar surface since we have assumed zero thermal inertia. Hence, a necessary improvement will be to incorporate thermal inertia effects into the models. In addition, it may be useful to include the effects due to large scale albedo variations like those on the moon. Secondly, a careful study of lunar topography and crater morphology will provide additional constraints on the depth to diameter ratio and the percentage of rough surface. Thirdly, we have assumed no roughness on a scale much smaller than the crater size. However, the depth to diameter ratio of small lunar craters ($\sim$ 10 km diameters) is approximately 0.2. The larger value of the depth to diameter ratio in our models would imply that surface roughness on a smaller scale (much less than 1 km, or 1 m perhaps?) is responsible for the observed temperature enhancements. Hence a distribution of depth to diameter ratios in the model is desirable.

Acknowledgements

REFERENCES

Bastin, J.A. and Gough, D.O. (1969) "Intermediate Scale Lunar Roughness," **Icarus, 11,** 289-319.

Beichman, C.A., Neugebauer, G., Habing, H.J., Clegg, P.E., Chester, T.J. (1986) "Flux Reconstruction and Calibration," **IRAS Catalog And Atlases Explanatory Supplement, JPL D-1855,** VI:1- 31, Pasadena.

Bevens, J.T. and Edwards, D.K. (1965) "Radiation Exchange in an Enclosure with Directional Wall Properties," **J. Heat Transfer, 87C,** 388-396.

Buratti, B.J. and Veverka, J. (1985) "Photometry of Rough Planetary Surfaces: The Role of Multiple Scattering," **Icarus, 64,** 320-328.

Burden, R.L. and Faires, J.D. (1985) **Numerical Analysis,** Prindle, Weber and Schmidt, Boston, 676.

Cuzzi, J.M. (1973) "The Subsurface Nature of Mercury and Mars from Thermal Microwave Emission," **Ph.D. Thesis,** California Institute of Technology.

Hämeen-Anttila, K.A., Laakso, P. and Lumme, K. (1965) "The Shadow Effect in the Phase Curves in Lunar Type Surfaces," **Ann. Acad. Sci. Fenn. Ser. A., 172,** 3-16.

Hansen, O.L. (1976) "Thermal Emission Spectra of 24 Asteroids and the Gallilean Satellites," **Icarus, 27,** 463-471.

Hansen, O.L. (1977) "An Explication of the Radiometric Method for Size and Albedo Determination," **Icarus 31,** 456-482.

Hapke, B. (1981) "Bidirectional Reflectance Spectroscopy 1. Theory," **J. Geophys. Res., 86,** 3039-3054.

Heiles, C.E. and Drake, F.D. (1963) "The Polarization and Intensity of Thermal Radiation from a Planetary Surface," **Icarus 2,** 281-292.

Johnson, P.E., Kemp, J.C., Lebofsky, M.J. and Rieke, G.H. (1983) "10μm Polarimetry of Ceres," **Icarus, 56,** 381-392.

Landau, R. (1975) "The 3.5 micron Polarization of Mercury," **Icarus, 26,** 243-249.

Linsky, J.L. (1973) "The Moon as a Proposed Radiometric Standard for Microwave and Infrared Observations of Extended Sources," **Ap. J. Suppl. Ser. 216:25,** 163-204.

Love, T.J. (1968) **Radiative Heat Transfer,** Charles E. Merrill Publ. Co., Columbus, 287 pp.

Matson, D.L. (1971) "I. Astronomical Photometry at Wavelengths of 8.5, 10.5 and 11.6μm. II. Infrared Emission from Asteroids at Wavelengths of 8.5, 10.5, and 11.6μm," **Ph.D. Thesis,** California Institute of Technology.

Matson, D.L., Johnson, T.V., Veeder, G., Nelson, R.M., Morrison, D. Brown, R.H. and Tokunaga, A.T. (1983) "The Mystery of the Galilean Satellites' Brightness Temperatures," **BAAS, 15**, 852.

Mendell, W. W. (1976) "The Apollo 17 Infrared Scanning Radiometer", **Ph.D. Thesis**, Rice University, Houston, Texas, 183 pp., 92-97.

Mendell, W.W. and Lebofsky, L.A. (1982), "Lunarlike Thermal Emission and the Standard Asteroid Radiometric Model," **BAAS, 14**, 726.

Montgomery, C.G., Saari, J.M., Shorthill, R.W., Six, N.F. Jr. (1966) "Directional Characteristics of Lunar Thermal Emission," **Boeing Document D1-82-0568/Brown Tech. Note. R-213**, Huntsville, 102 pp.

Murcray, F.H. (1965) "The Spectral Dependence of Lunar Emissivity," **J. Geophys. Res., 70**, 4959-4962.

Özisik, M.N. (1973) **Radiative Transfer and Interactions with Conduction and Convection**, John Wiley and Sons, Inc., 575 pp.

Petit, E. and Nicholson, S.P. (1930) "Lunar Radiation and Temperatures," **Ap. J. 71 No. 2**, 102-135.

Saari, J.M. and Shorthill, R.W. (1966a) "Isothermal and Isophotic Contours for the Lunar Disk Through a Lunation," **Boeing Document D1-82-0552-1**, Seattle, 95 pp.

Saari, J.M. and Shorthill, R.W. (1966b) "Isothermal and Isophotic Atlas of the Moon," **NASA Contractors Rept. CR-855**, NASA.

Saari, J.M. and Shorthill, R.W. (1966c) "Review of Lunar Infrared Observations," **Boeing Document D1-82- 0586**, Seattle, 43 pp.

Saari, J.M. and Shorthill, R.W. (1972) "The Sunlit Lunar Surface I and II," **The Moon, 5**, 161-199.

Saari, J.M., Shorthill, R.W. and Deaton, T.K. (1966) "Infrared and Visible Images of the Eclipsed Moon of December 19, 1964," **Icarus, 5**, 635-659.

Shorthill, R.W. and Saari, J.M. (1965) "Radiometric and Photometric Mapping of the Moon through a Lunation," **Ann. N.Y. Acad. Sci., 123**, 722-739.

Spencer, J.R. (1987) "The Surfaces of Europa, Ganymede, and Callisto: An Investigation Using Voyager IRIS Thermal Infrared Spectra," **Ph.D. Dissertation**, Univ. of Arizona, Tucson, Arizona, 211 pp.

Veverka, J. and Wasserman, L. (1972) "Effects of Surface Roughness on the Photometric Properties of Mars," **Icarus, 16**, 281-290.

Vogler, K.J., Johnson, P.E. and Shorthill, R.W. (1987) "Infrared Calibration from High Resolution Planetary and Lunar Measurements," **BAAS 19**, 871.

Vogler, K.J., Johnson, P.E. and Shorthill, R.W. (1988) "Improved Thermal Models for Solid Planetary Bodies," **Lunar and Planetary Science XIX**, 1217, Lunar and Planetary Institute, Houston.

TABLE 1: Summary of Computer Models

Model A: • rotating asteroid with arbitrary pole orientation.
           • solves one dimensional heat flow equation into surface.
           • input parameters include heliocentric distance, rotation period, bolometric bond albedo and emissivity, anisotropy of emission, wavelength and thermal inertia.

Model B: • low albedo spots added to Model A in order to mimic surface roughness.

Model C: • treats surface roughness as paraboloidal holes (craters).
           • includes treatment of scattered incident radiation and re-emitted thermal radiation inside crater.
           • input parameters include depth to diameter ratio, dielectric constant (emissivity), bidirectional reflectance, illumination/viewing geometry and heliocentric distance.
           • option of directional emissivity.

Model D: • places a distribution of craters from Model C on a smooth dielectric sphere with the craters covering a given percentage of the surface.
           • no directional emissivity inside the craters.
           • illumination/viewing conditions are for full moon.
           • heliocentric distance included.

Model E: • identical to Model D except for the addition of directional emissivity inside the craters.

TABLE 2: Correspondence of 10μm Brightness
Temperature Scan from Saari and Shorthill (1972)
and Visable Lunar Features.

Angular Distance From Moon's Center, θ	Type of Feature	Name of Feature
$0° \leq \theta \leq 5°$	Maria	Sinus Medii
$5° \leq \theta \leq 10°$	Highland	—
$10° \leq \theta \leq 15°$	Maria	Mare Vaporum
$15° \leq \theta \leq 25°$	Highland	Appenine Mountains and surroundings
$25° \leq \theta \leq 40°$	mostly Maria	Palus Putredinis, Palus Nebularum
$40° \leq \theta \leq 55°$	Highland	Lunar Alps and surroundings
$55° \leq \theta \leq 60°$	Maria	Mare Frigoris
$60° \leq \theta \leq 90°$	Highlands	North Polar Highlands

FIGURES

FIGURE 1: Brightness temperature spectra for two surfaces. The upper curve is for a distribution of $T_1=340$ K and $T_2=400$ K each covering equal areas, where $\epsilon_1 = \epsilon_2=0.95$. The lower curve is for a $T_{avg}=370$ K and $\epsilon=0.95$. Notice that assuming an average temperature over a region that has local temperature contrasts results in a cooler and less steep brightness temperature spectrum.
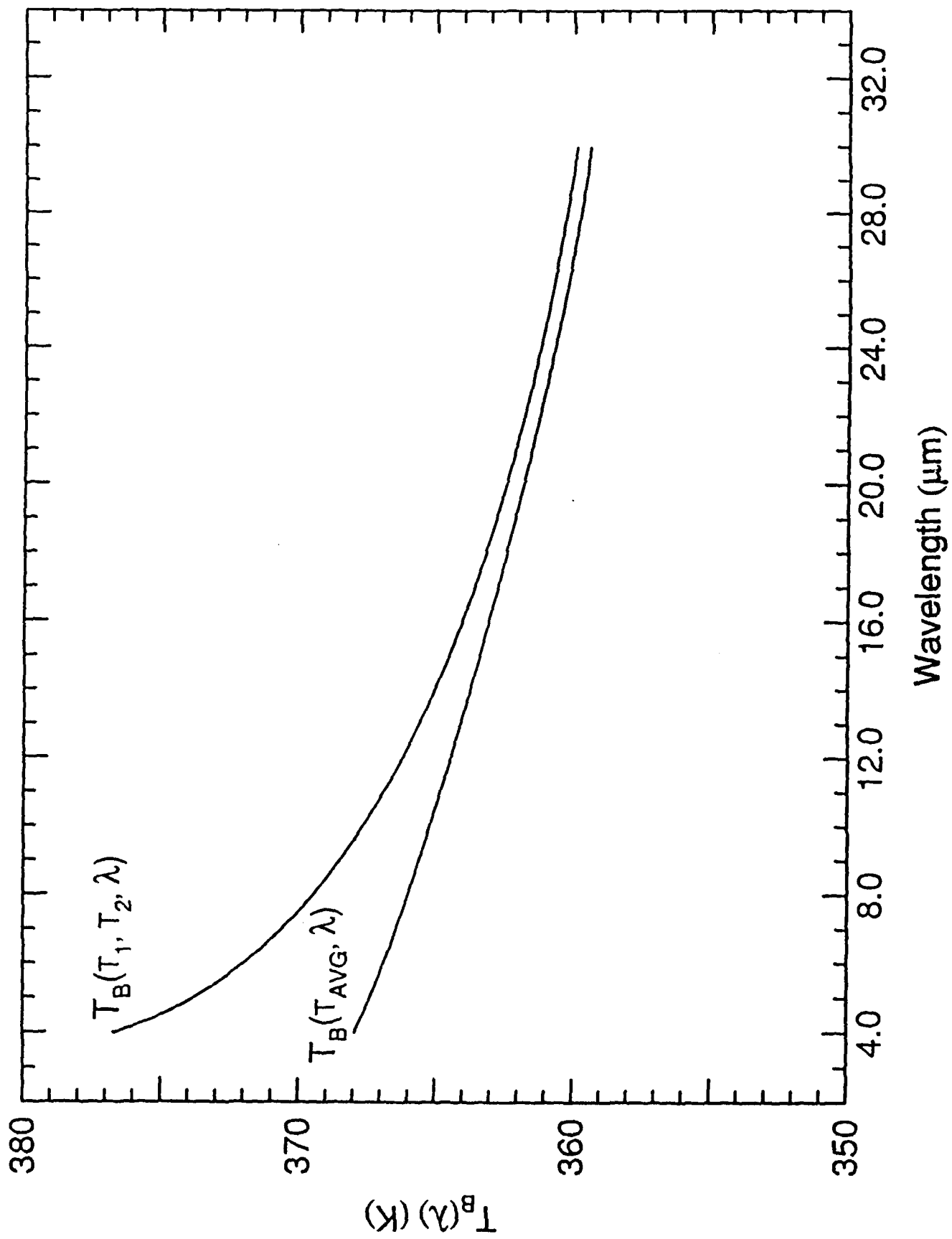
FIGURE 2: Disc-integrated brightness temperature spectrum calculated with low albedo spots by Model B, and compared to Murcray's (1965) data. Model parameters, are low albedo=0.01 with 60% coverage, high albedo=0.18 with 40% coverage, emissivity=0.94, specific heat=0.2 cal $gm^{-1}K^{-1}$ and thermal inertia=0.001 cal $K^{-1}cm^{-2}sec^{-1/2}$. The lines through the data and model points represent linear least squares fits to the points which allows comparison of the slopes.

FIGURE 3: 10μm brightness temperature vs. θ ($i=\epsilon=\theta$, $\alpha=0°$) as a function of depth to diameter ratio as calculated by Model C, (directional emissivity included inside the crater). Calculations used 180 crater elements, a bidirectional reflectance of 0.025 and a hemispherical reflectance of 0.05 corresponding to a Bond albedo of approximagely 0.06, and a dielectric constant of 3.0 corresponding to $E(\epsilon,0°) \simeq .92$. Notice that the finite size of the crater elements introduces small oscillations into the T_B vs. θ curve as depth to diameter ratio is increased. For example, calculations with 60 crater elements would produce oscillations in an h/D=0.25 curve similar to the oscillations in the h/D=0.45 curve in this figure.

FIGURE 4: 10μm brightness temperature vs. θ: Upper and lower limit depth to diameter ratio fits for the full Moon as calculated by Model E. The upper curve has the parameters h/D = 0.51, dielectric constant = 3.0, bidirectional reflectance = 0.03, hemispherical reflectance = 0.065, derived from a Bond albedo of 0.08 and a weighting of 87% rought surface and 13% smooth surface. The lower curve has h/D = 0.46 with all other parameters the same. Comparison data is from Saari and Shorthill (1972). A closer fit in depth to diameter ratio lies between these two sets of parameters. H refers to highland regions and M to maria (See Table 2).

FIGURE 5: 10μm brightness temperature vs. θ: Upper and lower limit reflectance fits as calculated by Model E. The upper curve has the parameters h/D=0.49, dielectric constant = 3.0, bidirectional reflectance = 0.022, hemispherical reflectance = 0.049 derived from a Bond albedo of 0.060 and a weighting of 87% rough surface and 13% smooth surface. The lower curve has a bidirectional reflectance of 0.051, a hemispherical reflectance of 0.121 derived from a Bond albedo of 0.15. All other parameters are the same. Comparison data is from Saari and Shorthill (1972). H refers to highland region and M to maria (see Table 2).

FIGURE 6: Disc-integrated brightness temperature spectra as calculated by Model E and compared to Murcray's (1965) data. Model parameters are the same as those in Figures 4 and 5. The lines through the data and model points represent linear least squares fits to the points which allows for comparison of the slopes.
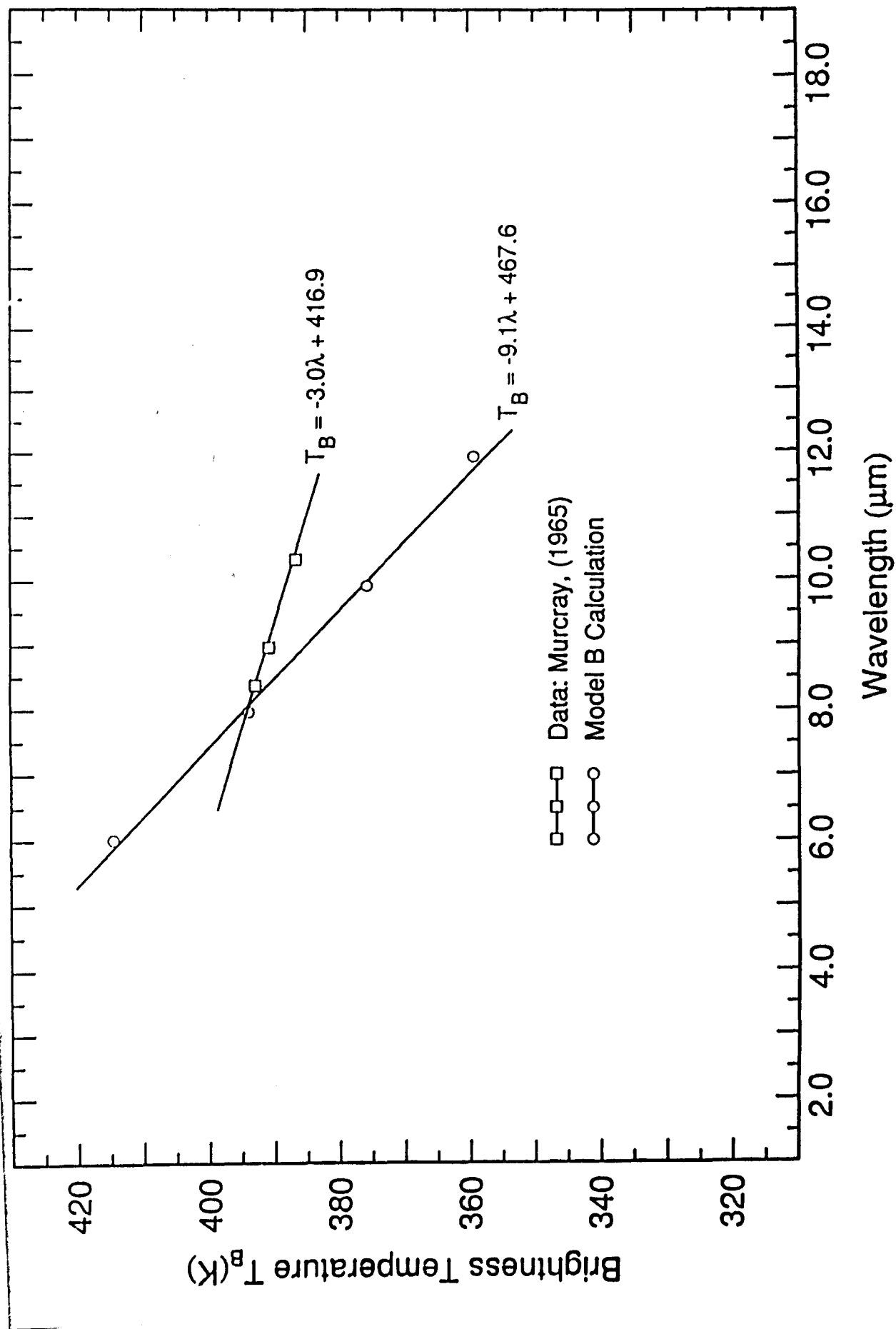
$T_B = -3.0\lambda + 416.9$

$T_B = -9.1\lambda + 467.6$

Data: Murcray, (1965)
Model B Calculation

Wavelength (μm)

Brightness Temperature T_B(K)

Figure axes:

y-axis: $10\mu m$ Brightness Temperature $T_B(\theta)$ (K)

x-axis: $\theta(deg)$: Angular Distance From Disc Center

Legend:
- Model E: Upper Limit h/D Fit
- Model E: Lower Limit h/D Fit
- Saari and Shorthill (1972)

Figure: Brightness Temperature T_B(K) versus Wavelength (μm).

$T_B = -3.0\lambda + 416.9$

$T_B = -3.8\lambda + 417.1$

$T_B = -3.7\lambda + 413.1$

$T_B = -3.7\lambda + 408.9$

$T_B = -3.6\lambda + 406.5$

Data: Murcray, (1965)

Model E Calculations

Upper Limit h/D Fit

Lower Limit h/D Fit

Upper Limit Reflectance Fit

Lower Limit Reflectance Fit

5.5 Surface Roughness and Infrared Emission from Solid-Surfaced Planetary Bodies.

SURFACE ROUGHNESS AND INFRARED EMISSION
FROM SOLID-SURFACED PLANETARY BODIES

A THESIS PROPOSAL

By Karl Vogler

Thermal modeling is an important tool for studying the thermophysical properties of solid-surfaced planetary bodies, and in determining asteroid diameters and albedos. An early thermal models by Wesselink (1948) examined heat conduction in the lunar surface and gave a quantitative explanation for the surface temperature variations measured during an eclipse and throughout a lunation by Pet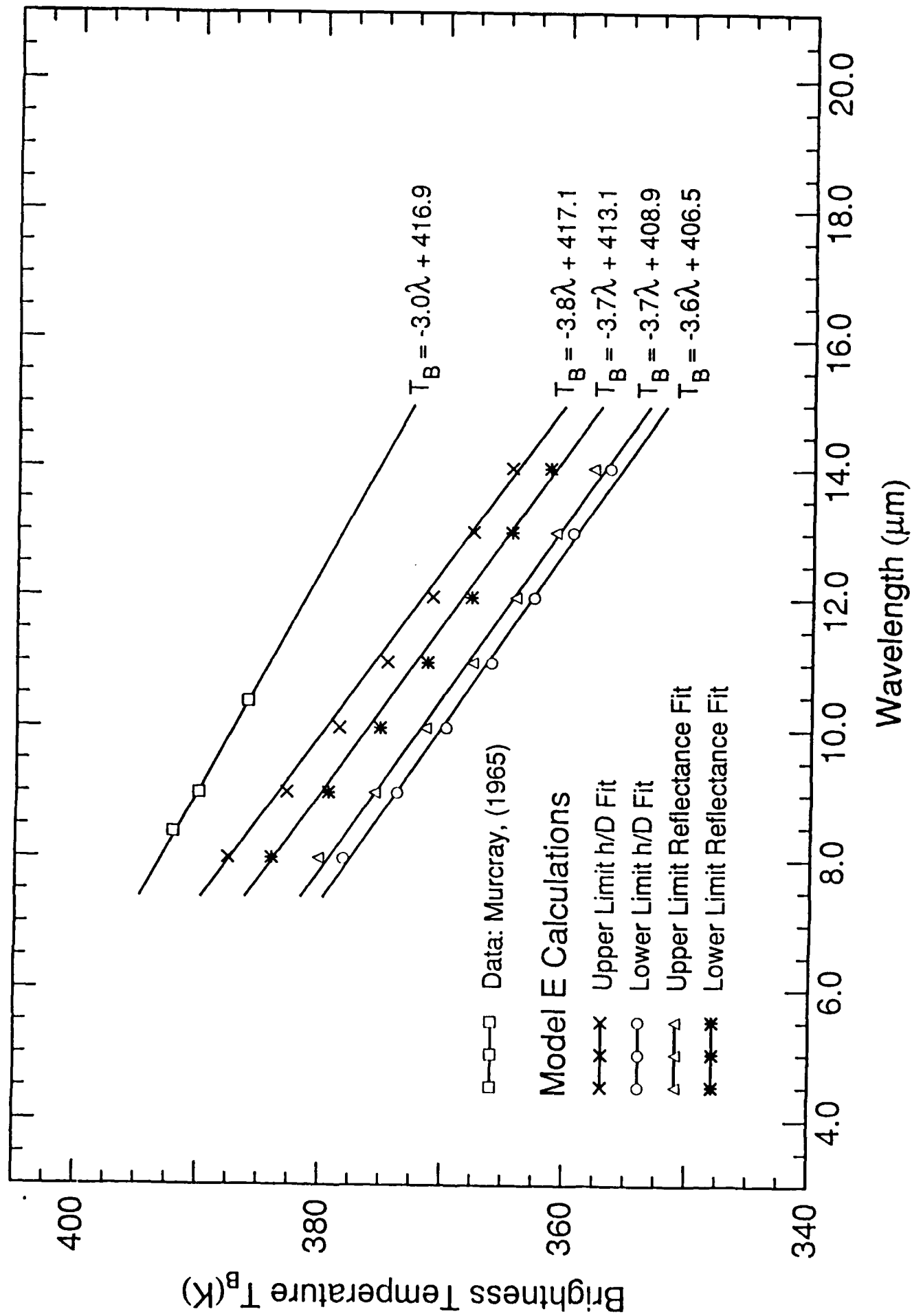it and Nicholson (1930), and Petit (1940). Later models continued to study surface properties in the manner of Wesselink (1948). Allen(1970) first applied thermal radiometry to asteroids when he used 10μm observations of 4 Vesta and a thermal model to obtain an "infrared" diameter. Other early work includes Matson (1971), Morrison (1973), Jones and Morrison (1974), and Hansen(1976a). The thermal models described by these authors are roughly equivalent and can be considered as a "standard" or lunar-like model. (Morrison and Lebofsky, 1979). The assumption is that the larger asteroids are similar to the moon in shape and also have a significant regolith. This allows the standard model to be tested with lunar observations before being applied to asteroid measurements. The details of the "standard" model and recent improvements will be discussed later. A review of the thermal modeling literature will reveal that effects caused by macroscopic surface roughness, i.e. directionality of thermal emission, subsolar point and limb temperature enhancement, and the behavior of the thermal emission spectra for these asteroid-like objects have either been treated empirically or not at all. A few models do describe surface roughness effects but only for a single bandpass. In addition, the empirical treatment of surface roughness has lead to minor confusion over the value of the scaling factor involved as reported by Morrison and Lebofsky, 1979.

1

The standard thermal model assumes an ideal, spherical asteroid whose surface elements are in instantaneous thermal equilibrium with the absorbed fraction of the incident solar radiation. The asteroid is non-rotating and is observed at zero phase angle. Thus for this spherical asteroid in equilibrium with the solar insolation we write:

$$\pi r^2(1-A)S = \beta\epsilon\sigma r^2\int_{-\pi}^{\pi}\int_{-\pi/2}^{\pi/2} T^4(\theta,\phi)\cos\phi\, d\phi\, d\theta$$

where r is the radius of the asteroid, A is the bolometric Bond albedo, S is the incident solar flux, ϵ is the wavelength independent bolometric emissivity and σ is the Stephan-Boltzmann constant. $T(\theta,\phi)$ is the effective temperature of a point on the surface at latitude ϕ and longitude θ. β is the normalization constant which is used to allow for the angular distribution of thermal emission. the Sun and Earth are in the asteroids equatorial plane at $\theta = \phi = \emptyset^{\circ}$ which defines zero phase angle. Infrared emissivities for dielectric materials are around $\epsilon = \emptyset.9$ which is the value typically used in the standard thermal model. Changes in the emissivity will alter the effective temperature and the wavelength dependence of the brightness, but will have only a small effect on the flux in a given bandpass.

The temperature distribution $T(\theta,\phi)$ is assumed to depend primarily on the thermal inertia of the surface. The standard model assumes low thermal inertia and uses the distribution:

$$T(\theta,\phi) = \begin{cases} T_{max}\cos^{1/4}\theta\cos^{1/4}\phi & ; \quad \theta,\phi \leq \pi/2 \\ 0 & ; \quad otherwise \end{cases}$$

2

Low thermal inertia implies a loose particulate regolith. A more realistic

approach is to solve a one dimensional heat flow equation into the

subsurface of each surface element of the sphere as done by Matson (1971),

Cuzzi (1973), Landau(1975) and Johnson et. al. (1983). Other improvements

in the temperature distribution in addition to the thermal inertia include

asteroid rotation rate and pole orientation as done by Cuzzi(1973),

Johnson et.al. (1983) and Lebofsky et.al. (1984).

The normalization factor β is an empirically determined constant

which modifies the temperature distribution $T(\theta, \phi)$ so that the

directionality of infrared emission and surface temperature enhancement at

small phase angles is accounted for in some fashion. β is often referred

to as the infrared beaming factor. The infrared beaming factor is actually

the reciprocal of the enhancement in total thermal flux at zero phase

angle over that of a uniformly radiating sphere (Lebofsky et.al., 1986).

For objects like the Moon, $\beta < 1$. The flux enhancement for which

accounts appears in lunar measurements by Petit and Nicholson (1930),

Saari and Shorthill (1966a,b), Shorthill and Saari (1965), and Mendell

(1976). Small scale macroscopic surface roughness is the apparent cause of

the enhancement (Mendell and Lebofsky, 1982). All of the standard models

mentioned, used this normalization factor or an equivalent empirical

parameter.

There are a few observational facts that the standard model does not

account for. Matson et. al. (1983) reported a marked decrease of infrared

brightness temperature with increasing wavelength for the Galilean

satellites, confirming earlier reports by Hansen (1976b). The observed

decrease of brightness temperature between 10μm and 20μm is steeper than

can be explained by the standard model. Matson et. al. (1983) have also shown that photometric calibration errors and wavelength dependent emissivity will not explain the observations. Murcray's (1965) 6 to 12μm data shows a negative slope in the brightness temperature spectrum. The same effect is also observed in the Voyager IRIS 4 to 55μm data for the Galilean satellites. Spencer (1987) also states that temperature variations across the instruments field of view due to global temperature gradients make only a small contribution to the spectral slope. Having ruled out these possible causes of the observed behavior of the infrared brightness temperature spectrum, one is left with local temperature contrasts as the probable cause.

Measurements by Petit and Nicholson (1930) first revealed the non-Lambertian emission of the lunar surface near zero phase. Their temperature measurements along the lunar equator varied as $\cos^{\frac{1}{6}}\theta$ instead of $\cos^{\frac{1}{4}}\theta$ which is expected of a Lambertian surface. (θ is the angular distance from the subsolar point.) In addition, their subsolar point temperature of 407K indicates that thermal emission is significantly enhanced over that of a blackbody sphere for which one expects 395K. Deviations from diffuse emission were explained by a general surface roughness. Saari and Shorthill (1972), using their measured isophotic and 10μm isothermal contours of the full Moon (Shorthill and Saari, 1965 ; Saari and Shorthill 1966a,b) characterized the lunar brightness temperature by the least squares fit, $T(K) = 324.2 + 72.6\cos\theta$ where θ is the angular distance from the subsolar point. In addition, the directional infrared emission from the full Moon was determined as a function of observer elevation and azimuth angles of three sun elevation angles. It

4

was concluded that the brightness temperature of the sunlit lunar surface is influenced primarily by an average surface roughness and albedo variations (Saari and Shorthill, 1972).

Jones and Morrison (1974) first determined $\beta \sim 0.9$ by calibrating their models on the moon and Galilean satellites, and used their model to determine diameters for eight asteroids. Hansen (1976a) assumed a temperature distribution with significant dark side emission and a limb temperature which was 60% of the subsolar point temperature. This yielded a value of $\beta \sim 1.3$, and diameters and emissivities which differed significantly from those of Jones and Morrison (1974). Hansen (1977) later added a rough, cratered surface to his model which resulted in $\beta \sim 1.0$ and gave results similar to those of Jones and Morrison (1974). Morrison and Lebofsky (1979) used a more refined standard model to examine Hansen's results. Morrison and Lebofsky concluded that Hansen's assumption of significant dark side thermal emission resulted in a non-lunar-like model. In addition, they found that Hansen had treated the thermal emission spectrum as a single graybody instead of a composite of graybodies at different temperatures. This assumption caused the small emissivities in Hansen's (1976a) paper. Morrison and Lebofsky also noted that when the temperature distribution was changed and the error corrected most of the discrepancies between Hansen (1976a) and Jones and Morrison (1974) disappeared without the need of the cratered surface model. One notes, however, that Saari and Shorthills' (1972) result gives a limb temperature that is roughly 80% of the subsolar point temperature, indicating the validity of Hansen's temperature distribution for $\theta, \phi \lesssim \frac{\pi}{2}$. The significance of $\beta \sim 1.0$ indicates that Hansen's treatment of a rough surface is

approximately correct in accounting for the observed flux enhancements. Clearly, a detailed surface roughness model should be pursued.

More recent discussions of asteroid radiometry center on better empirical determinations of β . Brown et al. (1982) improved the empirical determination of β at 10μm and 20μm by using the occultation diameters of two asteroids and a Jovian satellite. Lebofsky et. al. (1986) further refined this technique by using the light curves and occultation diameters of 1 Ceres and 2 Pallas. These more recent models are calculated at 10μm and 20μm and do not address the observed behavior of the thermal emission spectra reported by Matson et.al.(1983).

Local temperature contrasts, as mentioned earlier, are the apparent cause of the observed behavior of infrared thermal emission spectra for solid surfaced planetary bodies. A local temperature contrast is defined as any variation in surface temperature on a scale smaller than the field of view at the detector. There are several mechanisms capable of producing local temperature contrasts, (1) albedo variations, (2) thermal inertia variations, and (3) macroscopic surface roughness. Albedo variations can cause local temperature contrasts since higher albedo surfaces will in general be cooler than lower albedo surfaces. Also, high thermal inertia material exhibits smaller diurnal changes in surface temperature than low thermal inertia material. Thus a mixture of high and low thermal inertia material could produce local temperature contrasts. Surface roughness on a macroscopic scale will cause local temperature contrasts as a direct result of variations in illumination of the surface. the term macroscopic implies that the scale of roughness is larger than the wavelengths being considered and is large enough so that temperature contrasts will not be

6

removed by conduction (i.e. larger than a few centimeters)(Spencer 1987).

Flat surfaces tilted toward the sun will be warmer than those tilted away.

More obviously shadowed regions are cooler than those in full sunlight. In

addition, features with negative relief (holes, crevices, etc.) will see

scattered incident radiation and re-emitted thermal radiation from other

points inside the same depression, and thus will appear hotter than their

surroundings. All of these effects occur in real planetary surfaces and

are amenable to thermal modeling.

Surface roughness effects have been modeled by a number of

researchers over the past 20-30 years. A brief review of these results

will reveal topics that have been overlooked.Hameen-Anttila et.al. (1965)

examined the shadowing effect caused by a rough surface and how it affects

the phase curve of lunar type surfaces. Buhl et.al. (1968a and b)

considered the effects of a cratered surface in altering the emission

characteristics of the lunar surface but only examined radiation emitted

at the subsolar point and at full Moon. Bastin and Gough (1969) modeled

surface roughness as a series of parallel troughs in order to study the

lunar observations in the 10μm bandpass. Winter and Krupp (1970) modeled

the 10μm lunar data of Saari and Shorthill by looking at the emission

characteristics of cratered surfaces using various crater shapes and

distributions. Sexl et.al.(1971) studied the directional characteristics

of lunar emission at 10μm using a cratered surface model with an empirical

radiation law describing the angular dependence of radiation emitted by a

flat element of lunar surface. Models similar to those above exist for

Mars (Ververka and Wasserman, 1972 and Buratti and Ververka, 1985) and

for Mercury (Landau, 1975). All of these models assume diffuse emission

7

except for Sexl et.al. (1971). In addition, the models above are calculated for a single bandpass, do not have any disk-integrated results, and are specific to the object discussed in terms of illumination conditions.

I propose to study the effects due to surface roughness in solid-surfaced planetary bodies using thermophysical computer models and high resolution ($\sim$1 arcsec) images of the Moon. The goal of the modeling is to develop and refine a surface roughness algorithm which will replace the infrared beaming factor in the "standard" thermal model. The goal of the lunar imaging portion is to provide additional data for testing the models, as well as providing high resolution infrared maps of selected regions with which to study lunar surface properties. The overall goal of this project is to determine if surface roughness effects can explain the behavior of infrared emission spectra and deviations from diffuse emission. In addition, I wish to examine if it is possible to directly measure surface roughness using remote infrared measurements and computer models.

The previous discussion of the literature clearly indicates the need for a general surface roughness algorithm to replace the empirical infrared beaming factor, so that the behavior of infrared emission spectra and deviations from diffuse emission can be further explored. The geometry used in the roughness model must produce a distribution of slopes, shadows, and depressions all of which vary with phase angle, heliocentric distance, and surface properties. The model should then calculate surface temperature and emitted intensity and flux as a function of position on the sphere. A disk-integrated brightness temperature and total emitted

8

intensity and flux must also be calculated. A computer model which

performs the above calculations has been implemented and is being tested

and modified.

This current model treats macroscopic surface roughness as

paraboloidal holes of specified depth to diameter ratio, albedo,

emissivity, and illumination/viewing geometry. The geometry is the same as

that used by Hämeen-Antilla et.al. (1965). Using this geometry the model

calculates the illumination conditions for a surface element inside a

paraboloid. The scattered incident radiation and re-emitted thermal

radiation from other elements inside the paraboloid are calculated using

radiative heat transfer methods (Spencer, 1987 ; Bevens and Edwards,

1965). The result of these calculations is a temperature map of the

paraboloids surface from which the emitted intensity and flux is

calculated given the observing geometry. The emissivity of the surface is

derived from the Fresnel relations and Kirchoffs' Law. The model then

places a random distribution of single depth to diameter ratio depressions

over a smooth, gray, dielectric sphere with a weighting representing the

fraction of surface covered with depressions. Both disk-resolved and disk-

integrated properties are the calculated as functions of wavelength,

heliocentric distance, depth to diameter ratio, surface properties and

phase angle. Future modifications include the capability for a

distribution of depth to diameter ratios, albedo distributions, and the

possibility of including thermal inertia explicitly in the roughness

algorithm.

A data set of high resolution ($\sim$1 arcsec) images of selected regions

of the lunar surface is needed to study surface properties. I plan to

9

choose a minimum of two regions representing highlands, mare and regions of anomalous infrared emission (total of 6 regions minimum). The highlands are a high albedo surfaces and the mare represent low albedo surfaces. The majority of infrared anomaly regions ($\sim$ 80%) are associated with young craters with either ray systems and bright interiors or bright rims at Full Moon (Shorthill, 1972). The distribution of these regions on the lunar surface produces a range of illumination conditions for a given phase angle. This will serve as additional data for testing the computer models. A minimum of three separate phase angles for each region is desirable. Dark side measurements of one or two regions for at least three separate phase angles will allow construction of thermal inertia maps for a single wavelength. In addition, measurements for at least two different wavelengths for the regions of interest and for a single phase angle will allow the emission spectra to be examined. For each of the regions of interest I have Lunar Geologic Maps, Apollo Mapping Camera Photography, and Lunar Topographic Orthophotomaps (1:250,000) which will aid in interpretation of the images.

The images will in part be made with the mid-infrared Array Camera (built by Eric Ahrens and Roger Ball of Space Sciences Labs, Univ. of Cal. Berkeley) while mounted on the WIRO telescope. The Camera is a 10 x 64 infrared CCD array which is capable of measurements in the 10μm and 20μm atmospheric windows with 1% and 10% circularly variable filters. The plate scale for this instrument on the WIRO telescope is approximately 0.7 arcsec per pixel which corresponds to roughly 1.2 kilometers per pixel on the lunar surface. A one second integration time on the illuminated lunar surface yields a signal to noise ratio of $\gtrsim$ 500 whereas an integration of

10

four seconds on the dark side is required to reach S/N $\sim$100. Measurements for two regions were made on November 1, 1988 at 8.7 μm using this Array Camera at WIRO. Three clear nights with the moon visible and using this instrument should be sufficient to obtain the necessary lunar data.

REFERENCES:

Allen, D.A. (1970) "The Infrared Diameter of Vesta", Nature, 227, pp.158-159.

Bastin, J.A. and Gough, D.O. (1969) "Intermediate Scale Lunar Roughness", Icarus 11, pp.289-319.

Bevens, D.A. and Edwards, D.O. (1965) "Radiation Exchange in an Enclosure with Directional Wall Properties", J. Heat Transfer, 87C, pp.388-396.

Brown, R.H., Morrison, D., Tedesco, C.M., and Brunk, W. (1982) "Calibration of the Radiometric Asteroid Scale using Occultation Diameters", Icarus 55, pp.188-195.

Buhl, D., Welch, W.J. and Rea, D.G. (1968a) "Reradiation and Thermal Emission from Illuminated Craters on the Lunar Surface", J.Geophy.Res. 73, pp.7593-7608.

Buhl, D., Welch, W.J. and Rea, D.G. (1968b) "Anomolous Cooling of a Cratered Lunar Surface", J.Geophys.Res. 73, pp.5281-5295.

Cuzzi, J.M. (1973) "The Subsurface Nature of Mercury and Mars from Thermal Microwave Emission", Ph.D. Thesis, California Institute of Technology.

Hameen-Antilla, K.A., Laakso, P. and Lumme, K. (1965) "The Shadow Effect in the Phase Curves in Lunar Type Surfaces", Ann.Acad.Sci.Fenn. Ser.A, 172, pp.3-16.

Hansen, O.L. (1976a) "Radii and Albedos of 84 Asteroids from Visual and Infrared Photometry", Astron.J. 81, pp.74-84.

Hansen, O.L. (1976b) "Thermal Emission Spectra of 24 Asteroids and the Galilean Satellites", Icarus 27, pp.463-471.

Hansen, O.L. (1977) An Explication of the Radiometric Method For Size and Albedo Determination", Icarus 31, pp.456-482.

Jones, T.J. and Morrison, D. (1974) "Recalibration of the Photometric/ Radiometric Method of Determining Asteroid Sizes", Astron.J. 79, pp.892-895.

Johnson, P.E., Kemp, J.C., Lebofsky, M.J. and Rieke, G.H. (1983) "10μm Polarimetry of Ceres", Icarus 56, pp.381-392.

Landau, R. (1975) "The 3.5 Micron Polarization of Mercury", Icarus 26, pp.243-249.

Lebofsky, L.A., Sykes, M.V., Tedesco, E.F., Veeder, G.J., Matson, D.L., Brown, R.H., Gradie, J.C., Feierberg, M.A., Rudy, R.J. (1986) "A Refined 'Standard' Model for Asteroids Based on Observations of 1 Ceres and 2 Pallas", Icarus 68, pp.239-251.

1

Lebofsky, L.A., Sykes, M.V., Tedesco E.F., Veeder, G.J., Matson, D.L., Nolt, I.G., Radotitz, J.V., Ade, P.A.R., Gear, W.K., Griffen, M.J. and Robson, E.I. (1984) "Thermal Properites of the Regolith of Asteroid 1Ceres", Bull.Amer.Astron.Soc. 16, p.698.

Matson, D.L. (1971) "I.Astronomical Photometry at Wavelengths of 8.5, 10.5, and 11.6um. II. Infrared Emission from Asteroids at Wavelengths of 8.5, 10.5, and 11.6um", Ph.D. Thesis, California Institute of Technology.

Matson, D.L., Johnson, T.V., Veeder, G.J., Nelson, R.M., Morrison, D., Brown, R.H. and Tokunga, A.T. (1983) "The Mystery of the Galilean Satellites' Brightness Temperatures", Bull.Amer.Astron.Soc. 15, p.852.

Mendell, W.W. (1976) "The Apollo 17 Infrared Scanning Radiometer", Ph.D. Thesis, Rice University, Houston Tx. 182pp.

Mendell, W.W. and Lebofsky, L.A. (1982) "Lunarlike Thermal Emission and The Standard Asteroid Radiometric Model." Bull.Amer.Astron.Soc. 14, p.726.

Morrison, D. (1973) "Determination of Radii of Satellites and Asteroids from Radiometry and Photometry", Icarus 19, pp.1-14.

Morrison, D. (1974) "Radiometric Diameters and Albedos of 40 Asteroids", Astophys.J. 194, pp.203-212.

Morrison, D. and Lebofsky, L.A. (1980) "Radiometry of Asteroids", In ASTEROIDS (T. Gehrels ed.) pp.185-205 Univ. of Ariz. Press Tucson.

Murcray, F.H. (1965) "The Spectral Dependence of Lunar Emissivity" J.Geophys.Res. 70, pp.4959-4962.

Petit, E. and Nicholson, S.P. (1930) "Lunar Radiation and Temperatures", Astrophys.J. 71, pp.102-135.

Saari, J.M. and Shorthill, R.W. (1966a) "Isothermal and Isophotic Contours for the Lunar Disk Through a Lunation", Boeing Document D1-82-0552-1, Seattle, 95pp.

Saari, J.M. and Shorthill, R.W. (1966b) "Isothermal and Isophotic Atlas of the Moon", NASA Contractors Rept. CR-855 NASA.

Saari, J.M. and Shorthill, R.W. (1972) "The Sunlit Lunar Surface I and II", Moon 5, pp.161-195.

Sexl, R.U., Sexl, H., Stremnitzer, H. and Burkhard, D.G. (1971) "The Directional Characteristics of Lunar Infrared Radiation", Moon 3, pp.189-213.

Shorthill, R.W. and Saari, J.M. (1965) "Radiometric and Photometric Mapping of the Moon through a Lunation". Ann.N.Y.Acad.Sci. 123, pp.722-739.

Shorthill, R.W. (1972) "The Infrared Moon: A Review" in Thermal Characteristics of the Moon, Progress in Astronautics and Aeronautics, vol.28, pp.3-47, MIT Press Cambridge, Massachusetts and London, England

Spencer, J.R. (1987) "The Surfaces of Europa, Ganymede, and Callisto: An Investigation using Voyager IRIS Thermal Infrared Spectra", Ph.D. Dissertation, Univ. of Arizona, Tucson,Ariona. 211pp.

Veverka, J. and Wasserman, L. (1972) "Effects of Surface Roughness on the Photometric Properties of Mars", Icarus 167, pp.281-290.

Wesselink, A.J. (1948) "Heat Conductivity and the Nature of the Lunar Surface", Bull.Astron.Inst.Netherlands 10, pp.351-363.

Winter, D.F. and Krupp, J.A. (1971) "Directional Characteristics of Infrared Emission from the Moon", Moon 2, pp.279-292.

5.6   The ADC-1 data acquisition and control peripneral (1page).

The ADC-1

An Accurate and Reliable Data Acquisition and Control System for Under $500

The Data Acquisition AND Control Peripheral

- 16 Analog Inputs
- 4 Digital Inputs
- 6 Controlled Outputs
- 32 Powerline Carrier Control Points
- RS-232 Serial Communications
- Low Power CMOS Components

REMOTE MEASUREMENT SYSTEMS

SPECIFICATIONS:

Analog Inputs:

- 16 differential analog inputs
- Integrating dual slope 12 bit A/D converter
- Sample rate of 20 samples/sec with input auto zeroing
- Sample rate of over 120 samples/sec without auto zeroing at 11 bit resolution
- Standard ± 0.4 Volt input range, alternate ranges of ±1.0, ±2.0, and ±4.0 volts are available
- Stable reference voltage provides temperature coefficient of 40 PPM/°C
- Accuracy to ± 1/2 LSB
- Input impedance 10 Meg Ω. 110 dB noise rejection at 60 Hz.

Digital Inputs:

- 4 digital inputs
- Individually configurable for normally open or normally closed circuits
- 2 states - toggle or latched.
- Monitoring rates to 400 Hz (at 9600 baud with appropriate software).

Controlled Outputs:

- 6 independently controlled open collector TTL outputs.
- Each output controls up to 200 ma at 5 VDC
- Control rate to 400 Hz

BSR X-10 Powerline Carrier Transmitter:

- Sends control codes on AC powerline for operation of 32 remote modules
- Eight switch-selectable banks of 32 software selectable addresses for control of up to 256 different modules

- Transmitter and AC line connection in separate optically-isolated enclosure minimizes 60 Hz noise
- Control rate of 2/second

Communications:

- 300 to 9600 baud
- 3 wire RS-232 or TTL
- 8 data bits, 1 stop bit.
- Bit mapped instructions
- Disable line for multiple unit operation

Owner's Manual:

- Detailed description of ADC-1 operation
- Specific sensor interconnection instructions.
- Provides programming examples and implementation instructions for over 20 different computers.

Environmental:

- Operating temp 0-50C.
- Non-condensing

Power:

- Requires 5 - 24 VDC
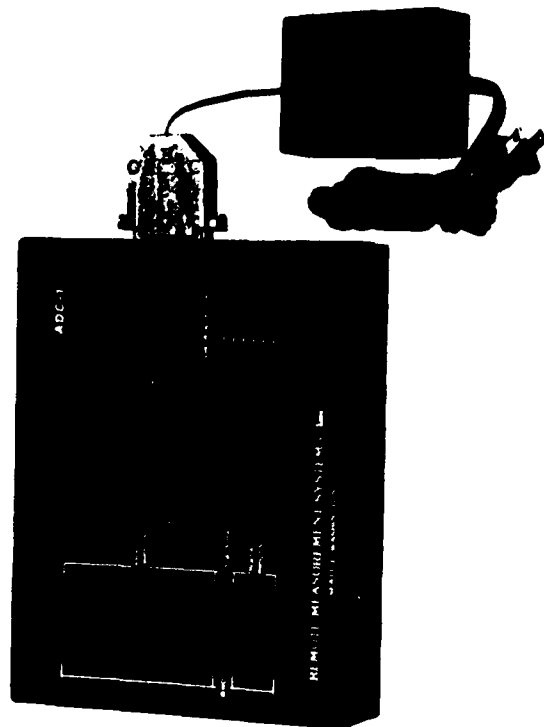- Consumes 20ma at 5 v

Physical Specifications:

- Dimensions, 8x7x2 inches
- Weight, 2 lbs
- Rugged aluminum enclosure
- Built in terminal strips
- Female DB 25 for RS-232 interface (DTE)

OPTIONS:

- **ADC-1-B** A reduced price model for applications such as data logging, where only measurement capabilities and controlled outputs are required. The ADC-1-B has no BSR X-10 control capability.

- **ADC-1-B-12C** Expands the number of controlled outputs from 6 to 12, without BSR control capability.

- **ADC-1-8Ax and -16Ax** Provides an internal instrumentation amplifier for either 8 or 16 channels with amplification gains of 10, 20, 30, 40, or 50. A gain of 50 provides 2 μV resolution over a range of ± 8 mV. The amplifier is software controlled and recommended for thermocouples and strain gages.

- **ADC-1-32SE** Provides 32 single-ended analog inputs, rather than 16 differential inputs. Digitized voltages are referenced to ADC-1 ground. The ADC-1-32SE is not available with amplification.

- **ADC-1-Rx.x** A/D range is modified to user specification within the range of ± 0.4 to ± 4.0 volts. The standard range is ± 0.4 volts to maximize resolution with commonly used sensors. Resistive voltage dividers offer scaling of higher input voltages on individual inputs.

REMOTE MEASUREMENT SYSTEMS INC

2633 Eastlake Avenue East, Suite 200, Seattle, Washington 98102
Phone (206) 328-2255   Telex: 650-274-9152

REV 1288

5.7   The RTD Resistance Temperature Device.(3 pages).

RTD Resistance Temperature Device

The Probe
A probe is an assembly composed of an element, a sheath, lead wire, and a termination or connection.

The termination
Probe may be terminated in a connector head, quick-disconnect, terminal block, or extension wire. OMEGA's standard terminations are pictured on pages E-5 through E-7. Other terminations are available upon special request. Please give a full description and send sketches.

The lead wire
Lead styles are offered in one of four configurations (see diagrams at the side of this page). Style 2 is OMEGA's standard. Be sure to select the configuration that is compatible with your instrumentation.

The sheath
The sheath, a closed end tube, immobilizes the element against moisture and the environment to be measured. The sheath also provides probe protection and stabilizes the element from the transition lead wire to the tip. OMEGA's standard sheaths are ¼" and ⅛" O.D. 304 stainless steel tube. Other O.D.'s and materials are available upon request...

Temperature Rating
OMEGA's Standard RTD probe assemblies are rated for use in temperatures up to 1112°F (600°C). Temperature limitation may be placed on termination styles due to wire insulation used. The maximum temperature rating available on special order is 1382°F (750°C). If probe is intended for high temperature use, please request quotation.

OMEGA stocks a broad line of RTD probes for immediate delivery. Please see pages E-3 through E-7 for standard lengths. Many special assembly probes are available for shipment within two weeks of receipt of your order. Please consult Sales Department for further details on your special needs.

Definition of RTD Probe Part Number

PR - [ ] - [ ] - [ ] - [ ] - [ ]
- TYPE
- LEAD CONFIG.
- ELEMENT RESIS.
- DIAMETER
- LENGTH
- SE CURVE

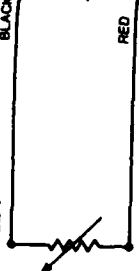Type: Select style 11, 12, 13, 14, 15 or PRX (pages E-3 through E-7), or 4. Style 2 is standard. Lead Configuration: Specify 1, 2, 3, or 4. Style 2 is standard. Resistance: 100 ohms is standard. 0, 200, 500, 1000, or 2000 ohms are available, with two wires...

Lead Configurations of RTD Probes

STYLE 1
BLACK

RED
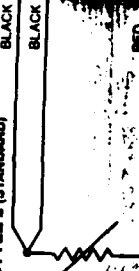
ELEMENT

Lead configuration 1 provides one connection to each end of the sensor. This construction is available where the resistance of the run of lead wire may be considered as an additive constant in the circuit, and particularly where the changes in lead resistance due to ambient temperature changes may be ignored.

STYLE 2 (STANDARD)
BLACK

BLACK

RED

ELEMENT

Lead configuration 2 provides one connection to one end and two to the other end of the sensor. Connected to an instrument designed to accept three wire input, compensation is achieved for lead resistance and temperature change in lead resistance. This is the most commonly used configuration.

STYLE 3
BLACK

BLACK

Omegafilm RTD Element For Fast Response!

$22 each

To Order, Specify: 100W30

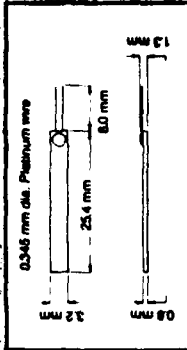*Available Off-The-Shelf*

Type 100W30

The 100W30 Platinum Resistance Temperature Detector has been developed to provide the typical high quality of platinum RTD sensors at lower cost. The 100W30 is size equivalent to standard sized elements, and utilizes a thick film design for long term stability. Compared to standard 3 mm wire wound sensors, the second generation 100W30 has up to 4 times the response time, and is a direct replacement. The type 100 sensor is calibrated to DIN43760, BS1904 and IEC751 specifications, with an alpha coefficient of 0.00385. Nominal resistance is 100 ohms at 0°C. These sensors may be operated at temperatures up to 600°C.

Technical Data
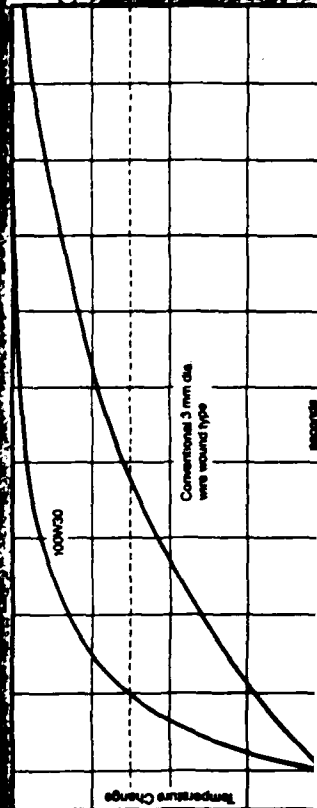Sensor Type: Thick film platinum RTD, α = 0.00385.
Surface Insulation: 1000M ohm at room temp. and 250 V, or 20M ohm at 600°C and 50 V.
Response Time: Less than 0.1 sec. to reach 63% of ultimate.
Temperature Range (BS1904 feet).
Self Heating Effect: Less than 0.009°C/mw when immersed in stirred water at ice point.
Stability after Temperature Cycling: Less than 0.06% after 10 cycles between −70 and 600°C.
Temperature Range: −70 to 600°C.
Fundamental Interval: 38.5 ohms nominal (0 to 100°C).
Dimensions: 1.0" L x 0.128" W x 0.031" D (25.4 mm x 3.2 mm x 0.8 mm) plus platinum lead wires 0.0136" (0.346 mm) x 0.315" (8.0 mm) long.

Model WS81. The WS81 donut shaped 100 ohm RTD element offers fast, accurate, temperature measurement as well as a convenient means of attaching it to a surface without cementing. These highly versatile units can be secured to a surface by a machine screw and washer, or by a rivet. They can also be directly cemented with or without the use of a vertical centering post. Rated temperature is from –50°C to 850°C. Accuracy and response are enhanced by locating the winding deposition only 0.007″ beneath the mounting surface. The rugged ceramic body, with firmly strain relieved 0.015″ diameter platinum, is designed to withstand high vibration conditions. This versatile 100 ohm unit meets DIN standard 43760.

Series W. Series W are rugged ceramic cylindrically shaped elements for use in the temperature range from –50°C to 600°C. Elements have .015″ gold palladium alloy leads approximately 0.4″ long, which are strain relieved in the stress free ceramic body. Elements are available in both angle and dual configurations with resistances at 0°C of 100, 200, 400, 500, 1000 and 2000 ohms. Construction conforms to standard DIN 43760 with 0.1% Tolerance tolerance.

OMEGAFILM RTD's may be used with various OMEGA controllers and digital readout thermometers. The following lists where some of these instruments are featured in this catalog.

a) CN2000 Controllers
b) DP80 Digital Indicators
c) Series 651 Digital Meters

OMEGA can offer Series W and Series F OMEGAFILM RTD's encapsulated in head mounting assemblies similar to P/N ON-930, ON-950 and ON-960 shown on Pg. F-5K. Please contact OMEGA's Applications Engineering Department about custom assemblies.

Discount Schedule
1-10 units .... Net
11-24 units 10%

OMEGAFILM — Platinum RTD Elements (Alpha = .00385)

Series	Dimensions (mm) 1 mm = .03937″	Single or Dual	Nominal Resistance OHMS	Temperature Range	Catalog Number	Price
F	1 mm Thick	1	100		F3101	$19
		x	500	–50°C to +600°C	F3131	19
		1	1000		F3141	19
F	1 mm Thick	1	100		F3102	19
		1	500		F3132	19
		1	1000		F3142	19
F	1 mm Thick	1	100		F3104	19
	1 mm Thick	1	100		F3105	19
WS		1	100	–50°C to +850°C	WS81	$7

OMEGAFILM — Platinum RTD Elements (Alpha = .00385)

Series	Dimensions (mm) 1 mm = .03937″	Single or Dual	Nominal Resistance OHMS	Temperature Range	Catalog Number	Price
W	30 mm / 12	1	100		W2102	$32
		x	200		W2112	35
		1	400		W2122	39
		1	500		W2132	39
		x	1000		W2142	48
		1	2000		W2152	97
W	30 mm / 12	2	100	–50°C to +600°C	W2202	58
		x	200		W2212	88
		2	400		W2222	66
		2	500		W2232	61
		2	1000		W2242	71
W	2.0 mm / 7	1	100		W2103	36
W	2.0 mm / 5	2	100		W2204	64

5.8 Articles

Asteroid flybys during trip to Jupiter will capitalize on U. scientist's work

By JoAnn Jacobsen-Wells
Deseret News science writer

A University of Utah researcher who conducted infrared studies of asteroids for the Air Force says the Galileo mission to Jupiter could produce important new science about the small, primitive planets.

The unmanned Galileo probe, which will capitalize on the studies of the local scientist, will take a close look at the asteroid Gaspra during its October flight and the asteroid Ida in 1993 en route to a two-year encounter with Jupiter in 1995.

Gaspra, officially known as 951 Gaspra, is about 16 kilometers in diameter, and Ida, officially known as 243 Ida, is about 32 kilometers across. The largest asteroids — of the more than 2,200 recorded — are on the order of 1,000 kilometers across. Some, however, are only hundreds of meters wide.

Richard W. Shorthill, U. research associate professor of mechanical engineering, said the planned asteroid flybys, one of the least-publicized of Galileo's many experiments, may provide new information on the composition of asteroids — their sizes and shapes, masses and bulk densities, and what minerals are present on their surfaces.

He believes the study of asteroids is crucial to understanding the early history of the solar system.

"Comets and asteroids are important, unreached frontiers in planetary exploration. As a group, these primitive objects undoubtedly hold meaningful clues to the formation

GALILEO

Continued from A1

and evolution of our solar system," he said.

Long-term research conducted by the U. scientist provided valuable information for the Galileo mission.

Shorthill and Paul E. Johnson, professor of astronomy at the University of Wyoming, studied asteroids from 1980 to 1987, using a telescope near Laramie equipped for infrared studies. Their research was part of a program designed to improve the Air Force's ability to identify faint or indistinguishable objects in space with telescopes.

According to Shorthill, the co-researchers installed a highly sensitive solid-state infrared detector at the focal point of the University of Wyoming's 2.3-meter telescope to measure the heat radiated by planets, asteroids and selected gas clouds.

"Up until now, asteroid classification has been confined to the brighter ones, which may give a distorted view of the overall types and distribution of asteroids," Shorthill said. "Because additional space missions to the asteroids are planned, a better understanding of these small objects is crucial to making the best choices for target asteroids."

The U. scientist said Galileo will provide the United States with its only close-up study of the asteroids until the Comet Rendezvous Asteroid Flyby mission, which is scheduled for launch in August 1995.
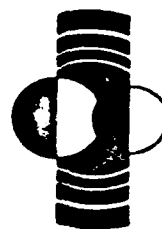
LUNAR AND PLANETARY INSTITUTE

3303 NASA ROAD 1   HOUSTON, TEXAS 77058   CABLE ADDRESS LUNSI

TEL: 713/486-2141

LPI SEMINAR SERIES

WEDNESDAY, JULY 27, 1988

" MEASURING AND MODELING THE NON-GREY BODY THERMAL EMISSION FROM SOLID SURFACED PLANETARY BODIES"

Karl Vogler
University of Wyoming and LPI

3:30 p.m.   **Berkner Room**

U. Study May Help Air Force Identify Objects in Space

A heat radiation study of space objects by a University of Utah scientist could improve the U.S. Air Force's ability to identify faint or indistinguishable objects in space with orbiting or ground-based telescopes.

Dr. Richard W. Shorthill, research associate professor of mechanical and industrial engineering, will begin a three-year study using the University of Wyoming's infrared telescope near Laramie. The study will measure heat radiated by space objects in a project funded by the Air Force Office of Scientific Research.

Dr. Shorthill, a planetologist, was an astrophysicist in the mid-1970s for the Boeing Co. and the principal investigator of the soil experiments conducted on the surface of Mars by the Viking landers. While at the Boeing Scientific Research Laboratories, he worked with a team that measured heat radiation from the moon during periods of total and partial lunar eclipses. That research provided information for the selection of landing sites for the Apollo moon landings.

Assisting Dr. Shorthill will be Dr. Thomas F. Greene, research engineer at Boeing Co., and Dr. Paul E. Johnson, professor of astronomy at the University of Wyoming.

"The focus of our research will be to calibrate infrared detectors in the 5-to-30-micron wavelength, a range beyond human visibility," Dr. Shorthill said. Calibrating involves comparing, checking or correcting the gradu-ations of scales of a measuring instrument — in this case a heat-radiation detector.

Dr. Shorthill said heat radiated by planets, asteroids and even by certain gas clouds can be measured by installing a highly sensitive solid-state infrared detector at the focal point of a telescope. The telescope in Wyoming is located on Jelm Mountain near Laramie at the 9,600-foot level and is one of the best of its kind in the world.

The study will explore the mysterious asteroids — small, irregularly shaped bodies orbiting the sun, most notably between the orbits of Mars and Jupiter — believed to be fragments of material that failed to condense into a single planet or matter from the nuclei of old comets.

"We have also chosen to look at the very faint asteroids, those of the 17th magnitude and fainter, that are invisible to the eye except when image intensifiers are attached to a telescope," Dr. Shorthill said. Because of their brightness, large asteroids are easy to measure, where small asteroids are faint and must be observed for long periods of time to add up the light signal to a readable level.

"The better our infrared calibration, the better our understanding and classification of asteroids will be because we will be able to make better measurements of the physical and chemical properties of asteroids," Dr. Shorthill said.

U. professor hopes study on mountaintop can help identify objects in space

Sometime in July, a University of Utah professor will be sitting on a mountaintop in Wyoming, using a gold-coated telescope to measure heat radiated by space objects.

What Dr. Richard W. Shorthill learns in his infrared studies of the moon, Mars and asteroids could help the Air Force identify faint or indistinguishable objects in space.

Shorthill says the Air Force, which tracks all kinds of objects in space, is eager to improve its capability of differentiating between man-made space objects and those of natural origin.

"If you're tracking a slow-moving satellite, for example, you must be able to tell it apart from an asteroid or from some other kind of natural object that is moving at the same angular speed. Infrared adds to our ability to make identifications that can't be made by any other means," he said.

The U. research associate professor of mechanical and industrial engineering will begin a three-year calibration project in July, using the University of Wyoming's infrared telescope, which sits at the 9,600-foot level of Jelm Mountain near Laramie. He will be assisted by Dr. Thomas F. Greene, research engineer at the Boeing Co., and Dr. Paul E. Johnson, professor of astronomy at the University of Wyoming. The project is funded by the Air Force Office of Scientific Resarch.

University of Wyoming astronomers plan to give the telescope's 90-inch mirror a gold coating to improve its infrared reflectivity and reduce the "thermal noise" — the heat radiated by the telescope. Because gold reflects more than 99 percent of the infrared light that strikes it, the coating should make the calibration experiments even more effective.

Shorthill, who has studied the solar system for more than two decades, said the focus of the research will be to calibrate infrared detectors in the 5-to-30-micron wavelength, a range beyond human visibility.

Calibrating involves comparing, checking or correcting the graduations or scales of a measuring instrument — in this case a heat-radiation detector.

The heat radiated by planets, asteroids and even by certain gas clouds can be measured by installing a highly sensitive solid-state infrared detector at the focal point of a telescope, Shorthill said.

The detector is placed in a container about the size of a large thermos bottle, then cooled with liquid nitrogen and liquid helium to increase the detector's sensitivity to heat radiation.

Shorthill also plans to study the very faint asteroids, those of 17th magnitude or fainter, that are invisible to the eye except when image intensifiers are attached to a telescope.

Asteroids, which are small, irregularly shaped bodies orbiting the sun, are believed to be fragments of material that failed to condense into a single planet or material from the nuclei of old comets.

Large asteroids are easy to measure because of their brightness, but the small ones must be observed for long periods to add up the light signal to a readable level.

Shorthill said that, up to now, asteroid classification has been confined to the brighter ones, which may give a distorted view of their overall types and distribution. "Because space missions to asteroids are planned for the future, a better understanding of them is important in making the best choices for target asteroids," he said.

In the mid-1970s, Shorthill, a former astrophysicist for the Boeing Co., was principal investigator for the soil experiments conducted on the surface of Mars by the Viking landers. He is also an internationally recognized authority on space gyroscopes.

U. scientist's infrared studies could sharpen A.F. space eyes

By George Ferguson
Associate business editor

A University of Utah scientist's up-coming infrared studies of the moon, Mars and asteroids could improve the Air Force's ability to identify faint or indistinguishable objects in space with orbiting or ground-based telescopes.

Dr. Richard W. Shorthill, research associate professor of mechanical and industrial engineering, will begin the three-year calibration project in July, using the University of Wyoming's infrared telescope near Laramie.

Shorthill, who has studied the solar system for more than two decades, will measure heat radiated by space objects in a project funded by the Air force Office of Scientific Research. He will be assisted by Dr. Thomas F. Greene, research engineer at the Boeing Co., and Dr. Paul E. Johnson, professor of astronomy at the University of Wyoming.

"The focus of our research will be to calibrate infrared detectors in the 5 to 30 micron wavelength, a range beyond human visibility," says Shorthill, a planetologist. Calibrating involves comparing, checking or correcting the graduations or scales of a measuring instrument — in this case a heat radiation detector.

The heat radiated by planets, asteroids, and even by certain gas clouds, says Shorthill, can be measured by installing a highly sensitive solid-state infrared detector at the focal point of a telescope.

The detector is placed in a container about the size of a large thermos bottle, then cooled with liquid nitrogen and liquid helium to increase its sensitivity to heat radiation.

University of Wyoming researchers plan to give the telescope's 90-inch mirror a gold coating to improve its reflectivity in the infrared and reduce the thermal noise — heat radiated by the telescope. Because gold reflects more than 99 percent of the infrared light that strikes it, the coating should make the calibration experiments even more effective.

The University of Wyoming infrared telescope, which sits at the 9,600-foot level of Jelm Mountain, is one of the best of its kind in the world.

Shorthill's research also could shed important scientific light on the mysterious asteroids — small, irregularly shaped bodies orbiting the sun, most notably between the orbits of Mars and Jupiter. Asteroids are believed to be fragments of material that failed to condense into a single planet or conssist of material from the nuclei of old comets..

"We also have chosen to look at the very faint asteroids, those of the 17th magnitude and fainter, that are invisible to the eye except when image intensifiers are attached to a telescope," says Shorthill.

"The better our infrared calibration, the better our understanding and classification of asteroids will be because we will be able to make better measurements of the physical and chemical properties of asteroids."

Because of their brightness, large asteroids are easy to measure. On the other hand, small asteroids are faint and must be observed for long periods of time so that the light signal adds up to a readable level.

"Up to now, asteroid classification has been confined to the brighter ones, which may give a distorted view of their overall types and distribution," says Shorthill. "Because space missions to asteroids are planned for the future, a better understanding of them is important in making the best choices for target asteroids."

Shorthill says the Air Force, which tracks all kinds of objects in space, is eager to improve its capability of differentiating between man-made objects and those of natural origin.

"If you're tracking a slow moving satellite, for example, you must be able to tell it from an asteroid or from some other kind of natural object that is moving at the same angular speed. Infrareds add to our ability to make identifications that can't be made by any other means," he says.

In the mid-1970s, Shorthill, a former astrophysicist for Boeing Co., was principal investigator for the soil experiments conducted on the surface of Mars by the Viking landers. He also is an internationally recognized authority on space gyroscopes.

While at the Boeing Scientific Research Laboratories, Shorthill and his collegues measured heat radiation from the moon, particularly during periods of a total or partial lunar eclipse.

Combined with radar reflections and orbital photographs, their research provided valuable information in the selection of landing sites for America's Apollo moon landers. Shorthill was active in briefing the Apollo astronauts and in intrerpreting the data.